Advanced systems for precision diagnosis and therapy of visual disorders

Original Citation:
Advanced systems for precision diagnosis and therapy of visual disorders / D'Alessandro, Vito Ivano. - ELETTRONICO. - (2025). [10.60576/poliba/iris/d-alessandro-vito-ivano_phd2025]

Published version
DOI:10.60576/poliba/iris/d-alessandro-vito-ivano_phd2025

Publisher: Politecnico di Bari

Politecnico
di Bari

LIBERATORIA PER L'ARCHIVIAZIONE DELLA TESI DI DOTTORATO

Al Magnifico Rettore
del Politecnico di Bari

Il sottoscritto Vito Ivano D'Alessandro nato a Grumo Appula il 02/04/1998

residente a Bitonto in via Tenente Francesco Lillo, 5 e-mail ivano_98@live.com

iscritto al 3° anno di Corso di Dottorato di Ricerca in Ingegneria Elettrica e dell'Informazione ciclo XXXVIII

ed essendo stato ammesso a sostenere l'esame finale con la prevista discussione della tesi dal titolo:

Advanced Systems for Precision Diagnosis and Therapy of Visual Disorders

DICHIARA

1) di essere consapevole che, ai sensi del D.P.R. n. 445 del 28.12.2000, le dichiarazioni mendaci, la falsità negli atti e l'uso di atti falsi sono puniti ai sensi del codice penale e delle Leggi speciali in materia, e che nel caso ricorressero dette ipotesi, decade fin dall'inizio e senza necessità di nessuna formalità dai benefici conseguenti al provvedimento emanato sulla base di tali dichiarazioni;
2) di essere iscritto al Corso di Dottorato di ricerca Ingegneria Elettrica e dell'Informazione ciclo XXXVIII, corso attivato ai sensi del "*Regolamento dei Corsi di Dottorato di ricerca del Politecnico di Bari*", emanato con D.R. n.286 del 01.07.2013;
3) di essere pienamente a conoscenza delle disposizioni contenute nel predetto Regolamento in merito alla procedura di deposito, pubblicazione e autoarchiviazione della tesi di dottorato nell'Archivio Istituzionale ad accesso aperto alla letteratura scientifica;
4) di essere consapevole che attraverso l'autoarchiviazione delle tesi nell'Archivio Istituzionale ad accesso aperto alla letteratura scientifica del Politecnico di Bari (IRIS-POLIBA), l'Ateneo archivierà e renderà consultabile in rete (nel rispetto della Policy di Ateneo di cui al D.R. 642 del 13.11.2015) il testo completo della tesi di dottorato, fatta salva la possibilità di sottoscrizione di apposite licenze per le relative condizioni di utilizzo (di cui al sito http://www.creativecommons.it/Licenze), e fatte salve, altresì, le eventuali esigenze di "embargo", legate a strette considerazioni sulla tutelabilità e sfruttamento industriale/commerciale dei contenuti della tesi, da rappresentarsi mediante compilazione e sottoscrizione del modulo in calce (Richiesta di embargo);
5) che la tesi da depositare in IRIS-POLIBA, in formato digitale (PDF/A) sarà del tutto identica a quelle **consegnate**/inviate/da inviarsi ai componenti della commissione per l'esame finale e a qualsiasi altra copia depositata presso gli Uffici del Politecnico di Bari in forma cartacea o digitale, ovvero a quella da discutere in sede di esame finale, a quella da depositare, a cura dell'Ateneo, presso le Biblioteche Nazionali Centrali di Roma e Firenze e presso tutti gli Uffici competenti per legge al momento del deposito stesso, e che di conseguenza va esclusa qualsiasi responsabilità del Politecnico di Bari per quanto riguarda eventuali errori, imprecisioni o omissioni nei contenuti della tesi;
6) che il contenuto e l'organizzazione della tesi è opera originale realizzata dal sottoscritto e non compromette in alcun modo i diritti di terzi, ivi compresi quelli relativi alla sicurezza dei dati personali; che pertanto il Politecnico di Bari ed i suoi funzionari sono in ogni caso esenti da responsabilità di qualsivoglia natura: civile, amministrativa e penale e saranno dal sottoscritto tenuti indenni da qualsiasi richiesta o rivendicazione da parte di terzi;
7) che il contenuto della tesi non infrange in alcun modo il diritto d'Autore né gli obblighi connessi alla salvaguardia di diritti morali od economici di altri autori o di altri aventi diritto, sia per testi, immagini, foto, tabelle, o altre parti di cui la tesi è composta.

Bari, 09/01/2026 Firma Vito Ivano D'Alessandro

Il sottoscritto, con l'autoarchiviazione della propria tesi di dottorato nell'Archivio Istituzionale ad accesso aperto del Politecnico di Bari (POLIBA-IRIS), pur mantenendo su di essa tutti i diritti d'autore, morali ed economici, ai sensi della normativa vigente (Legge 633/1941 e ss.mm.ii.),

CONCEDE

- al Politecnico di Bari il permesso di trasferire l'opera su qualsiasi supporto e di convertirla in qualsiasi formato al fine di una corretta conservazione nel tempo. Il Politecnico di Bari garantisce che non verrà effettuata alcuna modifica al contenuto e alla struttura dell'opera.
- al Politecnico di Bari la possibilità di riprodurre l'opera in più di una copia per fini di sicurezza, back-up e conservazione.

Bari, 09/01/2026 Firma Vito Ivano D'Alessandro

Finanziato dall'Unione europea
NextGenerationEU

Ministero dell'Università e della Ricerca

Italiadomani
Piano Nazionale di Ripresa e Resilienza

Politecnico di Bari

The doctoral scholarship was funded by
the European Union - Next Generation EU, Mission 4 Component 4 CUP D93C22000720005

POLITECNICO DI BARI

DEPARTMENT OF ELECTRICAL AND INFORMATION ENGINEERING

ELECTRICAL AND INFORMATION PH.D. PROGRAM

SSD: ING-INF/07–ELECTRICAL AND ELECTRONIC MEASUREMENTS

FINAL DISSERTATION

Advanced Systems for Precision Diagnosis and Therapy of Visual Disorders

---

by

VITO IVANO D'ALESSANDRO
Vito Ivano D'Alessandro

Referees:
PROF. GIULIANO SCARCELLI
PROF. SABRINA GRASSINI

Supervisors:
PROF. FILIPPO ATTIVISSIMO
PROF. ATTILIO DI NISIO
Attilio Di Nisio

Coordinator of Ph.D. Program:
Prof. Mario Carpentieri
Mario Carpentieri

Course n°38, 01/11/2022-31/10/2025

CONTENTS

CONTENTS

ABSTRACT

The objective of this thesis was to design, develop, and validate a novel non-contact method for measuring intraocular pressure (IOP) through the analysis of corneal dynamics induced by natural blinking. The proposed method leverages high-speed ocular imaging and image processing techniques to quantify corneal rebound, associated with IOP, following eyelid-induced deformation, thus eliminating the need for contact-based tonometry.

An acquisition system was developed, consisting of a modified ophthalmic chin rest and a high–frame rate camera, to capture the lateral corneal profile during blinking. From the acquired images, ocular masks were generated by applying a deep learning–based segmentation model. Subsequently, a geometry-based approach was applied to extract the corneal profile from these masks. The longitudinal displacement of this profile was analyzed during the eye-opening phase of the blink. The temporal behavior of the displacement followed an exponential curve, from which two biomechanical metrics describing corneal dynamics were derived: the time constant (τ), representing the speed of corneal rebound, and the displacement amplitude (A), quantifying the extent of corneal profile movement. These metrics were first evaluated in terms of intra-subject repeatability on healthy participants, providing reference variability ranges for future clinical studies.

The method was then applied to assess corneal dynamics under baseline and elevated IOP conditions, the latter induced through the Valsalva maneuver and confirmed with a portable tonometer. Results obtained from healthy volunteers showed a statistically significant reduction in τ under elevated IOP, indicating a faster corneal rebound, while A remained unchanged. This suggests that τ is a promising parameter for detecting relative IOP variations, whereas A is less sensitive to pressure changes.

By enabling continuous, non-invasive, and home-based IOP monitoring, this approach has the potential to complement or partially replace traditional tonometry, thereby improving early glaucoma detection and follow-up. In addition, the thesis explores complementary developments, including noise-robust blink detection algorithms and complete ECG waveform segmentation, broadening the scope of non-contact biomedical measurement systems.

LIST OF PUBLICATIONS

A total of **four** papers has been published in international journals during the Ph.D. program, and **one** has been submitted and is under review. Paper **[P6]** has been authored before the beginning of the Ph.D. program. Both papers **[P8]** and **[P9]** have received the **IEEE MeMeA 2023 Certificates of Appreciation**.

International Journal Papers Indexed by Scopus:

[P1] F. Attivissimo, **V. I. D'Alessandro**, A. Di Nisio, G. Scarcelli, J. Schumacher, and A. M. L. Lanzolla, "Performance evaluation of image processing algorithms for eye blinking detection," Measurement, vol. 223, p. 113767, Dec. 2023, doi: `10.1016/j.measurement.2023.113767`.

[P2] F. Attivissimo, **V.I. D'Alessandro**, L. De Palma, A. M. L. Lanzolla, and A. Di Nisio, "Non-Invasive Blood Pressure Sensing via Machine Learning," Sensors, vol. 23, no. 19, p. 8342, Oct. 2023, doi: `10.3390/s23198342`.

[P3] M. Scarpetta, M. Spadavecchia, P. Affuso, **V. I. D'Alessandro**, and N. Giaquinto, "Use of the SNOWED Dataset for Sentinel-2 Remote Sensing of Water Bodies: The Case of the Po River," Sensors, vol. 24, no. 17, p. 5827, Sep. 2024, doi: `10.3390/s24175827`.

[P4] A. Di Nisio, **V. I. D'Alessandro**, G. Scarcelli, A. M. L. Lanzolla, and F. Attivissimo, "Noise robustness evaluation of image processing algorithms for eye blinking detection," Measurement, vol. 239, p. 115508, Jan. 2025, doi: `10.1016/j.measurement.2024.115508`.

[P5] **V. I. D'Alessandro**, F. Attivissimo, A. Di Nisio, A.M.L. Lanzolla, A. Isaiah, and G. Scarcelli, "Association between Blink-related Corneal Dynamics During Blinking and IOP", Scientific Reports (Submitted, Under Review).

International Conference Proceedings Indexed by Scopus:

[P6] **V. I. D'Alessandro**, F. Paciolla, L. De Palma, F. Adamo, A. Di Nisio, and N. Giaquinto, "Robotized sorter for blood classification using RFID tags," in 2022 IEEE International Symposium on Medical Measurements and Applications (MeMeA), Messina, Italy: IEEE, Jun. 2022, pp. 1–6. doi: `10.1109/memea54994.2022.9856477`.

[P7] M. Scarpetta, M. Spadavecchia, **V. I. D'Alessandro**, L. D. Palma, and N. Giaquinto, "A new dataset of satellite images for deep learning-based coastline measurement," in 2022 IEEE International Conference on Metrology for Extended Reality, Artificial Intelligence and Neural Engineering (MetroXRAINE), Rome, Italy: IEEE, Oct. 2022, pp. 635–640. doi: `10.1109/metroxraine54828.2022.9967574`.

[P8] **V. I. D'Alessandro**, L. D. Palma, F. Attivissimo, A. D. Nisio, and A. M. L. Lanzolla, "U-Net convolutional neural network for multisource heterogeneous iris segmentation," in 2023 IEEE International Symposium on Medical Measurements and Applications (MeMeA), Jeju, Korea, Republic of: IEEE, Jun. 2023, pp. 1–5. doi: `10.1109/MeMeA57477.2023.10171896`.

[P9] L. D. Palma, **V. I. D'Alessandro**, F. Attivissimo, A. D. Nisio, and A. M. L. Lanzolla, "ECG wave segmentation algorithm for complete P-QRS-T detection," in 2023 IEEE International Symposium on Medical

Measurements and Applications (MeMeA), Jeju, Korea, Republic of: IEEE, Jun. 2023, pp. 1–6. doi: `10.1109/memea57477.2023.10171894`.

[P10] **V. I. D'Alessandro**, F. Adamo, L. De Palma, D. Lotano, and M. Scarpetta, "U-Net Convolutional Neural Network for Optic Disc Segmentation," in 2023 IEEE International Conference on Metrology for eXtended Reality, Artificial Intelligence and Neural Engineering (MetroXRAINE), Milano, Italy: IEEE, Oct. 2023, pp. 1087–1091. doi: `10.1109/metroxraine58569.2023.10405762`.

[P11] **V. I. D'Alessandro**, J. Schumacher, F. Attivissimo, A. Isaiah, and G. Scarcelli, "Non-contact Measurement of Intraocular Pressure (IOP) Via Corneal Deformation Induced by Natural Blinking," in Optica Imaging Congress 2024 (3D, AOMS, COSI, ISA, pcAOP), Toulouse: Optica Publishing Group, 2024, p. CTh5A.3. doi: `10.1364/cosi.2024.cth5a.3`.

National Conference Proceedings:

[P12] **V. I. D'Alessandro**, L. De Palma, A. Di Nisio, A.M.L. Lanzolla, M.A. Ragolia, M. Scarpetta, "Enfatizzazione del segnale fotopletismografico e selezione di nuove feature per il monitoraggio non invasivo della pressione sanguigna", Atti del VII Forum Nazionale delle Misure, Bologna, pp. 197-198, ISBN: 978-88-942753-2-2, 13-15 settembre 2023.

[P13] F. Attivissimo, A. Di Nisio, N. Giaquinto, A.M.L. Lanzolla, **V. I. D'Alessandro**, D. Lotano, "Sistema di rilevamento dell'ammiccamento mediante acquisizione con smartphone", Atti del VII Forum Nazionale delle Misure, Bologna, pp. 201-202, ISBN: 978-88-942753-2-2, 13-15 settembre 2023.

[P14] L. De Palma, F. Attivissimo, A. Di Nisio, **V.I. D'Alessandro**, "Stima non invasiva della pressione sanguigna dal segnale fotopletismografico utilizzando modelli di machine learning", Atti del VIII Forum Nazionale delle Misure, S. Vincenzo (LI), pp. 225-226, ISBN: 978-88-942753-3-9, 12-14 settembre 2024.

[P15] L. De Palma, F. Attivissimo, V. I. D'Alessandro, A. Di Nisio, A. M. L. Lanzolla, "Confronto delle performance di vcari modelli di machine learning per la stima non invasiva della pressione sanguigna utilizzando il segnale fotopletismografico", Atti del IX Forum Naazionale delle Misure, Napoli, 10-12 settembre 2025.

[P16] M. A. Ragolia, F. Adamo, G. Andria, V. I. D'Alessandro, N. Giaquinto, "Analisi dei parametri di modello e del setup sperimentale per la caratterizzazione di sistemi ultrasonici a matrice di fase", Atti del IX Forum Nazionale delle Misure, Napoli, 10-12 settembre 2025.

LIST OF FIGURES

LIST OF FIGURES

LIST OF TABLES

LIST OF ABBREVIATIONS

IOP Intraocular Pressure
POAG Primary Open-Angle Glaucoma
NTG Normal-Tension Glaucoma
HTG High-Tension Glaucoma
OHT Ocular Hypertension
GAT Goldmann Applanation Tonometer
NCT Non-Contact Tonometry
MEMS Micro-Electro-Mechanical Systems
RGB Red/Green/Blue
FPS Frames per Second
HCI Human Computer Interaction
EOG Electrooculography
EMG Electromyography
EEG Electroencephalography
LBP Local Binary Pattern
HOG Histogram of Oriented Gradients
SVM Support Vector Machine
EAR Eye Aspect Ratio
HSV Hue Saturation Value
ROI Region of Interest
FIR Finite Impulse Response
KL Kullback-Liebler
SSA Singular Spectrum Analysis
IAD Iris Area Detection
OF Optical Flow
GD Gabor Decomposition
GT Ground Truth
FDR False Discovery Rate

LIST OF ABBREVIATIONS

TPR True Positive Rate
LSB Least Significant Bit
DA Deformation Amplitude
PD Peak Distance
HCR Radius at Highest Concavity
HCT Highest Concavity Time
A1T Time at First Applanation
A2T Time of Second Applanation
A1V Velocity at First Applanation
A2V Velocity at Second Applanation
CL Combo Loss
BCE Binary CrossEntropy
IoU Intersection Over Union
GAT Goldmann Applanation Tonometer
ELP Eyelid Pressure
CVD Cardiovascular Disease
ECG Electrocardiogram
HRV Heart Rate Variability
HR Heart Rate
RR Respiratory Rate
WT Wavelet Transform
STFT Short-Time Fourier Transform
EMD Empirical Mode Decomposition
CNN Convolutional Neural Network
DAQ Data Acquisition
STD Standard Deviation
WDT Water Drinking Test

INTRODUCTION[1]

1.1 OVERVIEW AND THESIS OBJECTIVE

Glaucoma is a chronic, progressive optic neuropathy characterized by the degeneration of retinal ganglion cells and the corresponding axons in the optic nerve, ultimately leading to irreversible visual field loss [3], [4]. It represents the second leading cause of blindness globally and the first cause of irreversible blindness [5], with a prevalence that increases significantly with age. Recent epidemiological studies estimate that glaucoma affects over 76 million people worldwide, with projections suggesting this number may exceed 110 million by 2040 [6].

Among the various forms of glaucoma, POAG is the most common. It is typically associated with elevated IOP, which remains the only modifiable risk factor for the development and progression of the disease [7], [8]. However, other clinical conditions complicate this association. In NTG, optic nerve damage occurs even when IOP values remain within the statistical norm [9], whereas OHT describes elevated IOP in the absence of detectable optic nerve damage or visual field defects [10]. These forms underscore the multifactorial nature of the disease and the importance of frequent IOP monitoring to assess risk and progression over time.

Traditionally, IOP is measured using GAT, which estimates the pressure

---

[1] This introduction is based on the papers [1], [2].

required to flatten a known area of the cornea [11]. Although GAT is widely regarded as the gold standard, its limitations are well-documented: it requires corneal contact and topical anesthetic, is operator-dependent, and must be performed in a clinical setting [12], [13]. These limitations restrict the frequency and continuity of measurements, rendering it unsuitable for long-term, real-time monitoring. Yet, IOP is known to fluctuate diurnally and in response to systemic or physiological stimuli, such as posture, hydration, or physical exertion [14], [15], which may not be captured during single-time clinical assessments.

In response to these limitations, alternative IOP monitoring technologies have emerged in recent years. Rebound tonometry, such as the iCare series, allows for user-friendly, anesthesia-free contact measurements and is now FDA-approved for home use [16]. NCT, which uses an air puff to measure corneal deformation, eliminates the need for contact but suffers from reduced accuracy and sensitivity to corneal biomechanics [17], [18].

More recently, implantable pressure sensors and smart contact lenses have been developed to enable long-term and even continuous IOP monitoring. These include MEMS-based sensors surgically implanted within the eye [19], [20], [21], [22] or systems embedded in soft contact lenses capable of streaming IOP data in real time [23], [24], [25], [26], [27]. While promising, these technologies still present several limitations. Smart contact lenses embedded with sensors offer continuous IOP monitoring, but may be affected by blinking and posture changes [28], [29]. Implantable sensors provide direct measurements of IOP but require surgical implantation and are associated with potential ocular damage [30], [31], [32]. Therefore, despite addressing some of the challenges of traditional approaches, these innovative methods still involve direct contact with the eye and present safety and usability concerns that currently hinder widespread clinical adoption.

The goal of this research is to explore a completely non-contact and camera-based alternative to IOP monitoring, based on the hypothesis that spontaneous blinking can serve as a natural actuation mechanism for characterizing corneal biomechanics, which are themselves influenced by internal ocular pressure.

During a blink, the upper eyelid applies a mechanical force onto the corneal surface, inducing a temporary deformation [33], [34], [35]. Once the lid reopens, the cornea returns to its original shape, with a recovery process governed by its intrinsic elastic properties and the opposing pressure exerted by the internal fluid compartments of the eye. By capturing the blink-induced corneal motion using a high-speed camera and tracking the corneal profile throughout the blink cycle, it becomes possible to extract meaningful dynamic parameters such as deformation amplitude, rebound time constant, and displacement trajectory.

These parameters, if consistently correlated with IOP, could form the basis for a low-cost, non-invasive, and home-deployable IOP screening method. The use of an RGB camera, similar to those available in smartphones or embedded in wearable devices, further increases the accessibility of the method and opens new perspectives in remote glaucoma monitoring and telemedicine.

The development of such a system involves several technical challenges, including the accurate detection of blinks, robust segmentation of the ocular region across varying eye states (closed, semi-closed, open), and the modeling of corneal dynamics from noisy or partially occluded visual data. To address these challenges, a full processing pipeline has been developed, which includes image correlation for blink detection, deep learning–based segmentation using U-Net architectures, and geodesic path extraction to isolate the corneal contour. The temporal evolution of the corneal centroid is then modeled using exponential fitting to derive the desired biomechanical features.

To validate the proposed method, a dataset of lateral eye blink videos was acquired from human participants using a custom-built imaging system operating at 510 FPS. A case-control experimental setup was used to compare baseline and elevated IOP conditions, the latter induced using the Valsalva maneuver, a natural and non-invasive technique that causes a temporary IOP increase [36], [37], [38], [39].

This project was developed within an international collaboration involving the Department of Electrical and Information Engineering at Politecnico di Bari, the Fischell Department of Bioengineering at the University of Maryland, College Park, and the University of Maryland School of Medicine, Baltimore. The interdisciplinary contributions from biomedical engineers, computer scientists, and ophthalmologists allowed for the design, implementation, and preliminary clinical validation of the proposed IOP estimation system.

1.2 THESIS STRUCTURE

The thesis is structured as follows: in **By** integrating ECG analysis with the ocular-based metrics developed in previous chapters, this final part of the thesis expands the proposed framework toward multi-parametric health monitoring, where cardiovascular and ocular signals can be jointly interpreted to provide a more comprehensive understanding of IOP dynamics and ocular biomechanics in relation to systemic physiological states.

Chapter 1, the performance of five image processing algorithms for eye blink detection is evaluated. The chapter presents the experimental framework, including the acquisition protocol and the metrics adopted to assess accuracy and repeatability in detecting blinking frames. The goal is to identify the most reliable algorithm for subsequent processing steps.

In

Chapter 2, the robustness of the same set of algorithms is investigated under various noise conditions. Additive Gaussian noise is introduced at increasing intensities, and a Monte Carlo simulation is used to assess how each method's performance degrades. The chapter identifies the most resilient algorithm under noisy and suboptimal acquisition conditions, which are often encountered in real-world scenarios.

Chapter 3 introduces a novel non-invasive method for analyzing blink-induced corneal deformation using a lateral high-speed imaging acquisition system. After segmenting the ocular region and extracting the corneal contour, the temporal evolution of the corneal centroid is modeled using a first-order exponential function. This enables the extraction of biomechanical parameters such as deformation amplitude and recovery time constant, which are hypothesized to be influenced by intraocular pressure.

In

Chapter 4, an experimental validation is carried out to investigate the relationship between blink-related corneal dynamics and intraocular pressure. Measurements are performed under baseline and elevated IOP conditions, the latter obtained through the Valsalva maneuver. A portable tonometer is used to obtain reference IOP values, and statistical analyses are conducted to evaluate whether the proposed features can effectively discriminate between the two pressure states.

Finally,

Chapter 5, focuses on ECG signal segmentation for telemedicine applications. While the previous chapters of the thesis investigate ocular dynamics and IOP variations induced by blinking and the Valsalva maneuver, cardiovascular activity, captured by the ECG, is known to modulate both ocular perfusion and IOP through systemic blood pressure oscillations and autonomic regulation. Thus, this chapter presents a pipeline to detect the complete P–QRS–T complex in single-lead ECG recordings using wavelet decomposition and Otsu's thresholding. The algorithm's performance is validated in terms of temporal accuracy and intersection-over-union with annotated ECG events. By integrating ECG analysis with the ocular-based metrics developed in previous chapters, this final part of the thesis expands the proposed framework toward multi-parametric health monitoring, where cardiovascular and ocular signals can be jointly interpreted to provide a more comprehensive understanding of IOP dynamics and ocular biomechanics in relation to systemic physiological states.

CHAPTER 1

EYE BLINK DETECTION: ALGORITHMS PERFORMANCE EVALUATION[2]

INTRODUCTION

An eye blink is formally defined as a temporary closure of the eyes, involving the coordinated movement of the upper and lower eyelids [41]. In adults, the average blinking rate is approximately 12 times per minute, with a typical blink duration ranging between 100 and 400 milliseconds [42].

Eye blink dynamics are relevant in numerous domains, including HCI, gaze

---

[2] This Chapter is based on [40].

tracking systems, and various medical contexts [43], [44], [45]. For example, studies have shown that patients with Parkinson's disease tend to blink more slowly than healthy individuals, whereas those with Tourette syndrome exhibit more rapid blinking patterns [46]. Such findings have led to the use of blink rate as a biomarker for certain neurological disorders, potentially offering a non-invasive alternative to traditional diagnostic tools based on muscle activity, such as hand grip strength [10]. Moreover, blink characteristics have been linked to IOP and are of growing interest in glaucoma management, particularly in relation to vascular components implicated in NTG [47], [48].

Other notable applications of blink detection include eye fatigue analysis for 3D display viewing, psychological state assessment [49], and driver drowsiness monitoring [50].

Blink detection techniques can be broadly classified into non-image-based and image-based methods. Non-image-based approaches include EOG [51], EMG [52], and EEG. These methods offer rapid signal acquisition but are inherently invasive, requiring physical contact with the subject, which can lead to discomfort and introduce signal artifacts due to muscle activity.

In contrast, image-based methods are entirely non-invasive, requiring no physical contact with the eye. Their performance largely depends on image acquisition conditions, such as lighting and shutter speed. Although generally more computationally demanding, they can deliver high accuracy. Depending on the data source, these methods may rely on video sequences, single-image analysis with or without prior training, and a variety of machine learning or handcrafted feature extraction techniques.

Several algorithms for image-based blink detection have been proposed in the literature. Some use spatiotemporal filters and variance maps to locate the eyes. Mobile-based approaches, such as drowsiness detection systems using the OpenCV library on Android platforms, rely on Haar classifiers and template matching [53].

Other methods leverage LBP, achieving detection rates up to 99.2% by comparing the histogram of LBP descriptors of open eyes against those in subsequent frames [54]. Alternative strategies tracking the EAR over time [55], and following eyelid motion through landmark detection and filtering [56]. Techniques using light reflection [57], color-space analysis (e.g., HSV space) [58], and robust finite state machines [59] have also demonstrated promising accuracy in detecting eye states.

The primary aim of this chapter is to evaluate and compare the performance of five non-supervised image processing algorithms for eye blink detection using a low-cost image acquisition system. Among them, a novel method based on iris area variation across video frames is introduced, while the remaining four algorithms are adapted from existing approaches in the literature. Each method operates on RGB video frames, and an additional analysis investigates whether the use of individual RGB channels improves performance compared to grayscale processing.

1.1 IMAGE ACQUISITION SYSTEM

The acquisition system designed for this study was developed to capture videos of the eye during natural, spontaneous blinking in a controlled and repeatable manner. The setup includes an ophthalmic chin rest to stabilize the participant's head and minimize involuntary movements throughout the recording process. A smartphone running iOS is used as the imaging device, positioned in front of the subject using a custom-built cartesian support structure.

This structure was assembled using Bosch Rexroth 20x20 mm aluminum profiles, offering mechanical flexibility and precision in camera positioning. The smartphone holder, affixed to the main frame, was manufactured using additive manufacturing techniques to ensure mechanical compatibility and ergonomic alignment. The modular design of the setup allows for fine manual adjustment along three axes, enabling accurate alignment between the smartphone camera and the participant's eye.

The smartphone's camera settings were configured to capture video at a frame rate of 30 FPS, with a resolution of 848 × 464 pixels and a standard 24-bit RGB color depth (8 bits per channel). While this frame rate is not high enough to analyze the entire blink dynamics in detail, it is sufficient to identify the presence and timing of blink events.

To ensure consistent lighting conditions, the experiments were conducted indoors. A circular ring light was mounted around the smartphone lens to provide homogeneous illumination of the participant's face. The distance between the camera and the chin rest was fixed at 100 mm. The position of the camera was adjusted so that approximately half of the subject's face was included in the video frame, with particular attention to the eye region. This configuration is shown in **Fig. 1**, which includes both frontal and lateral views of the experimental setup.

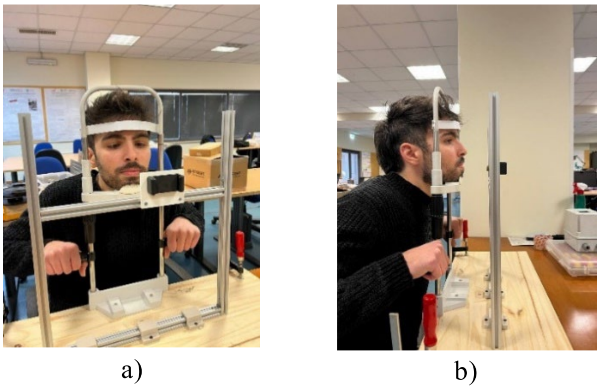

a) b)

Fig. 1. Image Acquisition System. a) frontal and b) lateral view.

The videos were recorded in RGB format and later converted to grayscale for further analysis, allowing for a comparative evaluation of the image processing algorithms on both color and monochrome images. An example frame acquired during the experiment is presented in **Fig. 2**, showing the original RGB image and its grayscale converted version.

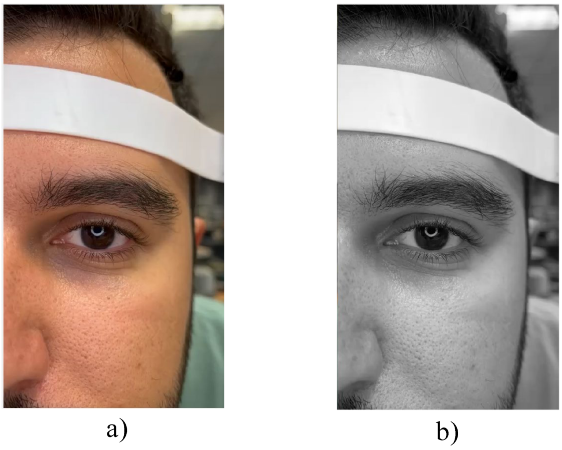
a) b)

Fig. 2. a) RGB frame captured during acquisition. b) Conversed grayscale image.

The dataset acquired with this system consists of video recordings from multiple participants varying in age, skin tone, and eye color. Each participant was asked to look directly at the camera lens during the acquisition, minimizing any shifts in gaze direction. The duration of each video varied, as did the number of blink events, all of which were spontaneous.

Characteristics of each participant are reported in **Table 1**.

Participant	Age	Gender	Eye color	Skin tone
1	28	Male	Brown	Olive
2	20	Female	Hazel	Fair
3	24	Female	Dark Brown	Medium
4	26	Male	Dark Brown	Medium

Table 1. Participants' characteristics.

The data collection was performed under naturalistic conditions to reflect real-world scenarios. Participants were recorded during routine daily activities, which helped preserve the natural variability of blink patterns. This is relevant since previous studies have shown that blink dynamics are influenced by fatigue and cognitive state [60].

1.2 DETECTION OF REGION OF INTEREST

To enhance computational efficiency and reduce unnecessary processing, a ROI is automatically extracted from the eye images prior to the application of the blinking detection algorithms. This strategy significantly decreases computational time and avoids the inclusion of irrelevant visual information, as demonstrated in previous studies [61], [62].

The proposed ROI detection approach is fully automatic and relies on color information to differentiate the eye region from the surrounding skin. The methodology is structured as outlined in the flowchart in **Fig. 3**.

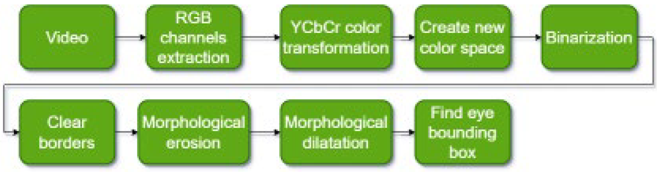

Fig. 3. Automatic Crop Algorithm Flowchart.

To accurately identify the eye area, the RGB image is transformed into the YCbCr color space, which is particularly effective at separating luminance and chrominance components. This transformation facilitates more robust identification of skin regions and improves contrast between eye and non-eye areas, even under non-uniform lighting conditions [63].

In the YCbCr space, the eye region typically exhibits high values of the blue-difference chroma component (Cb) and low values of the red-difference chroma component (Cr). Based on these observations, a custom-defined eye map is created using the following expression:

$$EyeMapC = \frac{1}{3}\left[(C_b^2) + (1 - C_r)^2 + \frac{C_b}{C_r}\right]$$

In the given formula, C_r is defined as the difference between the red channel R and the luminance component Y: $C_r = R - Y$; C_b is defined as the difference between the blue channel and Y: $C_b = B - Y$. Additionally, the luminance component is calculated using the formula $Y = 0.299R + 0.587G + 0.114B$, where R, G, and B represent the red, green, and blue channel values, respectively. This formulation emphasizes the eye region by assigning higher values where C_b is large and C_r is small, typically corresponding to the iris. In cases where the RGB components are equal (e.g., in grayscale regions), C_r becomes zero, causing the division to diverge. These pixels are thus excluded from the skin region.

Following the creation of the eye map, Otsu's thresholding is applied to binarize the image. This method selects an optimal threshold that minimizes the intra-class variance between foreground (eye) and background (skin) pixels [64]. However, the initial binary mask may include edge-connected artifacts. To mitigate this, a clear border operation is applied to remove objects touching the image edges. Next, the binary mask undergoes morphological filtering: erosion using a disk structuring element with a radius of 10 pixels, followed by dilation with a radius of 20 pixels. This sequence helps eliminate small, unwanted regions—such as those caused by skin texture—while preserving the main structures associated with the eyes and eyebrows. The resulting binary mask is illustrated in **Fig. 4a**.

To isolate the ROI corresponding specifically to the eye region, the bounding boxes of each connected component in the binary mask are computed. The lowest bounding box in the vertical direction is selected automatically, assuming that the eyes are positioned below the eyebrows. This approach ensures a consistent and accurate crop around the eye. An example of this selection is shown in **Fig. 4b**.

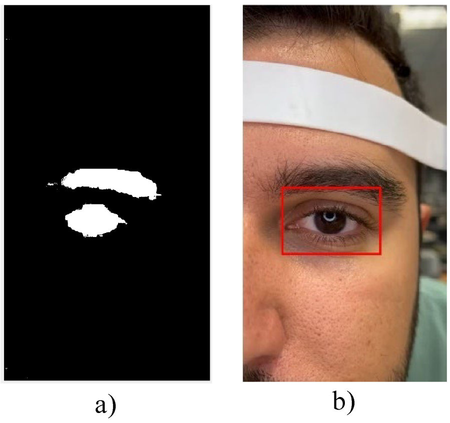
a) b)

Fig. 4. a) Eye and eyebrow mask and b) bounding box covering only the eye.

Once identified, the ROI is applied both to the original RGB image and to the grayscale-converted image. Importantly, the ROI is computed only on the first frame of each video sequence and then held constant throughout the analysis of all remaining frames. This approach ensures consistent spatial alignment across the entire video sequence and reduces the computational load by avoiding repeated ROI extraction.

1.3 METHODS

This section presents and describes the five unsupervised image processing algorithms evaluated in this study for eye-blink detection. Each algorithm processes a sequence of video frames and generates a signal that distinguishes between open and closed-eye states. The final output is a binary logic signal used to assess the algorithm's performance both in terms of frame-wise classification and blink event detection. The algorithms, selected based on literature relevance, are described in detail in the following subsections.

1.3.1 IRIS AREA DETECTION

This method identifies and tracks the area of the iris throughout the video frames. A flowchart summarizing the steps of the algorithm is shown in **Fig. 5**.

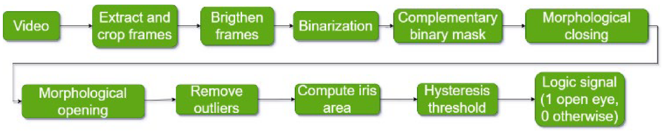

Fig. 5. Iris Area Detection Algorithm.

The process begins with a contrast enhancement step based on a low-light enhancement technique [65], which improves visibility and reduces haze. The enhanced image is then binarized using global Otsu's thresholding, and morphological operations are applied—specifically, a closing followed by an opening—to remove noise and small objects. Only the largest binary region, assumed to correspond to the iris, is retained.

The area of this binary region is then computed for each frame, resulting in a raw signal representing the iris area across time, as can be seen in **Fig. 6**. This signal decreases during blinking due to partial or full occlusion of the iris and increases when the eye is fully open. The raw signal is normalized to the [0,1] range and processed through hysteresis thresholding to obtain a clean binary signal identifying blink intervals.

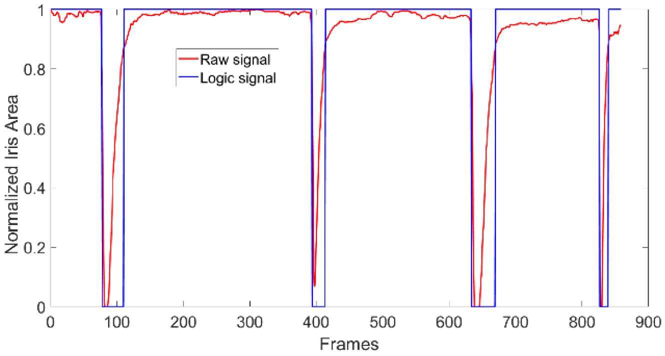

Fig. 6. Raw (red) and logic signal (blue) for iris area detection.

1.3.2 OPTICAL FLOW

The second algorithm is based on the analysis of motion between consecutive frames using the Gunnar–Farneback optical flow method [66] and is structured as shown in **Fig. 7**.

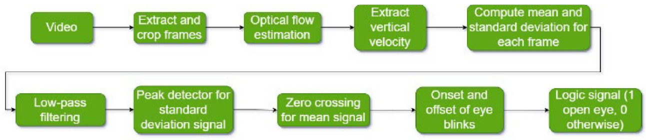

Fig. 7. Optical Flow Estimation Algorithm.

Unlike the Lucas–Kanade method, Gunnar–Farneback provides denser and more accurate motion vectors for dynamic regions such as eyelids, particularly when large displacements occur [67], [68]. As can be seen in **Fig. 8**, the estimated velocity vectors when an eye blink doesn't occur have a lower magnitude (measured in pixels per frame) compared to the case when the blink starts and during its occurrence.

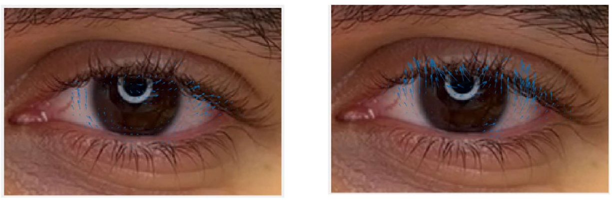

a) b)

Fig. 8. Velocity vectors estimation when a) no blink occurs and b) a blink occurs.

In this method, the vertical component of the average motion vector (μ) is extracted since eyelid motion occurs primarily along the vertical axis. Additionally, the standard deviation (σ) of vertical motion vectors is computed. Peaks in σ indicate motion related to blinking, while zero-crossings in μ are used to identify onset and offset points of each blink.

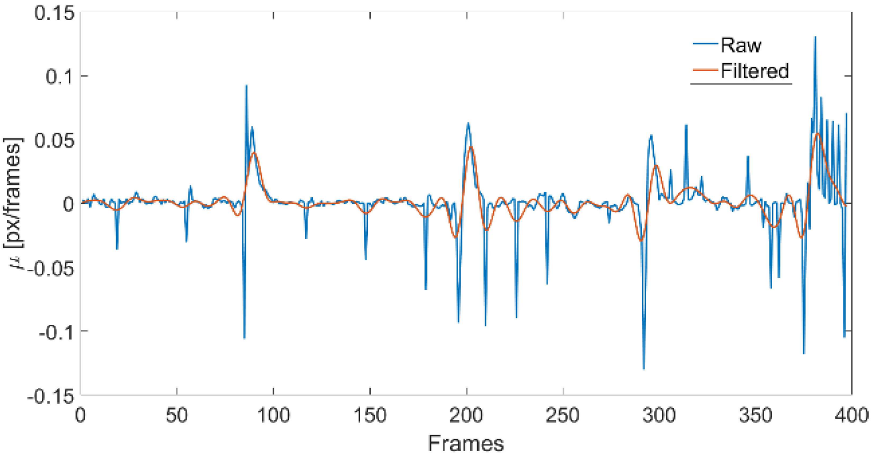

Fig. 9. Mean y-component of velocity.

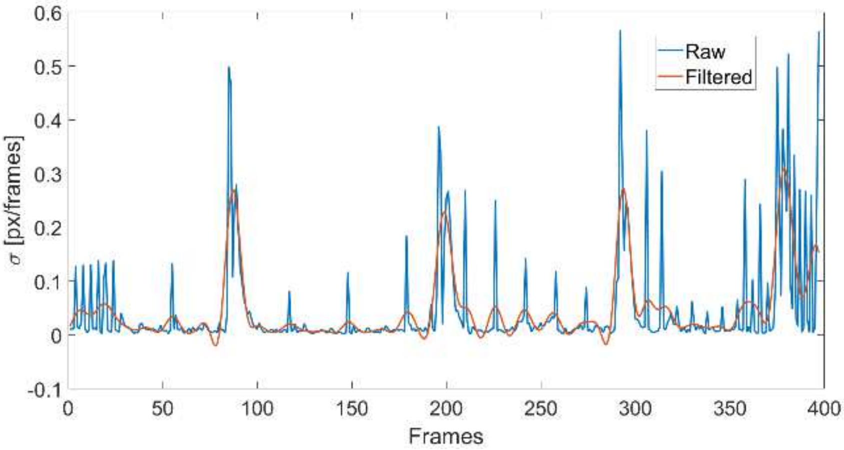

Fig. 10. Standard deviation of y-component of velocity.

To remove outlier peaks in the μ and σ waveforms, a Kaiser FIR low-pass filter with a normalized cut-off frequency of 0.1 is applied and the results are shown in **Fig. 9** and **Fig. 10** (red line), respectively.

The zero-crossing algorithm proposed in this study is based on the detection of zero-crossing points in the μ waveform. After that, to determine which of these points is an onset or offset of eye blinking, a peak detector is applied to the σ waveform because each peak is related to an eye blink. Indeed, the onset of the eye blink is defined as the first zero of μ waveform before i-th peak whereas the offset as the first zero in the μ waveform after the i-th peak. The resulting logical signal, representing blink detection, is shown in **Fig. 11** (red line).

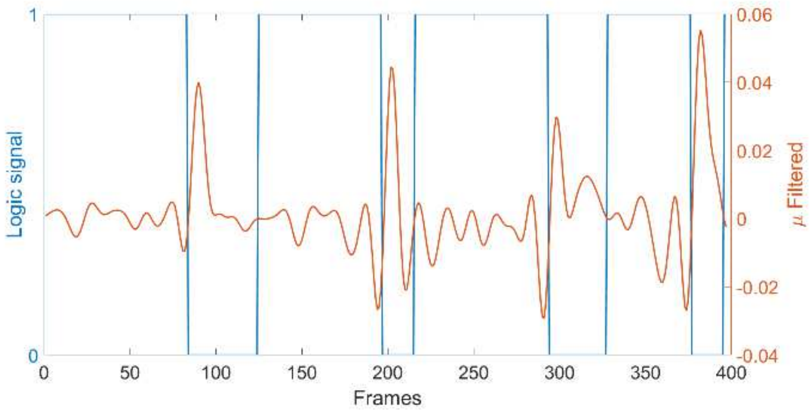

Fig. 11. Eye state prediction from the optical flow estimation algorithm.

1.3.3 IMAGE CORRELATION

This method measures the correlation between each video frame and a reference open-eye template, which is assumed to be the first frame in the sequence [69]. The algorithm structure is shown in **Fig. 12**.

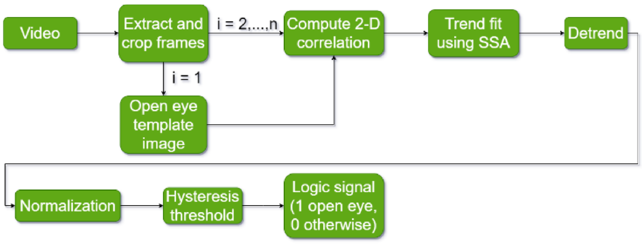

Fig. 12. Image Correlation algorithm.

The correlation coefficient between each frame and the template is computed to create a similarity waveform. During blinks, the eye region changes substantially, reducing similarity with the template image. However, a low-frequency trend may distort this signal. To address this, the SSA technique [70] is applied to isolate and remove the trend component, yielding a detrended signal that more clearly reflects blink dynamics, as can be seen in **Fig. 13**.

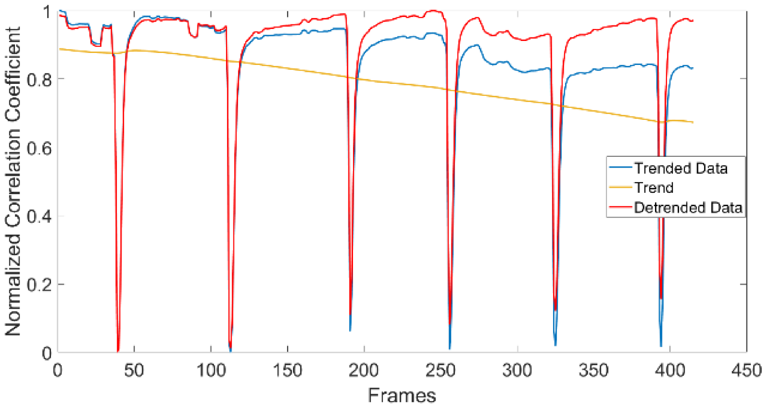

Fig. 13. Correlation coefficient for raw data (blue), trend fit by SSA (yellow) and resulting detrended signal (red).

A hysteresis threshold is then applied to the filtered signal to determine a binary logic waveform (**Fig. 14**) distinguishing open from closed-eye states.

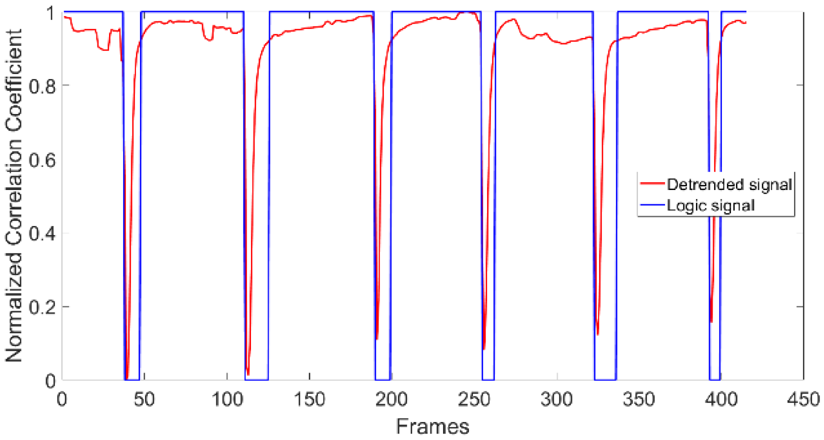

Fig. 14. Eye state prediction using image correlation algorithm.

1.3.4 LOCAL BINARY PATTERN

The fourth algorithm utilizes LBP to quantify texture changes in the eye region during blinking [71], [54]. The pipeline of the algorithm can be depicted in **Fig. 15**.

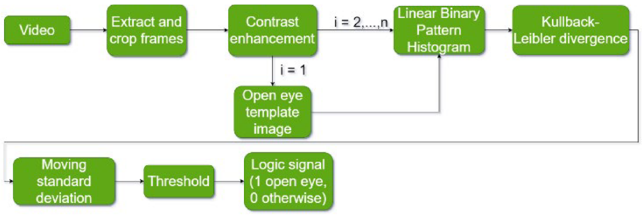

Fig. 15. LBP Histogram algorithm.

After detecting the ROI and applying contrast enhancement, the LBP histogram of the template frame (open eye) is calculated. For each subsequent frame, a histogram is computed using rotation-invariant LBP with 8 neighbors and a radius of 2, resulting in 59 features.

The KL divergence between the current histogram and the template quantifies changes in texture. During a blink, the divergence increases sharply due to eyelid movement. A moving standard deviation with a window of five frames is applied to smooth the raw signal, as can be seen in **Fig. 16**.

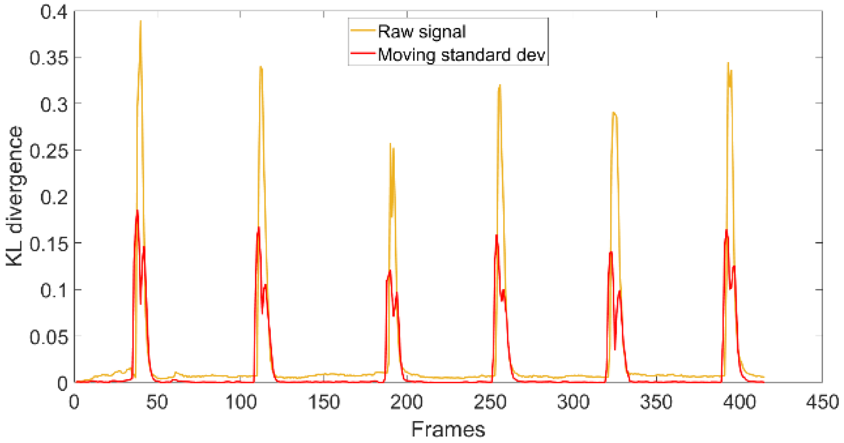

Fig. 16. Raw divergence signal (yellow) and filtered signal by moving standard deviation (red).

Finally, a threshold equal to the average of the signal is applied to the signal, extracting the refined logic signal that delineates between open and closed-eye states. The resulting logic signal is shown in **Fig. 17**.

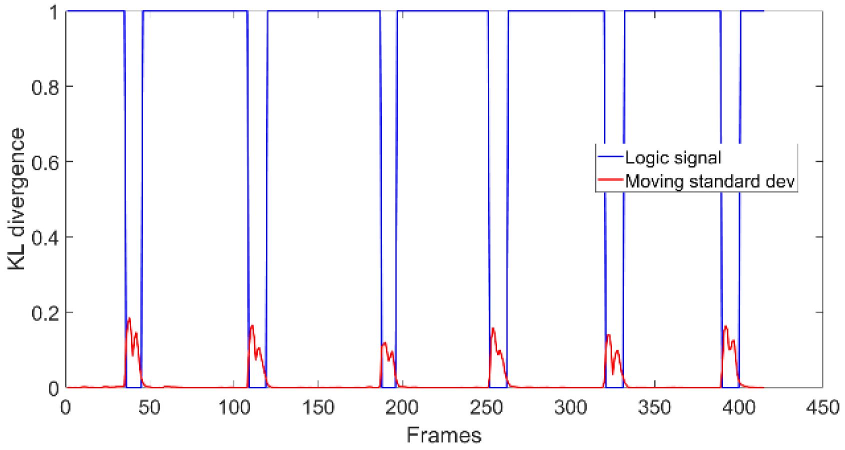

Fig. 17. Eye state prediction using LBP algorithm.

1.3.5 GABOR DECOMPOSITION

The final method is based on GD and is structured as shown in **Fig. 18.**

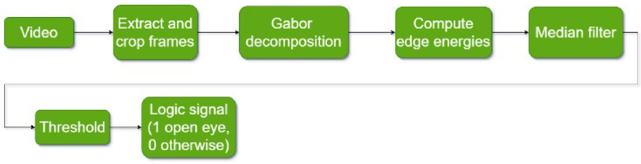

Fig. 18. Gabor Decomposition algorithm.

Each frame of the video sequence is convolved with a Gabor kernel tailored to be optimally responsive to eye blinking, characterized by a scale of 3 and an orientation of 7, as described in [72]. This process results in a filtered image denoted as $G(x, y|u, v)$, where (x, y) are the coordinates of the pixel, whereas (u, v) are the scale and orientation of the Gabor kernel, respectively. The output response $G(x, y \mid u, v)$ is summed across all pixels to obtain a global energy response $O(u, v)$ for each frame, as can be depicted in **Fig. 19**.

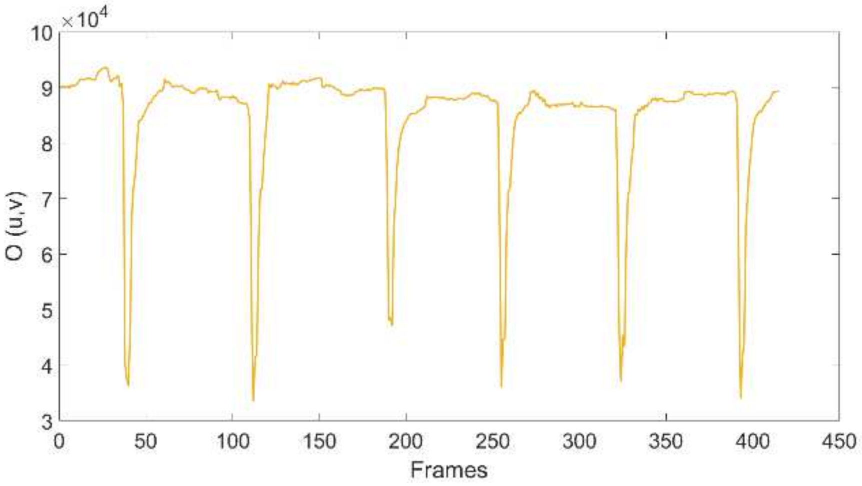

Fig. 19. Cumulative sum of Gabor response signal.

This raw signal is then smoothed using a 3rd-order median filter to reduce high-frequency noise (**Fig. 20**).

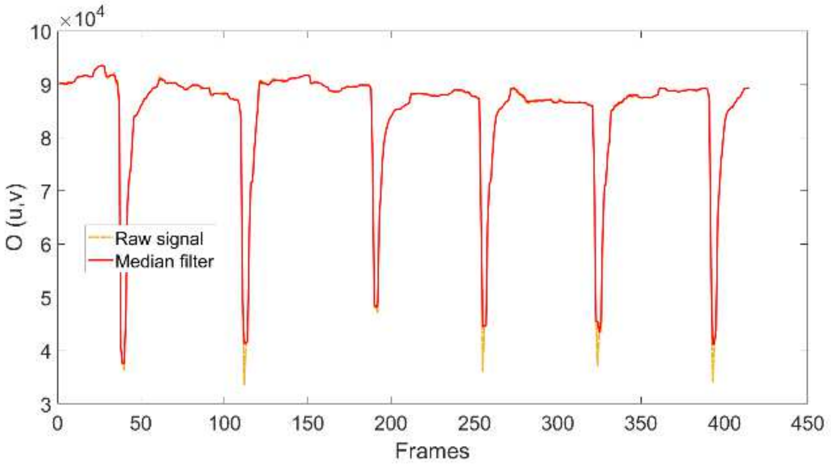

Fig. 20. Raw signal (yellow) and filtered signal after median filtering (red).

Finally, a logic signal is obtained by thresholding the filtered response at its mean value, effectively discriminating between open and closed-eye states (**Fig. 21**).

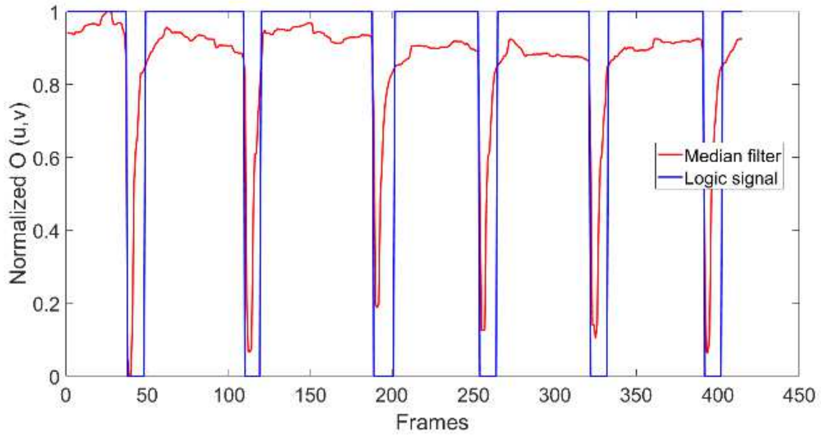

Fig. 21. Eye state prediction using Gabor Decomposition algorithm.

1.4 THRESHOLDING

Both iris area detection and image correlation algorithms need to threshold a raw signal to obtain the result of classification. This is done by applying two thresholds, a low-level and high-level threshold, named thL and thU, respectively. An example is shown in **Fig. 22**.

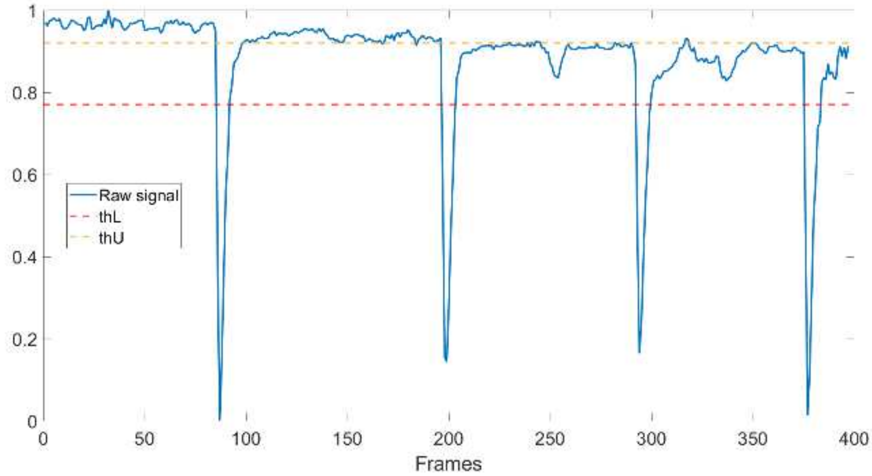

Fig. 22. Hysteresis threshold applied to the raw signal.

These threshold values are computed by solving an optimization problem that maximizes the mean F1-score of the classifier for all the acquired videos and for each channel. These values are reported in **Table 2**.

	Th. level	R	G	B	Grayscale

Algorithm 1	thL	0.82	0.72	0.78	0.78
	thU	0.87	0.93	0.91	0.92
Algorithm 3	thL	0.77	0.77	0.77	0.81
	thU	0.92	0.89	0.89	0.90

Table 2. Hysteresis threshold values.

On the other hand, the second algorithm, which is based on the motion vectors, does not need the application of a threshold to obtain a logical signal. In this case, the optimized parameters are related to the optical flow estimator. In particular, the number of pyramid levels and the neighborhood size. Numeric values are reported in **Table 3** for each channel and for the grayscale image.

	Parameters	R	G	B	Grayscale
Algorithm 2	Pyramid levels	2	2	2	2
	Neighborhood size	21	17	15	17

Table 3. Optical flow estimator parameters.

1.5 DISCUSSION

To evaluate and compare the performance of the five unsupervised algorithms previously described, two different classification strategies were adopted. The first approach, referred to as frame-wise classification, labels each frame as either an open-eye or closed-eye state. This method allows for a detailed assessment of the algorithm's behavior on a per-frame basis, providing insights into its precision and sensitivity in detecting blink-related frames.

In addition to the frame-level analysis, a second, higher-level approach, termed event detector, was used. Here, each blink was considered as a temporal event composed of a continuous sequence of frames where the eye is closed. The output of each algorithm was compared against a manually labeled ground truth that identified the exact onset and offset of each blink. A blink was considered correctly detected if the predicted event overlapped temporally with the annotated one.

1.5.1 FRAME CLASSIFIER

Each frame is classified as open or closed state. Dealing with a binary classification problem, four different cases can be defined:

1. TP, when the classifier predicts a closed eye state, and the eye is closed.
2. FP, when the classifier predicts a closed eye state, but the eye is open.
3. TN, when the classifier predicts an open eye state, and the eye is open.
4. FN, when the classifier predicts an open eye state, but the eye is closed.

Typically, the period of closing eyes is much smaller than that of opening eyes because the eyes will be closed when blinking. Therefore, the number of closed-eye images is much smaller than that of open-eye images, indeed each acquired video is intrinsically an imbalanced dataset, as can be seen in **Fig. 23**.

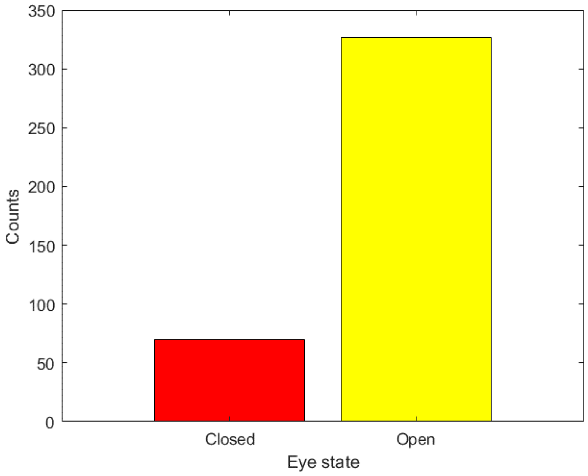

Fig. 23. Number of frames with closed eye (red) and number of frames with open eye (yellow).

Dealing with imbalanced data is a prevalent problem while performing classification on the datasets[73]. Most of the imbalanced classification literature has been devoted to binary classification problems, where one class significantly outnumbers the other. In two-class problems, the minority (underrepresented) class is usually referred to as the positive class, whereas the majority class is assumed to be the negative one[74]. Indeed, in the study case, the positive class is related to the closed eye, whereas the negative one refers to the open eye state. The metrics defined for the frame classifier are summarized in **Table 4**:

Accuracy	$\frac{TP+TN}{TP+TN+FP+FN}$
Precision	$\frac{TP}{TP+FP}$
Sensitivity	$\frac{TP}{TP+FN}$
F1-Score	$\frac{2 \times Sensitivity \times Precision}{Sensitivity + Precision}$

Table 4 - Evaluation metrics for the frame classifier

The results of the frame classifier for each metric and image color channel, obtained by applying the five different algorithms can be depicted in **Table 5**.

Method	Channel	Accuracy	Precision	Sensitivity	F1-score
Algorithm 1	Red	89,4	93,5	63,1	75
	Green	75	59,6	80,4	65
	Blue	84	77,6	75,2	73,2
	Grayscale	82,4	66	77,2	69,6
Algorithm 2	Red	83,5	61,9	84,9	70,3
	Green	85,2	64,6	85,4	73,1
	Blue	85,3	64,4	89,4	74,4
	Grayscale	83,5	61,4	86,2	71,6
Algorithm 3	Red	87,1	94,9	53,1	64,7
	Green	87,1	91,5	53,4	65,2
	Blue	82,2	77,2	59,1	61,4
	Grayscale	84,9	81,4	55,7	62,7
Algorithm 4	Red	85,9	81,1	57,8	66,1
	Green	85	77,2	59,7	65,1
	Blue	83,7	74,4	60,9	64
	Grayscale	85,1	77,9	60	65,6
Algorithm 5	Red	87,6	86,6	60,5	69,7
	Green	87,5	86	62,4	70,4
	Blue	87,7	86,5	63,3	71,1
	Grayscale	87,9	87,2	62	70,9

Table 5. Results of the frame classifier.

As can be seen in **Table 5**, the accuracy reaches the maximum value when the first algorithm is applied to the red channel of the RGB video frames. Due to the imbalanced dataset, the accuracy alone is not sufficient to describe the classification, so other metrics must be comprehensively considered. In terms of accuracy, it is evident that the third algorithm demonstrates the highest performance when applied to the red or green channels. On the other hand, the fifth algorithm exhibits the best performance for the blue channel and the grayscale image.

On the contrary, the sensitivity is higher when the second algorithm is employed. Moreover, the best results in terms of F1-score are achieved when the first algorithm is applied to the red channel.

1.5.2 EVENT DETECTOR

The event detector is used to verify if one predicted blink occurs within the GT blink signal, where GT refers to the actual eyeblinks that exist in the eyeblink signal.

Three different cases could happen and can be classified as:

1. TP, when there is an intersection between the ground truth blink and the predicted blink frames (**Fig. 24a**).
2. FP, when the classifier predicts a blink, but it is not in the ground truth. (**Fig. 24b**).
3. FN, when an eye blink that occurs in the GT is not detected by the classifier (**Fig. 24c**).

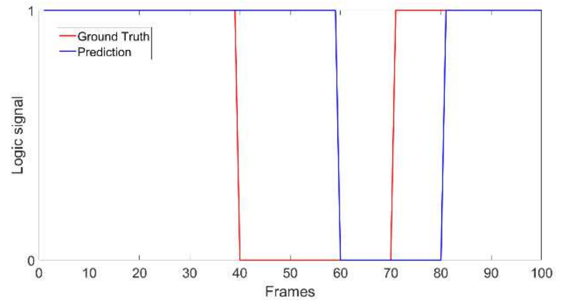

a)

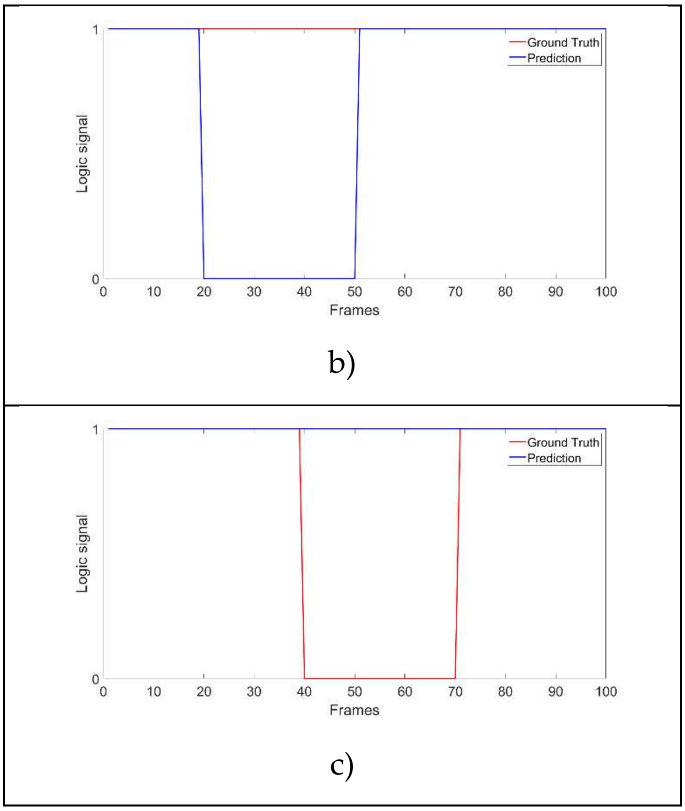

b)

c)

Fig. 24. Three different cases for the event detector.

Hence, the event detector classifies an eye blink as TP when the predicted eye blink overlaps with the GT. A FP arises when the predicted blink frames indicate an eye blink event, but there is no corresponding occurrence in the ground truth data. Lastly, a FN occurs when an eye blink that is present in the ground truth data is not detected by the classifier.

Indeed, since there is no possibility to define TN for the event detector, the metrics employed to assess the performance of the event classifier are summarized in **Table 6**:

Precision	$\frac{TP}{TP + FP}$
False Discovery Rate (FDR)	$\frac{FP}{FP + TP}$
Sensitivity	$\frac{TP}{TP + FN}$
Accuracy	$\frac{TP}{TP + FP + FN}$

Table 6. Evaluation metrics for the event detector.

The results of the event classifier are summarized in **Table 7**.

Method	Channel	Accuracy	Precision	Sensitivity	FDR
Algorithm 1	Red	100	100	100	0
	Green	100	100	100	0
	Blue	90	90	100	10
	Grayscale	100	100	100	0
Algorithm 2	Red	100	100	100	0
	Green	100	100	100	0
	Blue	100	100	100	0
	Grayscale	100	100	100	0
Algorithm 3	Red	100	100	100	0
	Green	95	95	100	5
	Blue	95	95	100	5
	Grayscale	95	95	100	5
Algorithm 4	Red	71,9	71,9	100	28
	Green	66,9	66,9	100	33
	Blue	63,7	63,7	100	36
	Grayscale	67,9	67,9	100	32
Algorithm 5	Red	100	100	100	0
	Green	89,3	89,3	100	11
	Blue	82,7	82,7	100	17
	Grayscale	90,6	90,6	100	9,4

Table 7. Results of the event detector.

As can be seen in **Table 7**, both accuracy and precision reach 100% when the red channel is used, except for the fourth algorithm. Considering the sensitivity, it can be said that all algorithms, applied to all channels, detect 100% of happened eye blinks. Lastly, the false discovery rate is useful to understand which algorithm introduces fewer false blinks. More in-depth, the red channel is the most suitable channel to be considered because in those cases the observed FDR is zero, except for the fourth algorithm.

1.6 CONCLUSION

The primary objective of this study has been to evaluate and compare the performance of the proposed iris area calculation technique with four commonly employed unsupervised, image-based methods for detecting eye blinks. This evaluation has been conducted using a cost-effective system to capture a sequence of external eye images.

For each algorithm, a frame classifier, which detects eye state, and an event classifier, which detects eye blinks from an acquired video have been analyzed. More in-depth, comparison between these algorithms has been done for each RGB channel and for conversed grayscale images. The performance of frame classifiers has been analyzed considering the F1-score to consider both the precision and sensitivity of the model, while accuracy, precision, sensitivity and false discovery rate have been considered to compare the event classifiers.

In light of the results observed for the frame classifier and the event detector, it has been demonstrated that, when an RGB camera is available, the best algorithm for detecting eye blinking is the one based on the iris area applied to the red channel, whereas if a grayscale camera is used, the second algorithm is superior. For the frame classifier, the best results have been obtained with the novel algorithm, which is based on the iris area calculation, obtaining a valuable precision of 93%. In addition, the most suitable color channel to correctly detect if eyes are open or closed is the red (R) one due to the highest F1-score. However, it has also been found that, when higher sensitivity to closed eye is required, calculation of optical flow on the blue channel produces an improved sensitivity of 89%, at the expense of a precision of less than 70%.

Regarding the event detector, all five algorithms applied in our experiments to the red channel reached a 100% detection rate for eye blinks. However, the fourth algorithm applied to the red channel reached a FDR of 28%, whereas the others did not detect false blinks.

In conclusion, it is evident that the novel algorithm, grounded in iris area detection, consistently outperforms the other four methods in terms of F1-score for the frame classifier. Regarding the event detector, when this method was applied in our experiments to the red channel, it reached a 100% detection rate with no false blinks, showcasing its effectiveness in detecting eye blinks.

CHAPTER 1

CHAPTER 2

NOISE ROBUSTNESS OF BLINK DETECTION ALGORITHMS[3]

INTRODUCTION

Eye blink detection plays a crucial role in a wide range of applications, from human–computer interaction and driver drowsiness monitoring to clinical diagnostics and ocular health assessment [53], [76], [77], [78]. In these contexts, the ability to accurately detect eye blinks is highly dependent on the quality of the acquired images. However, in real-world scenarios, image quality is often degraded by various noise sources, such as sensor imperfections, environmental lighting variations, and transmission artifacts. This degradation can significantly impact the performance of image processing algorithms, resulting in reduced detection accuracy and reliability.

While **By** integrating ECG analysis with the ocular-based metrics developed in previous chapters, this final part of the thesis expands the proposed framework toward multi-parametric health monitoring, where cardiovascular and ocular signals can be jointly interpreted to provide a more comprehensive understanding of IOP dynamics and ocular biomechanics in relation to systemic physiological states.

---

[3] This Chapter is based on [75].

INTRODUCTION

Chapter 1 presented a comparative evaluation of five unsupervised image processing algorithms for eye blink detection in noise-free conditions, the present study investigates their robustness when operating on noisy data. The selected algorithms include:

1. Iris Area Detection (IAD), algorithm #1
2. Optical Flow Estimation (OF), algorithm #2
3. Image Correlation (IC), algorithm #3
4. Local Binary Pattern (LBP), algorithm #4
5. Gabor Decomposition (GD), algorithm #5

Many studies have investigated blink detection, but few have focused on the effect of noise on blink detection algorithms. This study addresses this gap by evaluating the robustness of five non-supervised, image-based algorithms for eye blinking detection when noisy images are considered. Although real-world scenarios include various sources of noise—such as camera sensor characteristics, acquisition parameters like shutter speed, and lighting conditions [79], the presence of Gaussian noise is generally considered a good approximation. Consequently, modeling noise as a Gaussian distribution is a common assumption in the literature [80], [81], [82]. In this work, robustness to Gaussian noise is evaluated by artificially adding zero-mean Gaussian noise to the original images. Additionally, the effect of intrinsic quantization noise is also taken into account.

The algorithms are evaluated in terms of both frame classification (open/closed eye) and event detection (eye blinking), using statistical performance metrics such as precision, recall, and F1-score, which are standard for assessing classifier performance. This noise robustness evaluation is particularly important in applications where acquisition systems operate under uncontrolled conditions. For instance, mobile devices or low-cost cameras—frequently used in telemedicine and portable monitoring systems—are more prone to introducing sensor noise [83], [84]. In such scenarios, ensuring algorithmic robustness is essential for maintaining reliable detection performance without resorting to expensive hardware or extensive image preprocessing.

The objective of this chapter is to quantitatively assess the impact of noise on the performance of the five algorithms under study. Artificial Gaussian noise is added at different intensity levels to simulate challenging acquisition conditions, enabling a systematic comparison of algorithmic resilience. Both frame-wise classification metrics and event-based detection accuracy are analyzed, providing insights into the degradation patterns of each algorithm and guiding the selection of the most robust approaches for real-world applications.

2.1 ACQUISITION SYSTEM

The imaging system employed in this study is based on the setup already described in **By** integrating ECG analysis with the ocular-based metrics developed in previous chapters, this final part of the thesis expands the proposed framework toward multi-parametric health monitoring, where cardiovascular and ocular signals can be jointly interpreted to provide a more comprehensive understanding of IOP dynamics and ocular biomechanics in relation to systemic physiological states.

Chapter 1, which comprises an ophthalmological chin rest to minimize head movements during acquisition and an iOS smartphone mounted on a Cartesian positioning system.

For the experiments presented in this chapter, the acquisition system was used to expand the dataset described in the previous chapter, introducing two key modifications aimed at increasing dataset heterogeneity and enhancing the challenge for the blink detection algorithms under evaluation:

1. Lighting conditions were varied compared to the original configuration in **By** integrating ECG analysis with the ocular-based metrics developed in previous chapters, this final part of the thesis expands the proposed framework toward multi-parametric health monitoring, where cardiovascular and ocular signals can be jointly interpreted to provide a more comprehensive understanding of IOP dynamics and ocular biomechanics in relation to systemic physiological states.

2. Chapter 1, to include a broader range of illumination scenarios.
3. Camera frame rate was increased from 30 FPS to 60 FPS, while maintaining the same spatial resolution of 848 × 464 pixels and an RGB bit depth of 24 (8 bits per channel).

These adjustments were designed to make the dataset more representative of real-world conditions and to provide a more stringent test for the algorithms under study.

After image acquisition, Gaussian noise was artificially added to the sequence of frames. This choice was motivated by the fact that Gaussian noise is one of the most common noise models in digital imaging devices [34–36] and produces alterations that are challenging to remove. The added noise has zero mean and a variance ranging from 0 to $10\sigma_q^2$, where σ_q^2 is the variance associated with quantization noise. For an 8-bit depth image, the possible pixel values range from 0 to 255, resulting in a quantization step size $\Delta = 1$. Assuming that the quantization error is uniformly distributed in the interval $\left[-\frac{\Delta}{2}, +\frac{\Delta}{2}\right]$, which holds if the image is well-exposed and utilizes the full dynamic range of the sensor, the standard deviation of the quantization noise is:

$$\sigma_q = \frac{\Delta}{\sqrt{12}} \approx 0.29$$

The chosen noise variance range was determined empirically, as increasing the variance beyond $10\sigma_q^2$ did not yield appreciable changes in the performance metrics of the evaluated algorithms. Gaussian noise was independently added to each RGB channel of the color images or to the grayscale images, depending on the specific analysis being conducted. This approach enabled performance evaluation of the algorithms on each image channel individually.

Fig. 25 shows an example of an original grayscale image, the same image corrupted with Gaussian noise variance $\sigma^2 = 0.04$, and the same image corrupted with the maximum Gaussian noise variance considered.

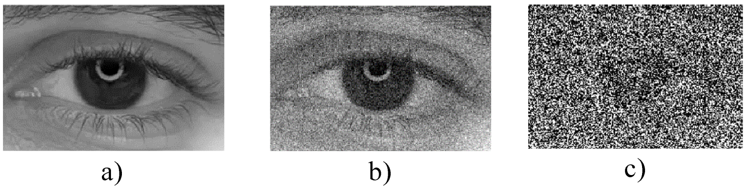

a) b) c)

Fig. 25. a) Original grayscale image, b) noisy image with added Gaussian noise variance $\sigma^2 = 0.04$ and c) noisy image with the highest added Gaussian noise variance.

In addition to the artificially introduced Gaussian noise, images inherently contain intrinsic noise determined by the characteristics of the acquisition system. This was quantified by repeatedly acquiring a stationary object, specifically, a printed photograph of a participant, to measure the system's baseline noise level. The intrinsic noise standard deviation was found to be $\sigma_i = 1.87$. Thus, the overall noise standard deviation was computed as:

$$\sigma = \sqrt{\sigma_i^2 + \sigma_q^2}$$

The dataset collected with this system contains videos of participants of varying ages, eye colors, and skin tones, recorded over multiple sessions. Each video differs in duration and, therefore, in the number of spontaneous eye blinks, and is captured in both RGB and grayscale formats.

2.2 METHODS

Adding noise to the original images can significantly reduce the performance of eye blinking detection algorithms. Therefore, it is essential to conduct a systematic study to quantify and understand this effect. In this work, a Monte Carlo simulation, a statistical method widely applied in image processing to evaluate algorithm robustness under noisy conditions [85], [86], [87]], is used to assess the performance degradation of five different eye blinking detection algorithms.

The algorithms under investigation, previously described in detail in **By** integrating ECG analysis with the ocular-based metrics developed in previous chapters, this final part of the thesis expands the proposed framework toward multi-parametric health monitoring, where cardiovascular and ocular signals can be jointly interpreted to provide a more comprehensive understanding of IOP dynamics and ocular biomechanics in relation to systemic physiological states.

Chapter 1, are also summarized in

Table 8. To ensure optimal performance, the parameters for each algorithm were computed by solving an optimization problem that maximizes a specific evaluation metric, the F1-score.

Algorithm	Parameters				
Algorithm #1: Iris area detection (IAD)	Threshold Level	R	G	B	Gr
	Low threshold	0.82	0.72	0.78	0.78
	High threshold	0.87	0.93	0.91	0.92
Algorithm #2: Optical flow (OF)		R	G	B	Gr
	Pyramid levels	2	2	2	2
	Neighborhood size	21	17	15	17
Algorithm #3: Image correlation (IC)	Threshold Level	R	G	B	Gr
	Low threshold	0.77	0.77	0.77	0.81
	High threshold	0.92	0.89	0.89	0.90

		R	G	B	Gr
Algorithm #4: Local binary pattern (LBP)	Neighborhood size	8	8	8	8
	Radius	2	2	2	2
Algorithm #5 Gabor decomposition (GD)	Scale	3	3	3	3
	Orientation	7	7	7	7

Table 8.Optimal parameters for each eye blinking detection algorithm.

The Monte Carlo simulation consisted of 100 repetitions, each time using different noise samples. For each repetition, we generated an observation of Gaussian noise that was applied consistently across all five algorithms: the original image is corrupted by additive Gaussian noise, and then the five algorithms are used to detect eye blinking. By doing this, it is possible to evaluate the performance of each algorithm for different Gaussian noise levels. The data flow is depicted in **Fig. 26**.

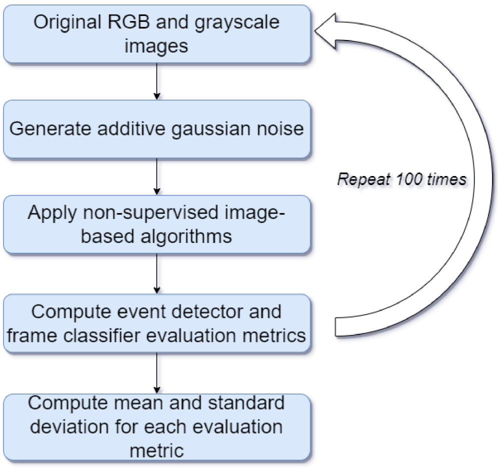

Fig. 26. Montecarlo simulation flowchart.

To evaluate the algorithm's performance, two tasks are considered: the frame classifier and the event detector. The frame classifier is analyzed using sensitivity, precision, and F1-score. These metrics permit us to understand the classifier's ability to correctly detect blinking frames among all true blinks (sensitivity), to avoid misclassification among detected blinking frames (precision), and the harmonic mean of these two metrics (F1-score).

The event detector is evaluated based on similar metrics, which are evaluated on events rather than single frames. These metrics are the FDR, which is equivalent to one's complement of precision, the TPR, which is equivalent to the sensitivity of event detection and the F1-score. The FDR measures the proportion of false positives among all positive detections, crucial for assessing the algorithm's specificity. TPR evaluates the algorithm's effectiveness in correctly identifying actual blinking events. These metrics were chosen because they provide a comprehensive overview of each algorithm's performance, reflecting its accuracy in blink detection and its reliability in avoiding false positives. Moreover, these evaluation metrics are widely used in other state-of-the-art works, where the performance of the eye blinking detection algorithm is exploited [88], [89], [90], [91], [92], [93].

The frame classifier and event detector are evaluated by computing the mean and standard deviation of selected metrics across the repetitions carried out in the Monte Carlo simulation. This evaluation is performed for each algorithm, image channel, noise level, and participant. This comprehensive analysis enables a direct and fair comparison of algorithm robustness under progressively degraded image quality conditions.

2.3 DISCUSSION

To evaluate the influence of Gaussian noise on the five different algorithms, a frame classifier has been defined to classify each frame as either in an open or closed state. Furthermore, since each blink consists of several consecutive frames of the closed-eye state, an event detector is applied to predict the onset and offset of blinks. The reference signal for both event detector and frame classifier, named GT, is a logic signal with a high value (1) when the eye is open and a low value (0) when the eye is closed. This reference signal has been manually determined by considering the moment when the eye changes state.

2.3.1 FRAME CLASSIFIER

The task of the frame classifier is to classify each frame extracted from the acquired video as either an open-eye or a closed-eye frame, based on whether the eye in that frame is open or closed.

Algorithm #1, based on the iris area detection (IAD), initially showed a promising blend of precision and F1-score at low noise levels, indicating its ability to effectively distinguish between true blinks and false positives. However, its relatively low sensitivity suggests difficulties in identifying all true blinking events, a critical consideration for applications where missing real events could have significant consequences. Moreover, while this algorithm performed well at low noise levels, it demonstrated a significant decrease in robustness starting from a noise level of 1.9, beyond which reliable measurements could not be obtained, as can be seen in **Fig. 27**.

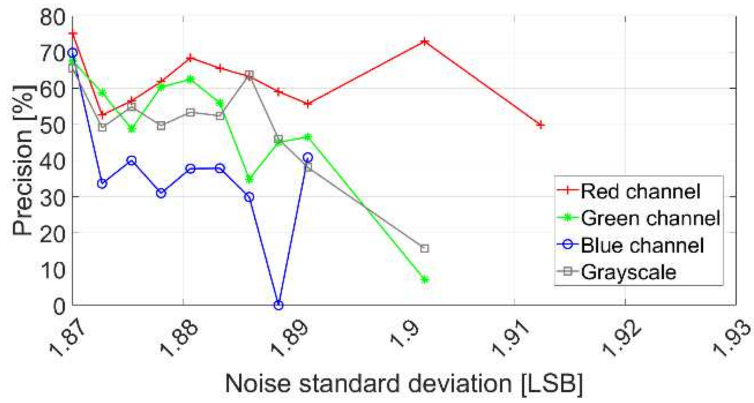

a)

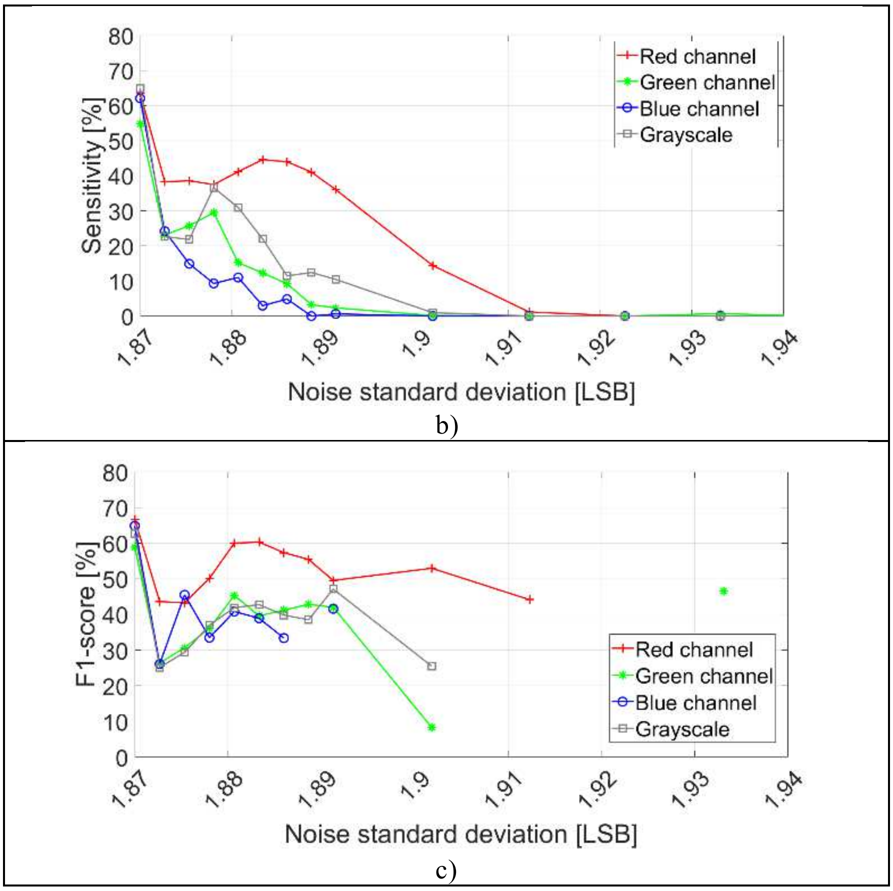

b)

c)

Fig. 27. Evaluation metrics for algorithm #1 (IAD) across different noise levels. Four lines with different colors are displayed (red for the red channel, green for the green channel, blue for the blue channel and gray for the grayscale conversed image).

Importantly, the failure to detect eye status changes is not related to the selection of model parameters, such as the threshold used to convert the raw signal into a logical signal. In that case, the raw signal, which is obtained when the algorithms are applied to the input videos, reveals it to be very noisy, indicating that no threshold adjustment could yield better results, thus emphasizing the algorithm's inherent limitation in handling higher noise levels.

Furthermore, the performance analysis across individual channels reveals that the red channel is generally the most effective for algorithm application, as illustrated in **Fig. 28**. Additionally, it is evident that algorithm #1 (IAD) consistently fails to detect changes in eye state, regardless of the channel considered.

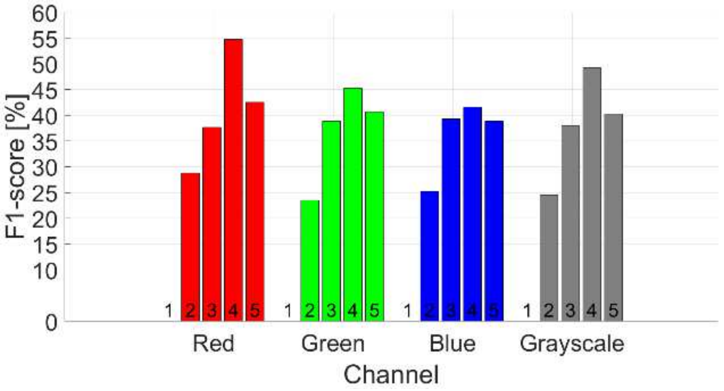

Fig. 28. Performance comparison by algorithm and channel, at the maximum experimented noise standard deviation of 2.07 LSB.

We analyzed the dynamic range of the RGB channels of the eye images to investigate why the red channel performs better in our experiments. We computed the histograms for each channel and determined the span of their dynamic ranges. The analysis revealed that the red channel spans the entire dynamic range [0, 255] more effectively than the green and blue channels, as shown in **Fig. 29**. This indicates that the red channel has better exposure and utilizes the full dynamic range. Consequently, this reveals the superior performance of the red channel in detecting eye blinks.

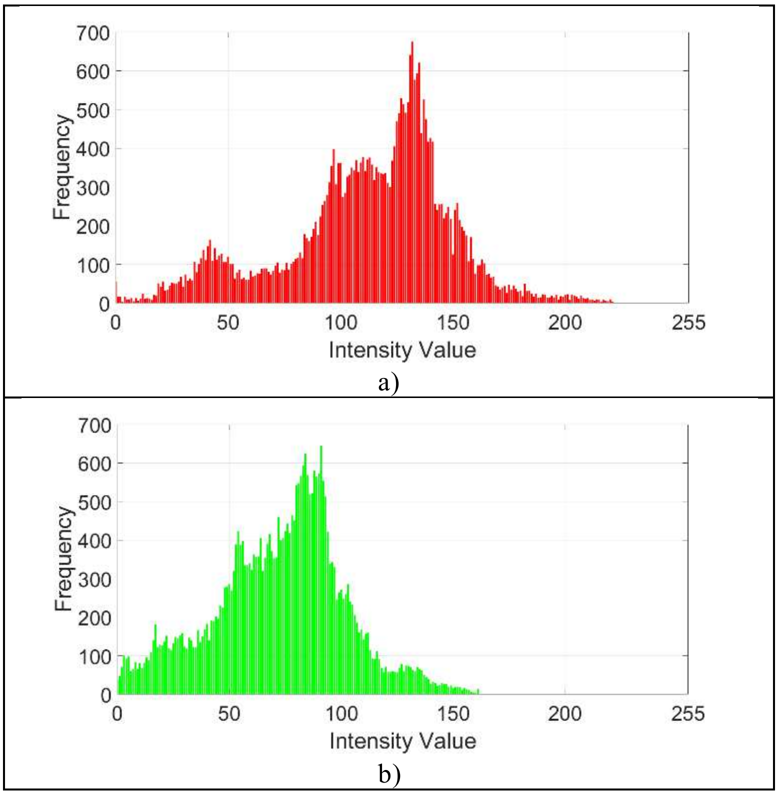

a)

b)

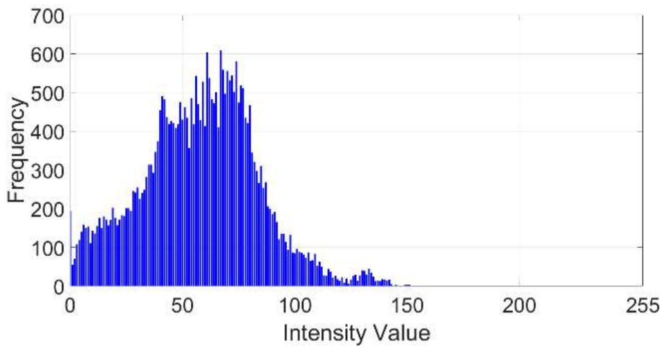

c)

Fig. 29. Histograms of the a) Red, b) Green, and c) Blue channels showing the distribution of intensity values. The Red channel spans the entire dynamic range more effectively than the Green and Blue channels, indicating better exposure and utilization of the dynamic range.

By analyzing model performance for the red channel across different noise levels, as shown in **Fig. 30**, all algorithms experienced performance degradation with increasing noise levels. Through detailed analysis, it became evident how the different algorithms respond to increasing noise levels. Despite algorithm #1 (IAD) performing well at low noise levels, its limited ability to handle higher noise levels restricts its practical utility. In contrast, algorithms #3 based on image correlation (IC), #4 based on local binary pattern (LBP) and #5 based on Gabor decomposition (GD) exhibited greater consistency in performance across a broad range of noise levels, even though with trade-offs between precision and sensitivity.

Added noise levels have been analyzed more densely for values below 0.08, since in that range the performance of most algorithms, except algorithm #3 (IC), falls abruptly.

When no noise is added to eye images, the best F1-score of about 74% is provided by algorithms #4 (LBP) and #5 (GD). However, their performance is below algorithm #3 (IC) when the noise standard deviation is between 1.88 and 1.92. The analysis of these results shows that algorithm # 3 (IC) has an F1-score that varies from 56% to 66% in that range. More in-depth, when delving deeper into the performance data of this algorithm across different image channels, shown in the appendix, the red channel emerges as the superior one, with the highest F1-score.

This indicates that for frame classification tasks within this noise range, algorithm #3 (IC) applied to the red channel of images is the most effective combination, yielding the most accurate results as quantified by the F1-score metric.

When higher noise levels are considered, algorithm #4, based on LBP, emerges as the most balanced candidate because it demonstrates a superior ability to maintain reliable performance even in the case of increasing noise. Also in this case, the optimal channel is the red one, which proved to be more effective in preserving algorithm performance under various noise levels. Therefore, applying algorithm #4 (LBP) to the image's red channel is recommended as the optimal strategy to maximize the effectiveness and robustness of blink tracking in noisy conditions. Conversely, the other algorithms show a continuous decrease in performance, with a lower classification efficacy than a random classifier discerning open or closed eye states.

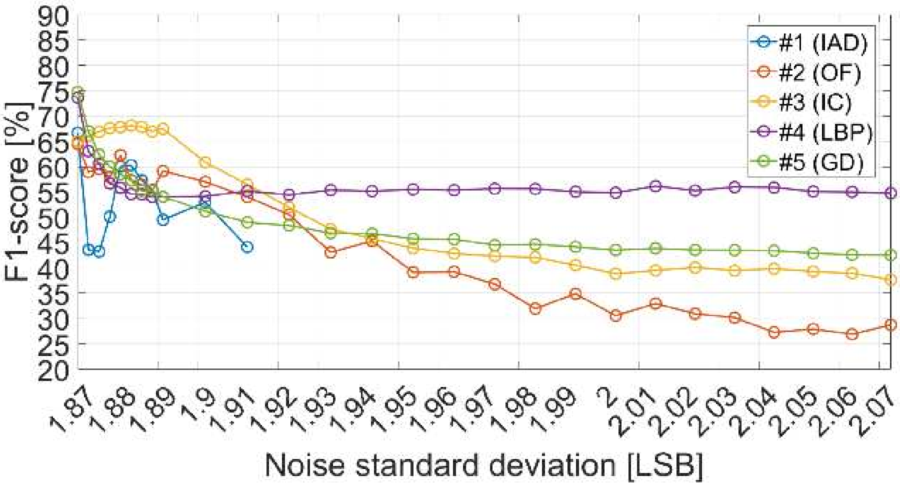

Fig. 30. F1-score across different noise levels when algorithms are applied to the red channel.

2.3.2 EVENT DETECTOR

The event detector considers the blinking as a series of consecutive frames. Thus, its performance is measured by evaluating if predicted blink time intervals overlap with the GT. Its performance across the five analyzed algorithms is evaluated in the presence of additive Gaussian noise.

The evaluation metrics analyzed for the event detector are FDR, TPR and F1-score across all noise levels.

Fig. 31 shows the results for different noise levels, highlighting the red channel's superior performance. It can be seen that algorithm #1 (IAD) struggles at high noise levels, with a decrease in TPR and unstable FDR. On the other hand, both algorithms #4 (LBP) and #5 (GD) deliver a high TPR even in the presence of significant noise, at the cost of a higher FDR.

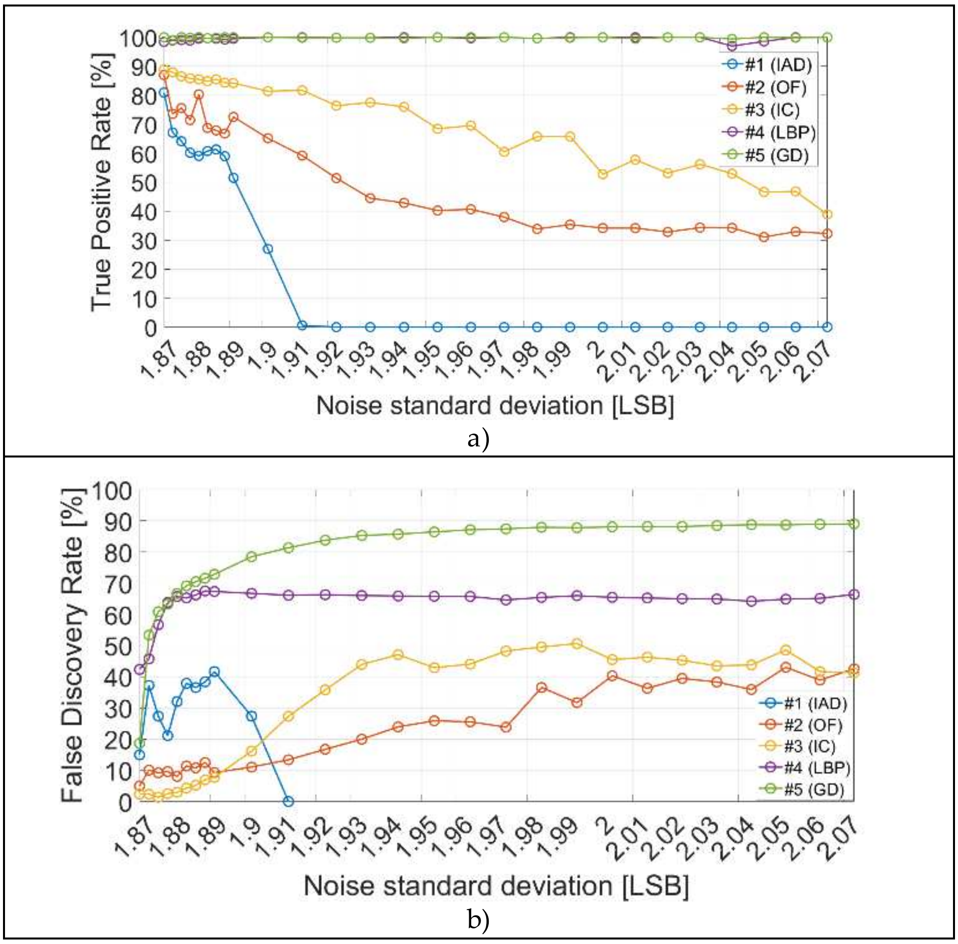

a)

b)

Fig. 31. Variation of a) TPR and b) FDR for all algorithms when applied to the red channel as noise level changes.

Algorithm #1 (IAD) distinguished itself with a low FDR and a relatively high TPR at lower noise levels. However, both metrics significantly deteriorated as noise increased, as shown in **Fig. 32**. Notably, when the noise standard deviation is greater than 1.92 LSB, this algorithm is unable to detect eye state changes.

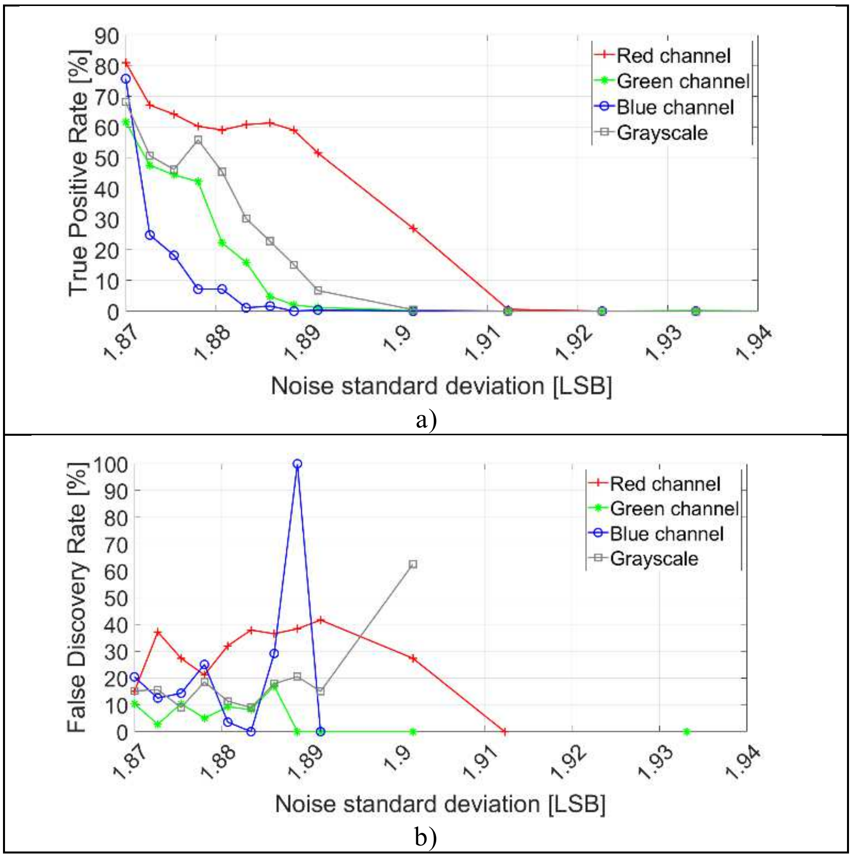

a)

b)

Fig. 32. Results of algorithm #1 (IAD) across different noise levels and channels.

Algorithm #2 (OF) generally overperforms compared to algorithm #1, and also offers better results at high noise levels, as shown in **Fig. 33**.

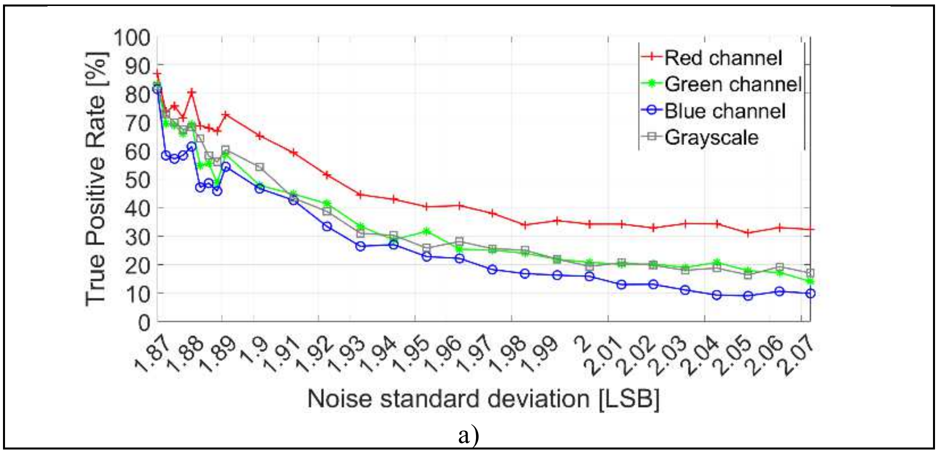

a)

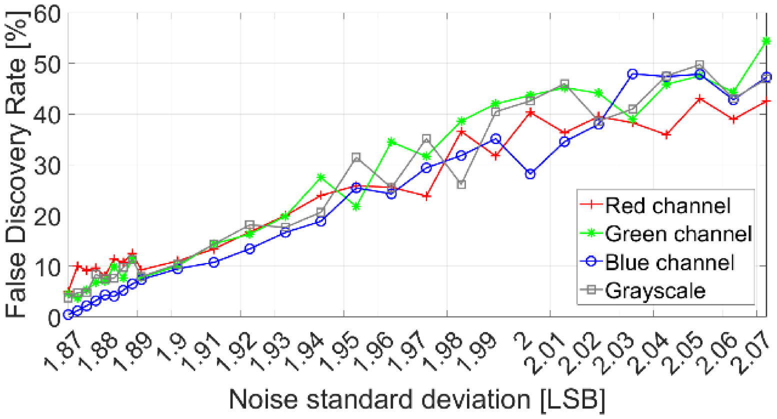

b)

Fig. 33. Results of algorithm #2 (OF) across different noise levels and channels.

By examining the performance of algorithm #3 (IC), based on image correlation, across different channels, the red one emerges as the best, with the highest F1-score, as can be seen in **Fig. 34**. This suggests that when this algorithm, is applied to the red channel, not only accurately detects real events (high TPR) but also has a low probability of false blinking (low FDR), thus offering an excellent trade-off between the two metrics.

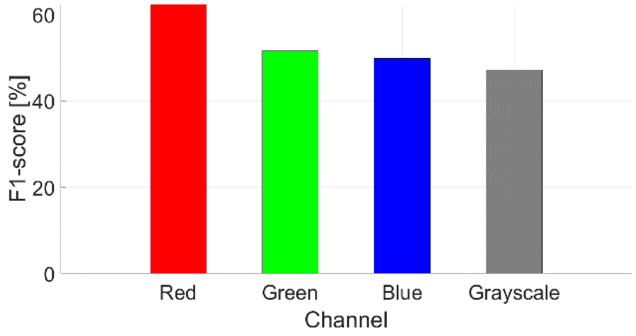

Fig. 34. Results of algorithm #3 for a noise standard deviation of 1.94 LSB.

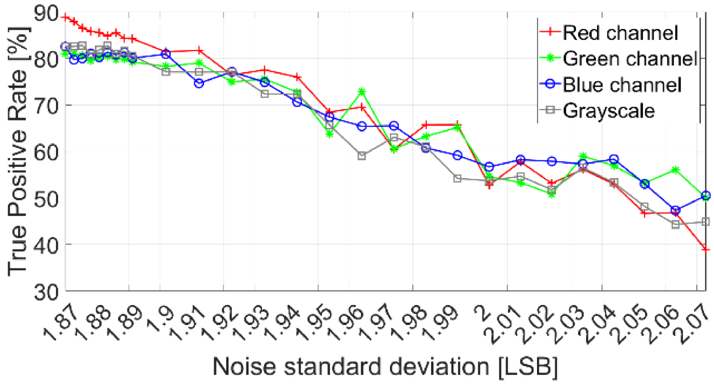

a)

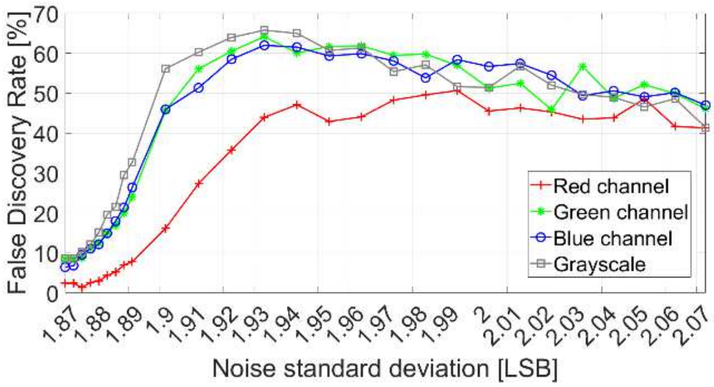

b)

Fig. 35. a) TPR and b) FDR for algorithm #3 (IC) across all noise levels.

Examining **Fig. 35**, it is evident that the performance of this algorithm varies depending on the color channel used and the level of added noise. In **Fig. 35a**, we can observe that all four channels demonstrate a decreasing trend in the percentage of true positives as the noise level increases. The red channel consistently exhibits the highest TPR, suggesting that it is less susceptible to increases in noise compared to the other channels. Moreover, at higher noise levels, the performance of all channels tends to converge.

In **Fig. 35b**, there is an opposite trend compared to the TPR. As the noise level rises, the FDR increases for all channels. The red channel starts with the lowest rate of false discovery and reaches a value in the range of 40%-50% at high noise levels. Indeed, the red channel is the one that reaches the best trade-off between low FDR and high TPR.

Algorithms #4 (LBP) and #5 (GD) displayed a relatively stable TPR for all the noise levels. The TPR remains stable and close to 1, even as noise levels increase, because the algorithm predicts more blinking events than are present in the ground truth when noise becomes more prevalent. Indeed, these algorithms have a high sensitivity in identifying blink events, despite an increased rate of false positives. Regarding the FDR, algorithm #4 exhibits a plateau effect when the noise level exceeds 1.9 LSB. On the other hand, algorithm #5 presents a worse FDR at high noise levels.

Fig. 36 shows algorithm #4 performance across different noise levels and channels.

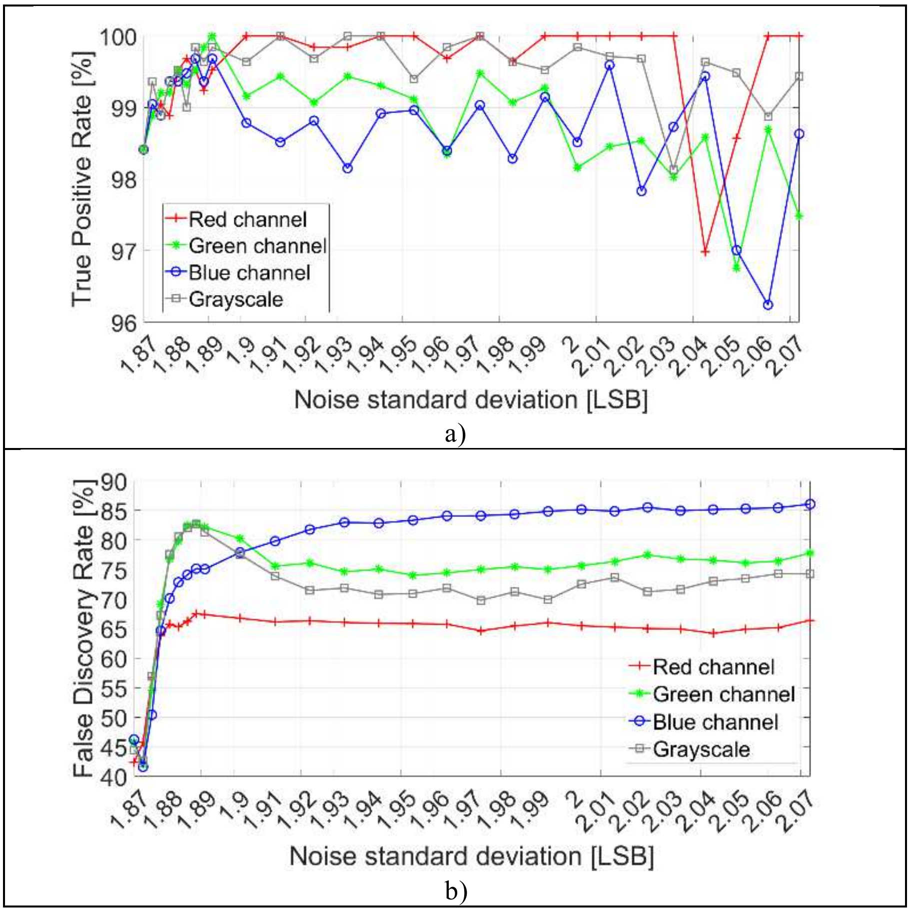

a)

b)

Fig. 36. Results of algorithm #4 (LBP) across different noise levels and channels.

Results for algorithm #5 (GD) across different noise levels and channels can be depicted in **Fig. 37**.

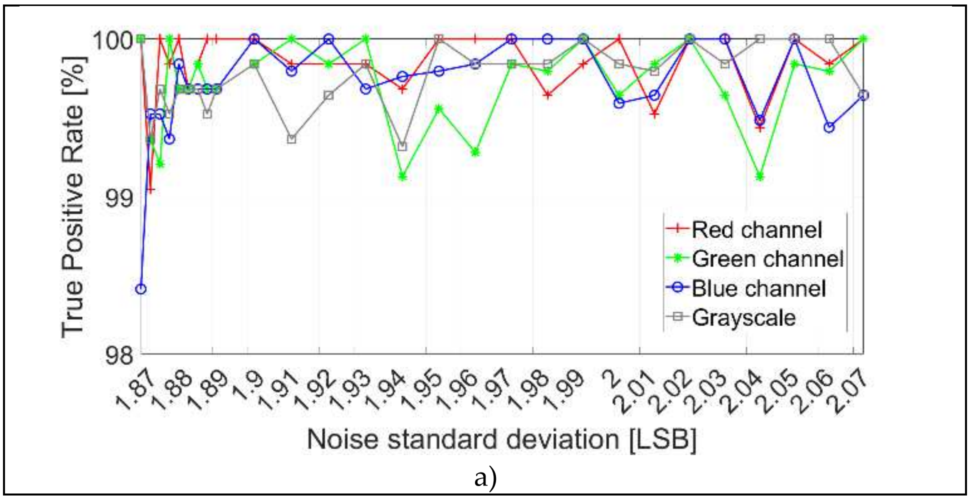

a)

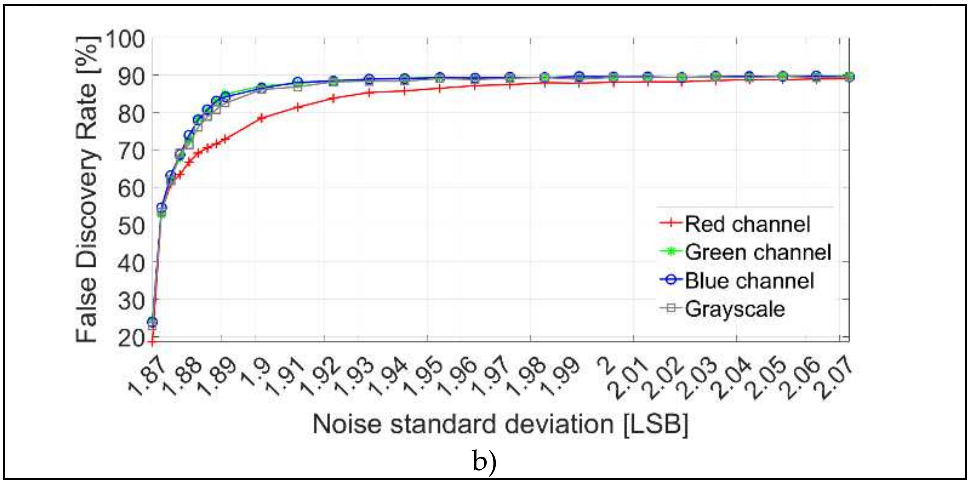

b)

Fig. 37. Results of algorithm #5 (GD) across different noise levels and channels.

For both algorithms, the TPR appears relatively stable for all the noise levels and channels.

As regards the FDR of algorithm #4 (LBP), shown in **Fig. 36b**, the red channel exhibits a good resistance to noise by maintaining a low FDR, outperforming the other channels across a broad spectrum of noise levels. In addition, beyond a noise level of 1.89 LSB, it reaches a plateau, indicating no increase of FDR when there is an increase in noise level. As can be seen in **Fig. 37b**, the FDR of algorithm #5 (GD) follows a similar trend across all channels. Initially, when there is no added Gaussian noise in the images, (1.87 LSB), the FDR for all channels is less than 30%. As the noise standard deviation increases, the FDR for all channels starts to increase, suggesting that the system mistakes noise for actual events more frequently. This trend plateaus at around 1.94 LSB for green, blue and grayscale channels, meaning that beyond this point, the noise does not significantly affect the FDR. The red channel, however, performs slightly better (lower FDR) than the other at almost all noise levels, suggesting that it may be more reliable for detecting eye blinking.

Thus, similarly to other algorithms, the channel that maximizes performance in noisy settings is the red one. Indeed, if algorithm #4 (LBP) is applied to the red channel, it exhibits low FDR in the case of high noise levels.

Conclusively, algorithm #3 (IC) based on image correlation emerged as the most robust against noise in event detection for blink tracking, which makes it the ideal choice for real-world applications faced with noisy images. Especially when applied to the red channel, it provides an optimal balance between accurate blink detection (high TPR) and minimizing false positives (low FDR), obtaining a higher F1-score, as can be seen in **Fig. 38**.

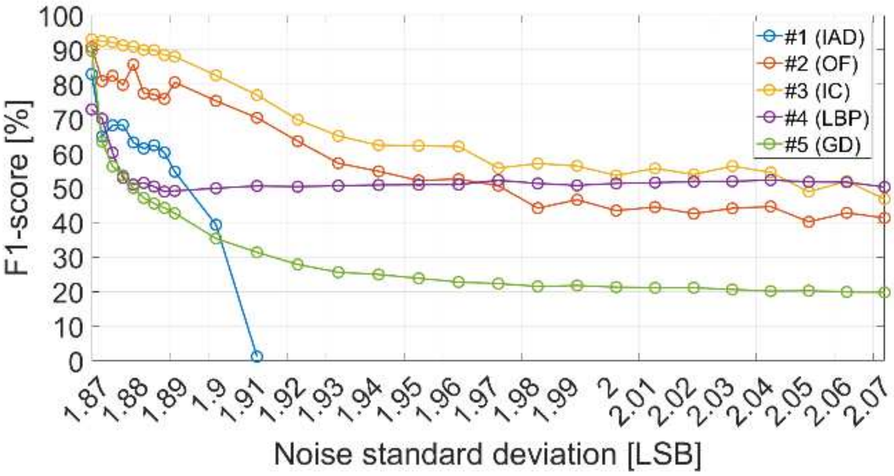

Fig. 38. Variation of F1-score for all algorithms when applied to the red channel as noise level changes.

2.4 CONCLUSION

In this chapter, we investigated the robustness of five non-supervised, image-based algorithms for eye blinking detection under varying levels of Gaussian noise. The evaluation was carried out considering both frame classification (open/closed eye) and event detection (blink onset/offset), providing a comprehensive comparative analysis. The results clearly show that noise has a significant detrimental impact on all tested algorithms, with the degradation becoming more pronounced as the noise level increases.

At low noise levels, Algorithm #3 (IC), based on image correlation, outperformed the others for both frame classification and event detection, with the red channel yielding the highest performance. However, its frame classification performance dropped sharply when the noise standard deviation exceeded 1.92 LSB, indicating limited robustness in high-noise conditions.

Conversely, Algorithm #4 (LBP), relying on local pattern analysis, demonstrated a superior ability to maintain a higher F1-score even at elevated noise levels. For the red channel, the LBP-based frame classifier showed only a moderate decline in F1-score, from 75% in noise-free conditions to about 55% at the highest tested noise level, confirming its resilience to noise corruption.

Regarding event detection, Algorithm #3 (IC) proved particularly effective in maintaining a low false discovery rate (FDR) across noise levels, outperforming the other algorithms in this respect.

Overall, the analysis highlights that the red channel is generally the most suitable for blink detection due to its better exposure and full utilization of the dynamic range. In summary, Algorithm #3 (IC) emerged as the most robust option for event detection in noisy environments, while Algorithm #4 (LBP) is the recommended choice for frame classification under high noise conditions.

CHAPTER 3

MODELING CORNEAL DYNAMICS DURING BLINKING[4]

INTRODUCTION

The biomechanical properties of the cornea have become an important focus in ophthalmology for the early detection and monitoring of ocular diseases [94]. Corneal biomechanics concerns how the cornea responds to applied forces, undergoes deformation, and subsequently returns to its original shape. In vivo diagnostic tools currently available to assess these properties include the Corvis ST, Ocular Response Analyzer, tonometry, and dynamic corneal imaging techniques, the latter based on dynamic ultra-high-speed Scheimpflug imaging or optical coherence tomography devices [95], [96], [97], [98], [99], [100]. Numerous studies have demonstrated the clinical relevance of biomechanical metrics for identifying and characterizing various ocular pathologies. **Table 9** provides an overview of some of the most widely used parameters.

Parameter	Description

---

[4] This Chapter is based on [2].

Deformation Amplitude (DA)	Vertical displacement of the corneal apex at the highest concavity
Peak Distance (PD)	Distance between the two peaks of the cornea at the time of highest concavity
Radius at Highest Concavity (HCR)	Radius of curvature at the time of highest concavity
Highest Concavity Time (HCT)	Time to reach the highest concavity of the cornea
Time of First Applanation (A1T)	Time from stimulus onset to first applanation
Time of Second Applanation (A2T)	Time from stimulus onset to second applanation
Velocity at First Applanation (A1V)	Speed of the corneal apex at the first applanation
Velocity at Second Applanation (A2V)	Speed of the corneal apex at the second applanation

Table 9. Overview of key corneal biomechanical parameters commonly used to assess ocular diseases.

For example, in keratoconus, a progressive corneal disorder characterized by thinning and conical deformation, parameters such as DA and HCR differ significantly from healthy eyes due to reduced corneal stiffness [101], [102]. In severe myopia, studies have shown greater DA and smaller HCR compared to controls, suggesting lower stiffness and greater deformability [103], [104]. In dry-eye patients, analysis with the Corvis ST has revealed a statistically significant increase in the HCT, indicating a more compliant cornea caused by epithelial and stromal layer alterations [105], [106].

In ocular hypertension and early-stage glaucoma, elevated IOP can also affect corneal dynamic response. Wang et al. [107] reported that, in POAG patients, DA and A2T were significantly lower, while A1T, A2V, and PD were significantly higher compared to healthy controls, indicating reduced deformability.

While these instruments provide valuable quantitative measures of corneal biomechanics, they are typically invasive or require close contact with the eye. More importantly, they necessitate clinical settings, making frequent measurements or continuous monitoring impractical.

To overcome these limitations, this chapter introduces the concept of corneal profile dynamics, which involves analyzing corneal deformation during a natural physiological process: the blink. The eyelid exerts a transient flattening force on the corneal surface during blinking, temporarily altering its profile [108]. Analyzing these short-lived deformations offers an opportunity to derive novel biomechanical metrics that could be useful in detecting and monitoring ocular diseases.

The primary aim of this study is to assess the intra-subject variability of these newly extracted metrics during complete, natural blinks. Multiple recordings are acquired from the same subject, and the variability is quantified by calculating the standard deviation of each metric. This approach provides a baseline for future comparative studies involving patients with ocular pathologies. Furthermore, an illustrative example is presented to demonstrate how these metrics can be applied to detect changes in IOP.

3.1 IMAGING SYSTEM

The imaging system developed to track the corneal profile during natural eye blinking is illustrated in **Fig. 39a**. The setup consists of a modified ophthalmology slit lamp equipped with an imaging lens (focal length: 50 mm; numerical aperture: 0.18; Thorlabs, Newton, NJ) and a high-speed camera (Allied Vision, Edmund Optics, Barrington, NJ) capable of acquiring images at 510 FPS. The camera was positioned laterally to the participant's eye to capture the corneal profile throughout the blinking process.

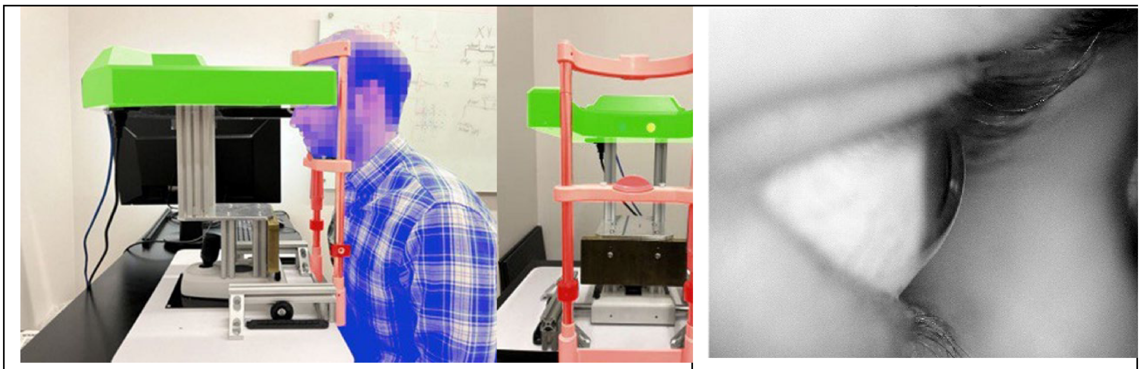
a)

b)

Fig. 39. High-speed imaging system to track corneal profiles during a blink. (a) Side and front views of the imaging system. The green area represents the chassis housing the cameras and lenses, the blue one corresponds to the patient, and the red structure is the modified chin rest where the patient rests his head for image acquisition. (b) An example of the lateral eye image acquired with the imaging system.

Videos were recorded in 8-bit grayscale format at a spatial resolution of 800 × 600 pixels. The high frame rate, although essential to accurately capture the rapid deformation of the cornea during a blink, implies a reduced exposure time. To compensate for this limitation and ensure optimal image quality, a visible LED ring light, mounted concentrically with the camera lens, was employed as the illumination source.

Fig. 39b presents an example of a lateral eye image acquired with the proposed system, illustrating the level of detail achievable under the described acquisition conditions.

The dataset used in this study consists of 10 videos acquired while the participant performed natural blinking, resulting in a total of more than 200 recorded blink events.

3.2 METHODS

The analysis of corneal dynamics during a natural, complete blink was organized into a sequence of processing stages, illustrated schematically in **Fig. 40**.

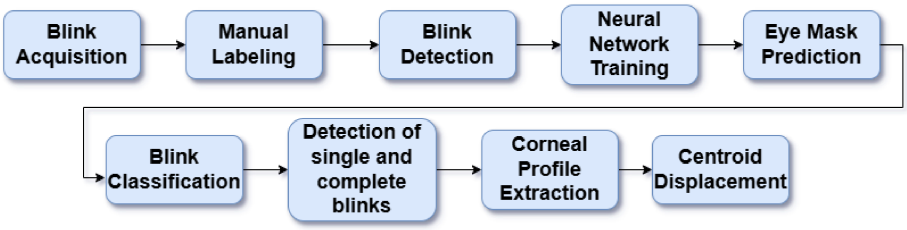

Fig. 40. Workflow overview for cornal dynamics analysis.

The workflow begins with the acquisition of 10 high-speed videos in which the participant performs natural blinking multiple times. Following data collection, a manual labeling phase is carried out to establish the ground truth for subsequent analysis. For each blink, the start and end frame are manually annotated, together with its type, *single* or *multiple*, and its completeness, *complete* or *incomplete*. In addition, binary ocular masks are manually generated for all relevant frames, providing reference segmentations of the ocular region. This manually labeled dataset serves as a benchmark to evaluate the performance of the automated blink detection, classification, and segmentation processes.

Automatic blink detection is performed using the IC method [69], which compares the similarity between a reference open-eye frame and each subsequent frame in the sequence. Once blinks are detected, they are classified into four distinct categories:

1. Complete blink – the eyelids close entirely, covering the cornea.
2. Incomplete blink – the eyelids partially close, leaving part of the cornea exposed.
3. Single blink – a single blink occurs before the eye reopens.
4. Multiple blinks – more than one blink occurs before the eye reopens.

A U-Net neural network supports the automatic classification of blinks [109], trained to predict ocular masks for all detected blink frames to quantify the variation of the ocular area during blinking. The performance of this segmentation network is assessed using standard binary classification metrics, specifically accuracy, precision, sensitivity, specificity, and F1-score [110], [111]. For subsequent biomechanical analysis, only *complete* blinks are selected, excluding incomplete or multiple blinks to ensure consistency of the dynamic measurements. The corneal profile is then extracted from the segmented masks using a custom-developed MATLAB script, enabling precise tracking of the corneal contour throughout the blink opening phase. This profile data serves as the basis for the dynamic analysis of corneal motion.

3.2.1 NEURAL NETWORK TRAINING

Four eye-opening sequences, each extracted from a different video among the ten available, were manually annotated frame by frame, starting from the fully closed eye and continuing until the eye was fully open. This labeling process produced approximately 1,000 annotated images, which served as the training dataset for the segmentation model.

The segmentation network employed was a U-Net, designed specifically for ocular region segmentation. The architecture consisted of convolutional layers with filter sizes ranging from 64 to 512, with a bottleneck layer containing 1024 filters. Batch normalization layers were inserted after each convolutional operation to enhance training stability and convergence [112]. To mitigate overfitting and improve generalization, the training procedure included early stopping and a reduce-on-plateau learning rate schedule. The complete network structure is shown in **Fig. 41**, where the input is a 256×256-pixel grayscale image and the output is a binary segmentation mask.

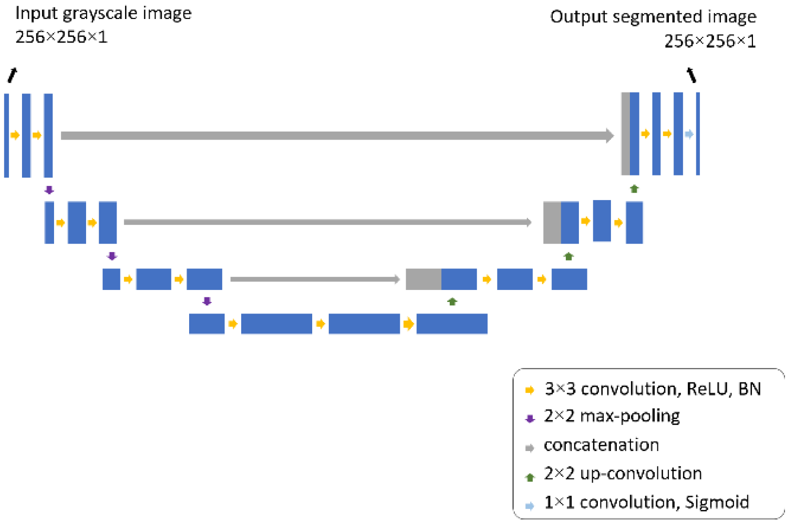

Fig. 41. U-Net architecture for ocular image segmentation. The input image is a 256x256 grayscale image; the output is a binary mask.

Frames from the opening phase of blinking were categorized into four classes based on the proportion of the segmented ocular area relative to its maximum observed value: closed eye (mask area = 0%), semi-closed eye (mask area between 0% and 40%), semi-open eye (mask area between 40% and 80%), and open eye (mask area > 80%). An example of the classification of these frames based on the mask area can be depicted in **Fig. 42**.

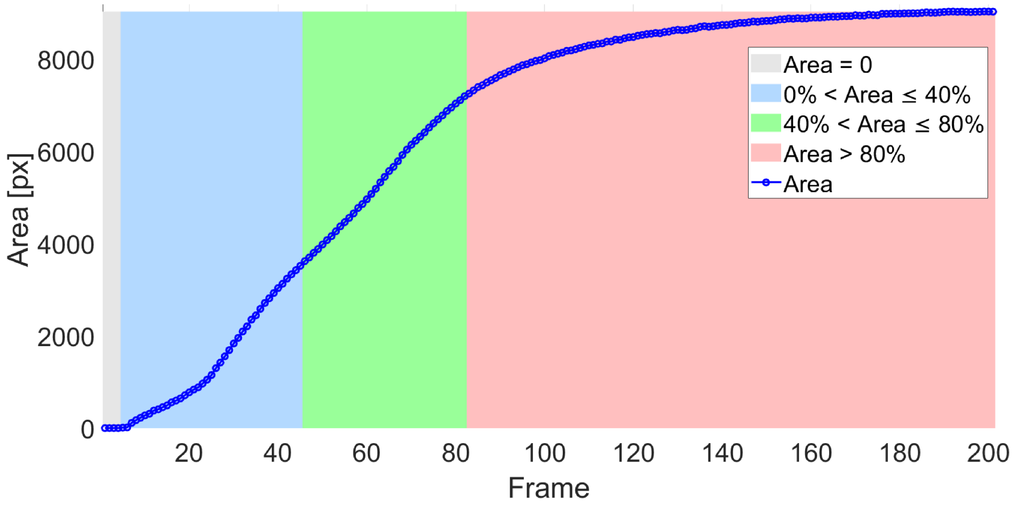

Fig. 42. Example of the classification method based on the mask area. The curve represents the segmented area over the sequence of frames during the eye-opening blink phase.

A notable imbalance was observed, with open-eye frames being the predominant type. To address this, a random resampling strategy was implemented based on the mask area, ensuring an equal number of samples in each class.

To increase dataset diversity and improve model generalization, several data augmentation techniques were applied, including horizontal flipping to account for both left and right eyes, random rotations within ±10° to simulate head pose differences, zoom variations of ±10% in scale, and horizontal and vertical translations up to ±10% of image size to simulate different camera-eye alignments. The dataset was split into 80% training and 20% testing. The model was trained for 300 epochs using the Adam optimizer [113] with an initial learning rate of 10^{-4}. The Combo Loss (CL) function was adopted, defined as:

$$L_{CL} = \alpha L_{BCE} + (1-\alpha)L_{Dice}$$

Where α is set to 0.5.

The Binary Cross-Entropy (BCE) term penalizes per-pixel misclassifications [114], while the Dice Loss emphasizes the overlap between prediction and GT [115]. This combination enhances segmentation accuracy, particularly in imbalanced datasets [116], [117].

The training and validation loss curves are shown in **Fig. 43**, while **Fig. 44** reports the Intersection over Union (IoU) evolution during training. On the test set, the model achieved an IoU of 97%, confirming its capability to accurately segment the ocular region.

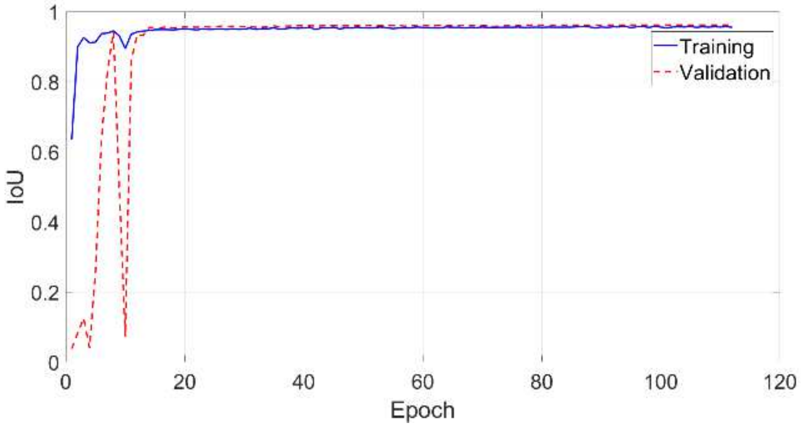

Fig. 43. Loss function for the training and test subsets.

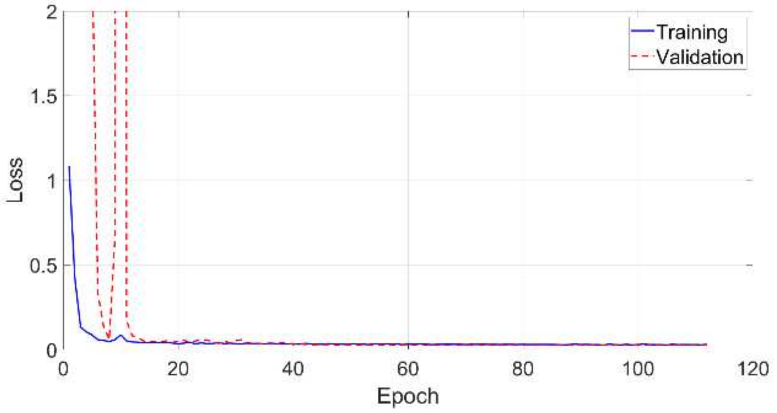

Fig. 44. IoU metric for the training and test subsets.

3.2.2 AUTOMATIC BLINK DETECTION AND CLASSIFICATION

The automated detection and classification of blinks can be performed by analyzing the variation of ocular masks predicted by the neural network. Once the network is trained, it can predict an eye mask for every frame in a video. By analyzing how the area of the eye mask changes over time, blinks can be detected and classified. However, this process is highly time-consuming. Therefore, a faster method was employed, relying on IC to perform a pre-selection of frames in which the blink occurs, followed by the blink classification with the neural network, rather than applying the network to all frames.

Specifically, each video frame was resized to 256 × 256 pixels to standardize the comparison, and the correlation coefficient was computed between the reference frame and each subsequent frame [40], [75]. The reference frame was selected as the first frame of the video, corresponding to the open-eye state. The obtained correlation signal was then smoothed using a first-order Butterworth low-pass filter with a cutoff frequency of 10 Hz to eliminate high-frequency noise while preserving relevant blink-related variations, as can be seen in **Fig. 45**.

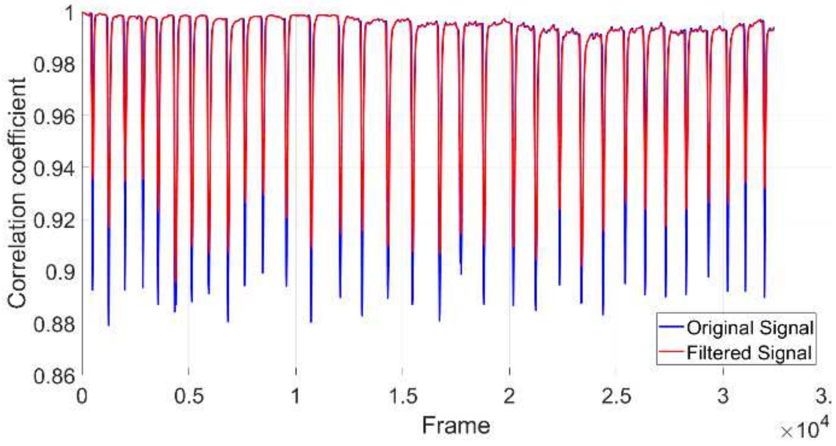

Fig. 45. Automatic blink detection from a video using the IC algorithm. The blue signal shows the correlation coefficient between a reference frame and all the other frames. The red signal is the filtered signal.

To correct the baseline shifts that can occur due to head movements during the acquisition, trend decomposition was applied, based on SSA. The resulting detrended signal was rescaled in the range [0,1].

Blink events were detected as significant negative peaks in the detrended signal. Peaks were identified using a prominence threshold of 10% of the median detrended signal, ensuring robust detection while minimizing false positives. **Fig. 46** illustrates the detrended signal along with the detected local minima corresponding to blink events.

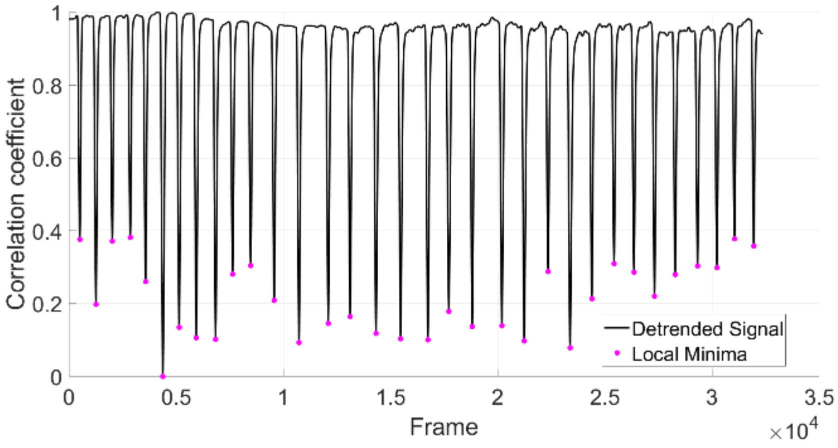

Fig. 46. Automatic blink detection using IC technique. Each local minimum of the signal represents a blink.

The start and end of each blink were determined based on the moving standard deviation of the detrended signal, computed using a window size of 10 frames. For each blink, an initial threshold was set at 10% of the mean moving standard deviation. This threshold was used to identify the boundaries of the blink as the first frame before the peak and the first frame after the peak where the standard deviation is below the threshold. If a valid interval, defined as having a start frame occurring before the peak and an end frame after the peak, was not found, the threshold was increased iteratively by 10% in each iteration. This process was repeated until a valid interval was found or a maximum of 100 iterations were reached. An example of detected blinks from the acquired video using the approach described above can be depicted in **Fig. 47**.

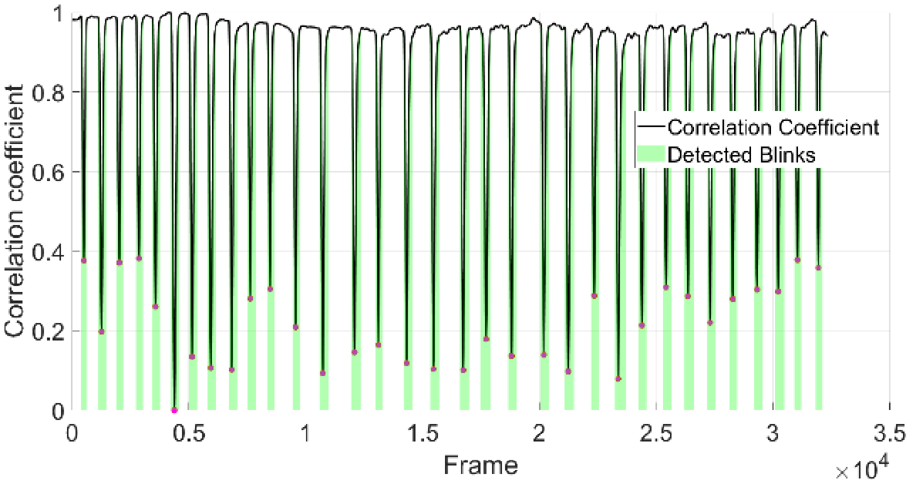

Fig. 47. An example of detected blinks using the automatic method described above.

This approach enables the automatic detection of all blink occurrences in the video without initially classifying their nature (complete/incomplete, single/multiple). Once the blink events are detected, the neural network is employed to predict eye masks on the eye blinking frames determined by the IC. To classify each detected blink, we analyze the temporal variation of the ocular mask area obtained from the neural network predictions. Specifically, we examine the presence and number of local minima and assess whether the mask area reaches zero. This information allows us to categorize blinks into complete or incomplete, and single or multiple. In **Fig. 48** different mask area profiles corresponding to various types of blinks are illustrated.

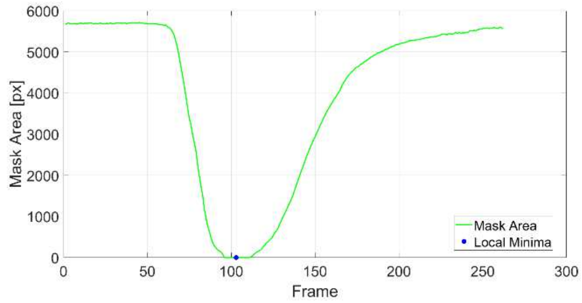

a) Complete and single blink: the area reaches zero and only one local minimum is detected.

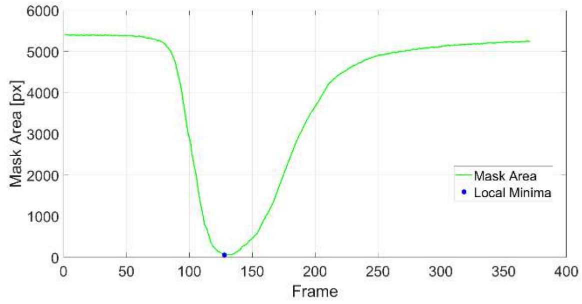

b) Incomplete and single blink: the area does not reach zero and only one local minimum is detected.

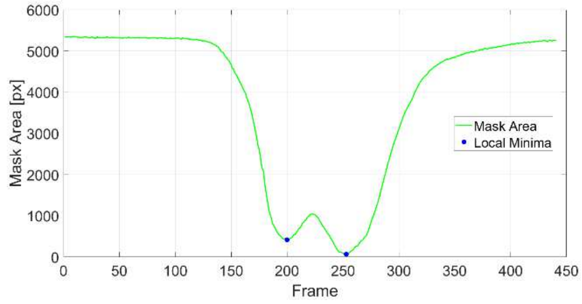

c) Incomplete and multiple blink: the signal contains more than one local minimum (two) and does not reach zero at either of them.

Fig. 48. Examples of automatic blink classification based on the temporal variation of the ocular mask area.

The automatic blink detection method based on IC achieved a 100% blink detection rate, accurately identifying all blink events across the analyzed videos. Regarding the classification of these blinks, the performance of the proposed approach is summarized in the confusion matrices shown in **Fig. 49**, highlighting its effectiveness in distinguishing between complete and incomplete blinks, as well as single and multiple blinks.

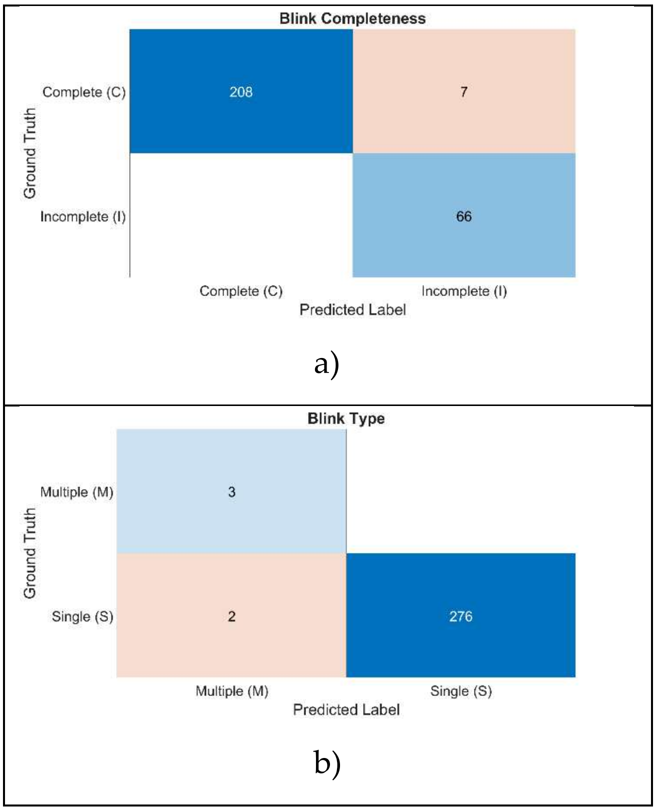

Fig. 49. Confusion matrices for the blink classification task. a) Classification performance for blink completeness (complete vs. incomplete). b) Classification performance for blink type (single vs. multiple).

The metrics used to evaluate the performance of the classifier are summarized in **Table 10**.

	Blink completeness	Blink type
Accuracy	0.975	0.993
Precision	1.00	1.00
Sensitivity	0.967	0.992
F1-score	0.983	0.996
Specificity	1.00	1.00

Table 10. Classification performance metrics for the two blink classifiers (completeness and type), including accuracy, precision, recall, and F1-score.

This strategy optimizes computational efficiency by avoiding the application of the neural network to the entire video while ensuring an accurate characterization of each blink that occurs in the acquired videos. Only complete and single blinks are considered when assessing corneal dynamics.

3.2.3 CORNEAL PROFILE EXTRACTION

After the prediction of ocular masks using the trained U-Net, the corneal profile for each eye-opening frame was extracted through a series of processing steps. The first step involved calculating the centroid of the predicted mask, defined as the geometric center of its pixel distribution. Masks without a valid centroid, such as empty masks or those containing multiple disconnected regions, were excluded from further analysis.

An example of the mask predicted by the neural network is shown in **Fig. 50**.

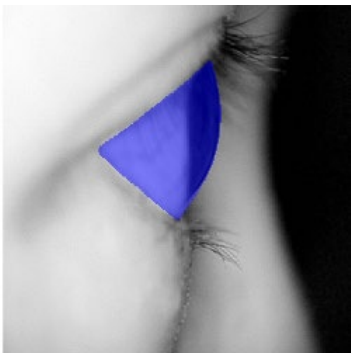

Fig. 50. Example of an original eye image and the corresponding predicted mask (in blue) obtained using the trained U-Net model.

To extract the corneal profile, the external border of the mask was computed. Pixels located to the right of the centroid were then analyzed to identify two key points: the upper-right pixel and the lower-right pixel. The upper-right pixel was determined as the farthest pixel above the centroid along the y-axis, selected based on the Euclidean distance from the centroid. Similarly, the lower-right pixel was identified as the pixel with the minimum y-coordinate below the centroid. **Fig. 51** illustrates the process of identifying these two key points.

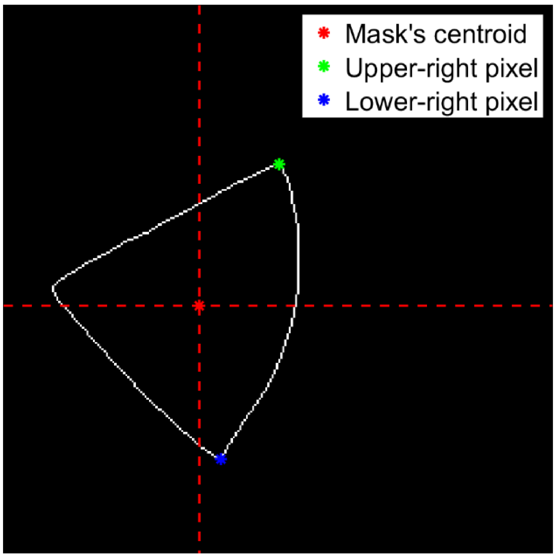

Fig. 51. Identification of key points on the external border of the mask to isolate the corneal profile.

With the upper-right and lower-right points determined, a geodesic distance algorithm [118] was employed to compute the shortest path along the external border of the mask between these two points. The geodesic path consistently aligned with the corneal profile, ensuring a precise and anatomically accurate delineation for each blinking frame. **Fig. 52** demonstrates the use of the geodesic distance algorithm to extract this profile.

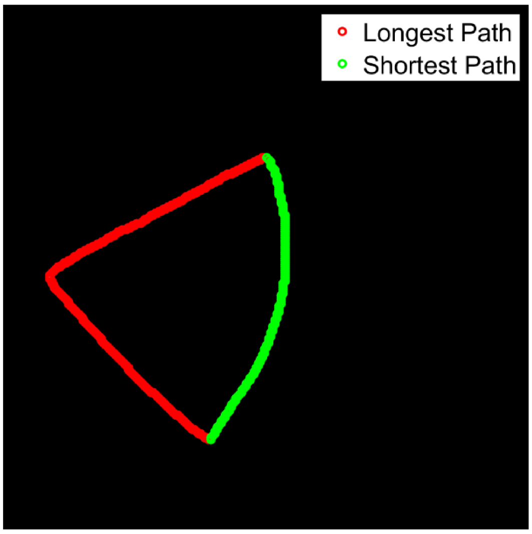

Fig. 52. Geodesic distance algorithm applied to the external border of the eye mask. The green path represents the shortest geodesic path between the upper-right and lower-right points, which consistently corresponds to the corneal profile for every frame of the eye blinking, including frames with the eye slightly open.

3.2.4 CENTROID DISPLACEMENT ANALYSIS

The longitudinal displacement of the centroid of the corneal profile is analyzed to assess its dynamics during the opening phase of a blink. The centroid, defined as the geometric center of a shape, represents the average position of all the points in the corneal profile.

Fig. 53 illustrates how both the corneal profile and its centroid evolve during the opening phase of a blink, highlighting the progressive deformation and subsequent recovery of the corneal surface.

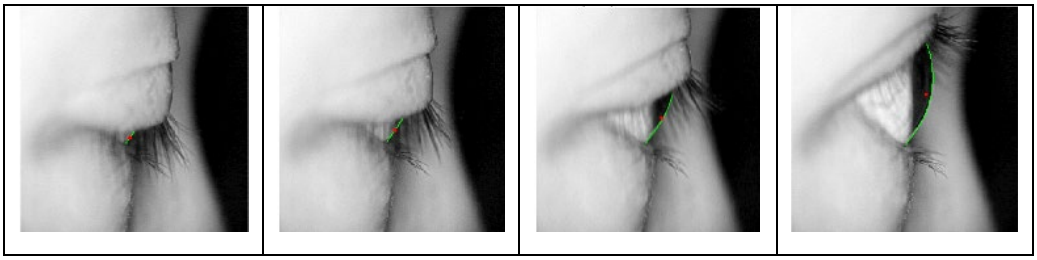

Fig. 53. The evolution of the corneal profile (in green) and its centroid (in red) during the opening phase of a blink.

As can be seen in **Fig. 54**, the longitudinal centroid displacement followed an exponential trajectory, stabilizing when the eye was fully open. Indeed, it was modeled with an exponential fitting function defined as:

$$y(t) = A\left(1 - e^{-\frac{t}{\tau}}\right) + B$$

where A represents the displacement amplitude, which measures the extent of longitudinal movement of the corneal centroid, B is the offset, and τ is the time constant, which characterizes the rebound velocity of the cornea after the eyelids exert pressure on the ocular surface.

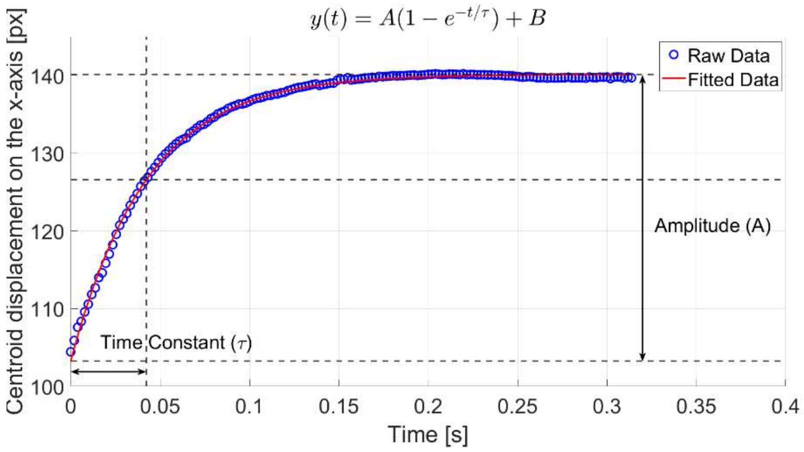

Fig. 54. An example of exponential fitting on the longitudinal displacement of the corneal centroid during the opening phase of a blink.

Potential outliers in the centroid displacement data were removed to improve the fitting performance. Specifically, the first five frames of each blink's eye-opening phase were excluded. In these frames, the corneal profile is often partially obscured by the eyelashes, making it challenging for the neural network to accurately predict the eye mask. By discarding these frames, noise in the data decreased, and the quality of the fitted parameters improved, resulting in a more consistent and reliable description of corneal dynamics.

3.3 DISCUSSION

The automatic detection and classification of all the blinks in the acquired videos described in the previous section identified 206 complete, single blinks suitable for analysis. All the other blinks classified as incomplete or multiple were excluded.

The raw corneal centroid displacement along the x-axis during the eye-opening phase of blinking for a single sample is shown in **Fig. 55**.

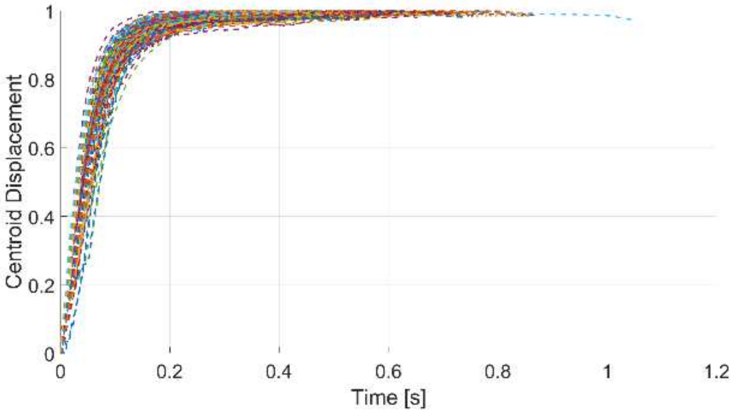

Fig. 55. Raw corneal centroid displacement along the x-axis during the opening phase of a blink. The normalization is applied only for visualization.

Then, the exponential fit is applied to the raw displacement curve to extract the two metrics. The fitted trajectories for all the blinks are shown in **Fig. 56**.

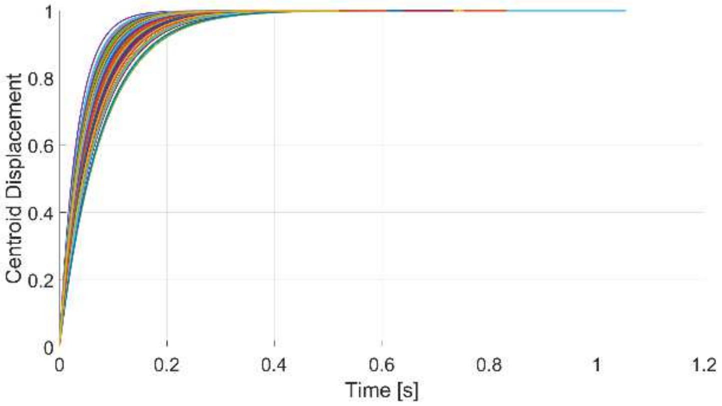

Fig. 56. Longitudinal centroid displacement during the eye-opening phase of blinking. Each curve represents the fitted displacement trajectory for an individual blink. The normalization of the curves is performed only for better visualization.

The fitted curves are then filtered based on their fitting performance. Specifically, only the curves with a $R^2 > \mu_{R^2} + 3\sigma_{R^2}$ and $RMSE < \mu_{RMSE} - 3\sigma_{RMSE}$ are considered for further analysis, where R^2 is the coefficient of determination and RMSE is the root mean square error.

The distribution of each metric is evaluated using the Kolmogorov–Smirnov test to assess normality.

The density distributions of displacement amplitude and time constant are shown in **Fig. 57** and **Fig. 58**, respectively.

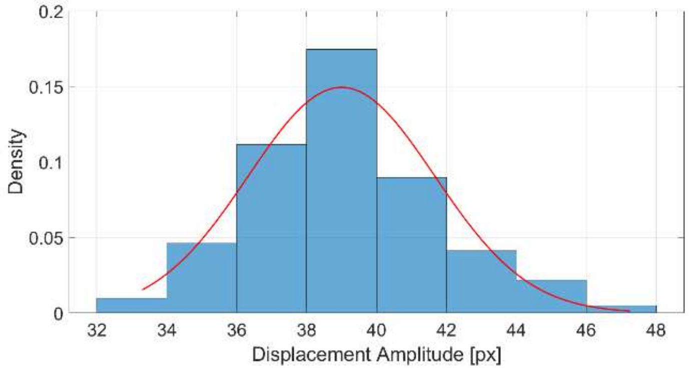

Fig. 57. Distribution of the displacement amplitude across all valid blinks. The overlaid red curve represents a Gaussian fit.

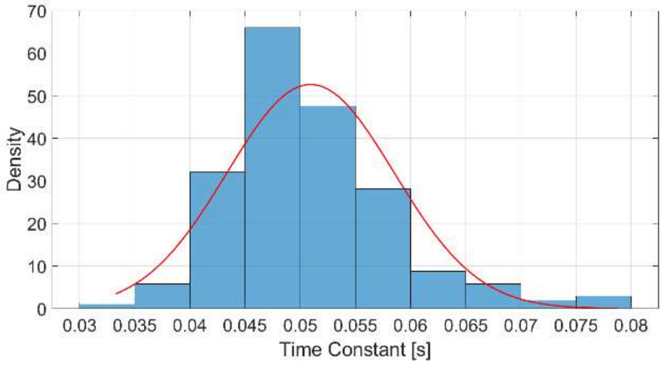

Fig. 58. Distribution of the time constant across all valid blinks. The overlaid red curve represents a Gaussian fit.

The results indicate that both the amplitude and the time constant follow a normal distribution. Specifically, the test yielded a p-value of 0.137 for the amplitude and 0.115 for the time constant. Since both values are above the significance level of 5%, the null hypothesis of normality was not rejected.

To further characterize the system, the mean, standard deviation, minimum, maximum, interquartile range (IQR) and skewness are calculated for both metrics. These results are summarized in **Table 11**.

	Mean	Std	Min	Max	Median	IQR	Skewness
A [px]	39.0	2.67	33.3	47.2	38.6	3.18	0.516
τ [ms]	50.9	7.57	33.3	78.8	49.7	8.50	0.976

Table 11. Statistical Analysis of the two corneal dynamics metrics.

The displacement amplitude exhibits a mean value of 39.0 px with a standard deviation of 2.67 px, indicating moderate variability across samples. The median value of 38.6 px is close to the mean, and the skewness is relatively low (0.516), suggesting a reasonably symmetric distribution. The IQR of 3.18 px further confirms a moderate spread of the data. On the other hand, the time constant presents a higher variability, with a mean of 50.9 ms and a standard deviation of 7.57 ms. For this parameter as well, the median value is close to the mean, while the skewness of 0.976 suggests a slight asymmetry in the distribution. The IQR, equal to 8.50 ms, indicates a relatively narrow dispersion of values around the central tendency.

To explore the potential of corneal dynamics and derived metrics for detecting ocular diseases such as glaucoma, a case study was carried out on a participant different from the one included in the statistical analysis presented above. The subject's IOP was initially measured under baseline conditions using a portable tonometer (iCare IC200). The participant then performed the water drinking test (WDT), a well-established procedure in which IOP is naturally increased by ingesting 1 liter of water within 5 minutes [119], [120], [121]. A subsequent measurement with the portable tonometer confirmed the IOP elevation, showing an increase of 2 mmHg.

Videos were recorded under both baseline and elevated IOP conditions while the participant performed natural blinks. Using the method described earlier, the longitudinal displacement of the centroid of the corneal profile was computed for each blink in both conditions. These results were then compared to assess the presence of statistically significant differences. **Fig. 59** illustrates the centroid displacement traces obtained under baseline (blue curves) and elevated IOP after WDT (red curves).

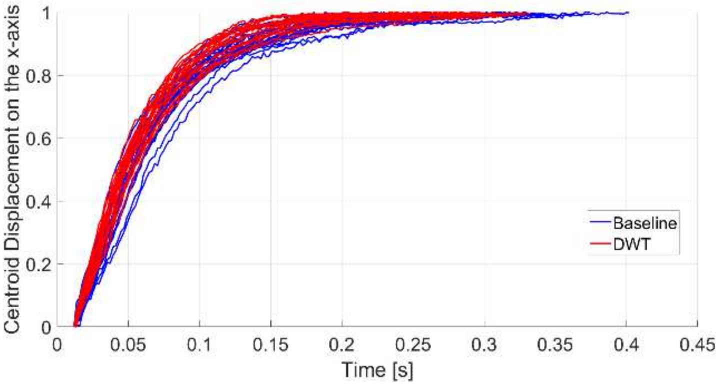

Fig. 59. Longitudinal centroid displacement for baseline IOP (blue) and elevated IOP after DWT test (red).

To quantitatively assess the differences, a two-sample t-test was applied to both displacement amplitude and time constant (**Fig. 60**).

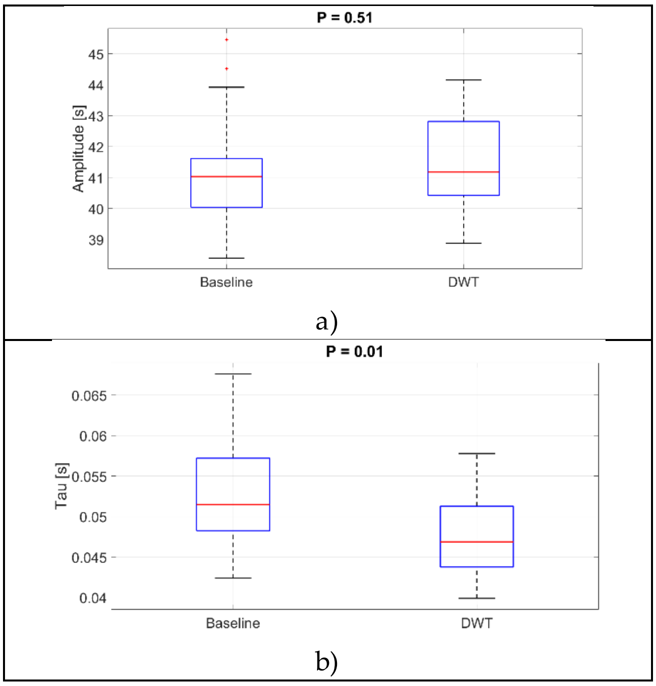

Fig. 60. Two-sample t-test for displacement amplitude and time constant.

Regarding displacement amplitude, the average value was 41.2 ± 0.34 px in the baseline condition and 41.5 ± 0.32 px in the elevated condition. As shown in **Fig. 60a**, this difference was not statistically significant, suggesting that IOP does not influence the extent of corneal profile movement during a blink.

In contrast, the time constant revealed a significant difference between the two conditions: 52.7 ± 1.3 ms at baseline versus 48.1 ± 1.2 ms under elevated IOP ($t = 2.62$, $p < 0.05$). As shown in **Fig. 60b**, the cornea exhibited a faster response when

IOP was elevated, consistent with the hypothesis that higher internal pressure increases the restoring force acting on the cornea.

These findings suggest that the time constant may represent a meaningful metric for capturing IOP variations. Monitoring such variations could contribute to the early detection of IOP-related ocular conditions, including glaucoma.

3.4 CONCLUSION

In this chapter, a novel, non-contact approach for analyzing corneal dynamics during natural blinking was presented, leveraging a high-speed lateral imaging system and advanced image segmentation techniques. By extracting the corneal profile and tracking its centroid displacement over time, two quantitative metrics were defined to describe the corneal response immediately after eyelid pressure release. These metrics demonstrated high repeatability and low intra-subject variability, confirming the reliability of the proposed method for assessing corneal biomechanics.

To preliminarily assess the clinical potential of this technique, a case study was performed in which IOP was artificially elevated using the dark room water drinking test (DWT) and measured with a certified portable tonometer. The differences observed in the extracted metrics between baseline and elevated IOP conditions indicate that corneal dynamics during blinking may encode clinically relevant information related to IOP changes.

Future work will focus on conducting a larger-scale study involving multiple subjects under both baseline and elevated IOP conditions, enabling statistical validation of the proposed metrics' diagnostic capabilities. If confirmed, this non-contact approach could represent a practical alternative to conventional tonometry, enabling continuous, at-home IOP monitoring. By facilitating early detection and timely intervention, it has the potential to significantly improve glaucoma prevention strategies and broaden access to preventive eye care.

CHAPTER 4

ASSOCIATION BETWEEN BLINK-RELATED CORNEAL DYNAMICS AND IOP[5]

4.1 INTRODUCTION

IOP is the sole modifiable risk factor for glaucoma, the leading cause of irreversible blindness worldwide, affecting approximately 3.5% of the global population aged 40–80 years [122], [123]. Accurate assessment and regular monitoring of IOP are, therefore, critical for the early diagnosis and effective management of this ocular disease.

This study explores the potential of blinking, a natural physiological process that plays a key role in ocular lubrication, debris removal, and eye protection [124], [125], as a means to characterize corneal dynamics and investigate its potential dependence on IOP.

Currently, IOP is most commonly measured using tonometry, with the GAT considered the gold standard [126]. However, GAT requires direct contact with the corneal surface, the application of topical anesthetics, and trained personnel. Furthermore, it can only be performed in a clinical setting, making it unsuitable for continuous or home-based monitoring, capabilities that could enable earlier

---

[5] This chapter is based on the paper [1].

detection of glaucoma.

To address these limitations, various technological solutions have been proposed. Smart contact lenses embedded with sensors can provide continuous IOP monitoring [24], [28], [29], yet their corneal contact may be uncomfortable or unacceptable for some patients. Implantable sensors [30], [31] offer direct measurement capabilities but require invasive surgical procedures [32].

In this work, we propose a novel, non-contact method to evaluate corneal dynamics during natural blinking and to assess their correlation with IOP. The method leverages the natural ELP exerted on the corneal surface [33], [34] during a blink to induce measurable corneal deformations. By analyzing these deformations, we aim to provide insight into IOP-related biomechanical changes in the cornea, paving the way for a practical, home-based, and continuous IOP monitoring approach.

4.2 DATA ACQUISITION

4.2.1IMAGING SYSTEM

The high-speed imaging system used in this study is the same described in **Chapter** 3 (*Imaging System*). Briefly, it consists of a modified ophthalmology slit lamp equipped with a 50 mm focal length imaging lens (numerical aperture 0.18; Thorlabs, Newton, NJ) and a high-frame-rate camera (Allied Vision, Edmund Optics, Barrington, NJ) operating at 510 FPS. The camera is positioned laterally to the participant’s eye to capture the corneal profile during blinking, acquiring 8-bit grayscale images at a spatial resolution of 800×600 pixels. A visible LED ring light, coaxially aligned with the camera lens, ensures uniform illumination and an optimal dynamic range [0–255] of grayscale values [127]. An example of the lateral eye image is reported in **Fig. 39b** in

4.2.2 EXPERIMENTAL PROTOCOL

We included healthy volunteers aged 18-50 with no history of ocular or systemic conditions that could influence IOP. All participants provided written informed consent. The study was conducted in compliance with the Declaration of Helsinki and approved by the Institutional Review Board of the University of Maryland, Baltimore. Each participant was assessed under two experimental conditions to examine corneal dynamics during a natural, complete blink (baseline) and during a Valsalva maneuver. For each participant, data were acquired only from the left eye.

The experimental protocol consisted of four steps. First, baseline IOP was measured using a portable tonometer (iCare IC200, Icare USA, Inc., Raleigh, NC, USA) [128], an FDA-approved medical device comparable to the Goldmann Applanation Tonometer (GAT)[129], [130].

Next, participants were asked to blink naturally while their eye movements were recorded using the high-speed imaging system. To ensure consistency in imaging geometry, each participant positioned their head on a modified chin rest, which prevented head tilt and maintained a constant imaging angle relative to the camera. Then, participants were instructed to perform the Valsalva maneuver, which is known to raise IOP [36], [131], [38]. This technique required them to exhale forcefully against a closed glottis into an air tube connected to an analog manometer, maintaining a pressure of at least 40 mmHg for 15 seconds [39]. The elevation of IOP during the Valsalva maneuver was confirmed with the portable tonometer. The maneuver was successful only if the IOP increased by more than 1 mmHg. If participants failed to maintain the required pressure or the IOP increase did not meet this threshold, they were asked to repeat the experiment. Finally, additional blinks and associated corneal dynamics were recorded while participants performed the Valsalva maneuver. Participants were excluded if their eyelashes obstructed the corneal profile, preventing measurement of corneal dynamics.

4.3 METHODS

A software program (StreamPix, NorPix Inc., Montreal, CA) was used to record blinks under two conditions: baseline and Valsalva. For the baseline condition, single or multiple videos totaling one minute in duration were recorded, during which participants were asked to perform natural blinks. For the Valsalva condition, multiple videos were recorded as each maneuver lasted approximately 15 seconds. A minimum of five blinks was considered acceptable for each condition.

Using a built-in MATLAB application (Video Viewer; MathWorks Inc., Natick, MA, USA), the blinks in the recorded videos were manually identified, determining the start and end frames of the eye-opening phase, from a fully closed eye to a fully open eye. During this manual eye blinking detection process, certain blinks were discarded based on the following criteria: (i) multiple blinks, when two or more consecutive blinks occur in rapid succession, making it difficult to isolate a single eye-opening phase. These were identified by the absence of a stable, fully open eye state between two consecutive closures. (ii) incomplete blinks, when the eye does not fully close before reopening, and (iii) excessive facial muscle activation, when significant movement of the eyebrows, forehead, or cheeks was observed, suggesting facial contractions that could interfere with the natural corneal response. Only natural and complete blinks were further analyzed.

A custom Python script was used to train a neural network specifically designed to predict eye masks during the eye-opening phase of each blink. The predicted ocular masks were subsequently assessed for the dynamics of the corneal profile during each blink. An exponential-like curve was produced for all the blinks by evaluating the longitudinal corneal displacement over time. The following parameters were computed: (i) the time constant, which quantifies the velocity at which the cornea rebounds during a natural, complete blink, and (ii) the displacement amplitude, which represents the extent of translation of the corneal profile (**Fig. 54**).

A pre-trained, participant-specific U-Net neural network (as described in **Chapter 3**) was employed solely to accelerate the manual labeling process. For each participant, at least two frames (one from baseline and one from elevated IOP) were manually segmented, producing ~400 labeled images per subject. These were used to train the network individually per participant, ensuring optimal adaptation to the specific eye morphology.

The U-Net architecture consisted of convolutional layers with filter sizes ranging from 64 to 512, a 1024-filter bottleneck, and batch normalization after each convolution. Input images were resized to [256, 256] and normalized to [0, 1]. Frames were categorized into four classes according to the mask area: closed (0%), semi-closed (0–40%), semi-open (40–80%), and open (>80%). Class imbalance was addressed via random resampling to match the size of the majority class, followed by data augmentation (horizontal flip, ±10° rotation, ±10% zoom, and ±10% translation). The dataset was split 80/20 for training/validation. Training employed the Adam optimizer (initial learning rate 1×10^{-3}, batch size 16, max 200 epochs) with early stopping and learning-rate reduction on plateau.

The loss function was a combo loss (α=0.5) combining BCE and Dice Loss, leveraging BCE's pixel-wise penalization and Dice's robustness to input imbalance. IoU was used for evaluation, achieving >90% IoU per participant on the validation set. The trained network then predicted masks for all other blinks of the same participant, significantly reducing manual annotation time.

After predicting ocular masks using the trained network, the corneal profile for each frame was extracted using the pipeline described in **Chapter 3**.

Then, the longitudinal displacement of the corneal profile during a blink was measured by examining its centroid during the eye-opening phase. The displacement of the centroid follows an exponential trajectory, reaching a plateau when the eye is fully open. Therefore, we modeled raw data using an exponential fitting function, as already stated in **Chapter 3**:

$$y(t) = A\left(1 - e^{\frac{-t}{\tau}}\right) + B$$

where A represents the displacement amplitude, which reveals the extent of movement of the corneal profile; B is the offset and τ is the time constant, which quantifies the rebound velocity of the corneal profile during the eye-opening phase of the blink after being deformed by the force applied by the eyelids.

Since the imaging angle was fixed by the modified chin rest during acquisition, variations among participants were limited to small differences in the relative position of the eye within the camera's field of view (e.g., slightly higher or lower, or shifted left or right eye position). Such variations affect only the offset parameter (B) of the exponential fitting, which corresponds to the initial position of the corneal profile centroid, but likely do not influence the dynamic parameters (τ and A) that describe the corneal dynamics.

Before applying exponential fitting, potential outliers in the centroid displacement data were removed. Specifically, the first five frames of each blink's opening phase were excluded, as these frames often present challenges for the neural network in accurately predicting the eye's mask due to partial obstruction of the corneal profile by eyelashes.

A filtering step was applied to the fitted curves based on their fitted parameters as the root mean square error (RMSE) and R^2. Specifically, R^2 values below $\mu_{R^2} - 3\sigma_{R^2}$ and RMSE values exceeding $\mu_{RMSE} + 3\sigma_{RMSE}$ were considered outliers. This filtering process allows us to exclude blinks with poorly fitted curves, resulting from segmentation errors, non-natural blinks, or head movements during the blink acquisition process.

Additionally, a second filtering process was applied to the curves to obtain the most accurate estimate of τ for each condition and participant. Specifically, only curves with a z-score within 1 were included for the baseline and Valsalva IOP conditions. This approach was validated by confirming that this metric satisfied the Kolmogorov-Smirnov test for normality, ensuring the distribution aligned with the assumptions required for this statistical filtering method, as described in **Chapter 3** (see **Fig. 58**). Finally, the average τ and amplitude were calculated for the remaining baseline and Valsalva IOP trajectories after this filtering process.

4.4 RESULTS

Fifteen healthy participants (28.3±6.02 years; 10 males, 5 females) were enrolled in the study and included in the final analysis. Each participant successfully performed the Valsalva maneuver, which was well tolerated without any adverse events during or after the procedure.

Under elevated IOP conditions, induced by the Valsalva maneuver, we hypothesize that the cornea rebounds faster due to the higher internal pressure exerting an increased restoring force. Consequently, a lower τ is expected for the Valsalva condition, reflecting faster corneal dynamics than the baseline IOP condition.

4.4.1 SINGLE SAMPLE ANALYSIS

Initially, nine blinks were recorded under baseline IOP conditions and ten under elevated IOP (Valsalva) conditions. After applying the filtering process, six blinks from each condition were selected for further analysis. Fig. **61.** Corneal dynamics for a single participant in baseline and elevated IOP conditions. (a) Normalized longitudinal centroid displacement during the blinks' opening phase. The blue curves represent the displacement under baseline IOP condition, whereas the red curves correspond to the displacement under elevated IOP condition (Valsalva). Normalization was applied only for visualization, as eye positions may vary across blinks recorded in different videos. (b) A of baseline versus elevated IOP conditions. (c) τ of baseline versus elevated IOP conditions.

a shows the corneal centroid displacement along the x-axis during the blink's opening phase for a single participant. In both conditions, the trajectory of the corneal centroid exhibits an exponential trend, stabilizing as the eye reaches its fully open state.

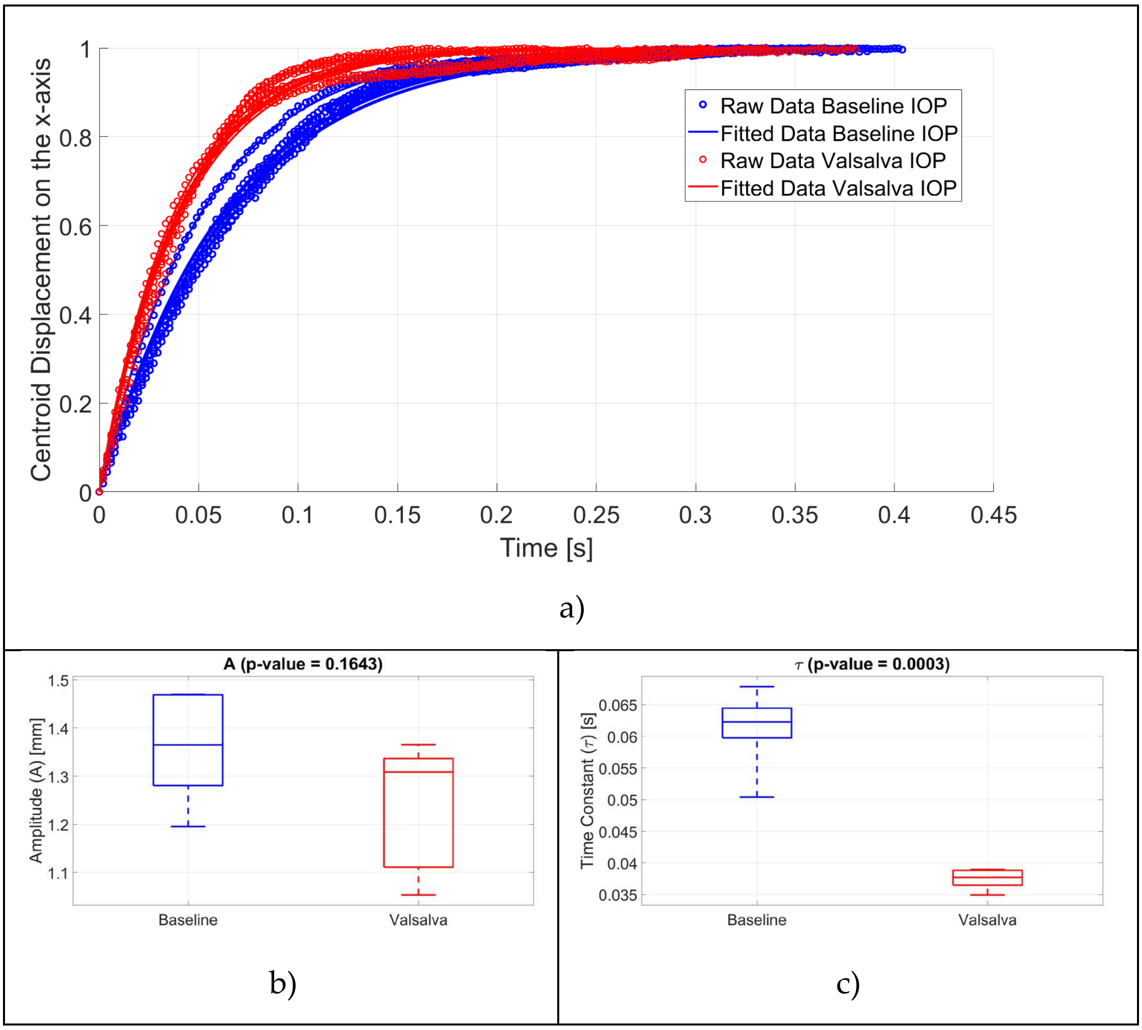

a)

b)

c)

Fig. 61. Corneal dynamics for a single participant in baseline and elevated IOP conditions. (a) Normalized longitudinal centroid displacement during the blinks' opening phase. The blue curves represent the displacement under baseline IOP condition, whereas the red curves correspond to the displacement under elevated IOP condition (Valsalva). Normalization was applied only for visualization, as eye positions may vary across blinks recorded in different videos. (b) A of baseline versus elevated IOP conditions. (c) τ of baseline versus elevated IOP conditions.

We measured τ and A of the cornea during the blink's opening phase for both conditions. The results showed that τ was lower in the Valsalva condition (37.44 $\pm$ 0.64 ms) compared to the baseline (61.17 $\pm$ 2.44 ms), and this difference was statistically significant ($t = 9.42, P < 0.001$, Fig. **61.** Corneal dynamics for a single participant in baseline and elevated IOP conditions. (a) Normalized longitudinal centroid displacement during the blinks' opening phase. The blue curves represent the displacement under baseline IOP condition, whereas the red curves correspond to the displacement under elevated IOP condition (Valsalva). Normalization was applied only for visualization, as eye positions may vary across blinks recorded in different videos. (b) A of baseline versus elevated IOP conditions. (c) τ of baseline versus elevated IOP conditions.

c).

Regarding A, the average for the baseline IOP condition was 1.36 $\pm$ 0.04 mm, and for the Valsalva condition, it was 1.25 $\pm$ 0.05 mm, and this difference was not statistically significant (**Fig. 61b**).

4.4.2 STATISTICAL ANALYSIS

To assess the effectiveness of the Valsalva maneuver in increasing IOP, we compared IOP values measured before and after the maneuver across all participants using the portable tonometer. The mean baseline IOP was 18.55 $\pm$ 0.72 $mmHg$, while the mean IOP during the Valsalva condition increased to 23.73 $\pm$ 1.01 $mmHg$. This increase was statistically significant ($t = 6.78$, $P <$

0.001), confirming that the Valsalva maneuver induced a consistent and measurable elevation in IOP, with IOP difference ranging from 1.7 $mmHg$ to 13 $mmHg$ between the two conditions.

To determine whether the IOP-dependent behavior observed in a single subject was consistent among participants, we performed a statistical analysis on all enrolled samples.

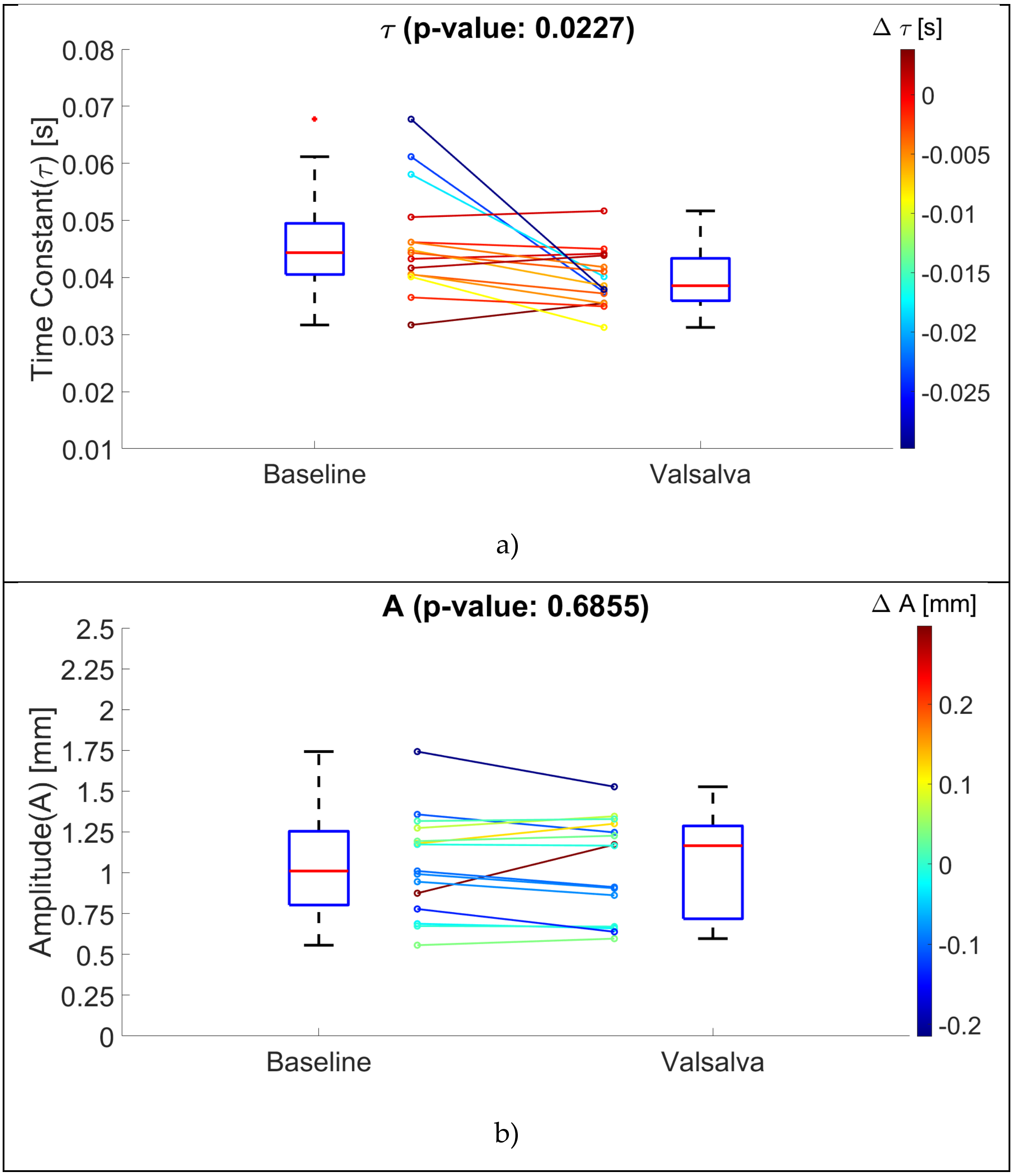

a)

b)

Fig. 62. Statistical analysis for 15 healthy samples without ocular disease history. (a) τ of normal and Valsalva IOP conditions across 15 samples ($P < 0.05$). (b) A of normal and Valsalva IOP conditions across 15 samples (no statistically significant difference).

Fig. 62. Statistical analysis for 15 healthy samples without ocular disease history. (a) τ of normal and Valsalva IOP conditions across 15 samples (P < 0.05). (b) A of normal and Valsalva IOP conditions across 15 samples (no statistically significant difference).

a illustrates the variation of τ for each participant who underwent the experiment. Out of 15 samples, 11 exhibit the expected trend, showing a lower τ under the elevated IOP condition compared to the baseline IOP condition.

The average τ was $46.23 \pm 2.48\,ms$ for the baseline IOP condition and $39.73 \pm 1.31\,ms$ for the elevated IOP condition ($t = -2.56$, $P < 0.05$, **Fig. 62.** Statistical analysis for 15 healthy samples without ocular disease history. (a) τ of normal and Valsalva IOP conditions across 15 samples (P < 0.05). (b) A of normal and Valsalva IOP conditions across 15 samples (no statistically significant difference). **b**), which indicates a faster corneal rebound when the Valsalva maneuver is performed. **Fig. 62b** depicts the changes in A for each participant across the two IOP conditions, with the color scale indicating the change in the amplitude ΔA between baseline and elevated IOP conditions. The average amplitude was $1.05 \pm 0.08\,mm$ for the baseline IOP and $1.04 \pm 0.08\,mm$ for the elevated IOP condition. Unlike τ, A does not exhibit a clear or consistent pattern across participants, with changes appearing more variable and without a statistically significant difference.

Furthermore, to confirm the results obtained from the paired t-test, the Wilcoxon signed-rank test was applied, as it is more robust to outliers, does not assume normality of the data and is suitable for a small sample size. The test confirmed the statistical difference observed for τ ($P = 0.0125$), supporting the evidence of a faster corneal rebound under elevated IOP conditions. Conversely, the comparison of A between baseline and Valsalva conditions remained not statistically significant ($P = 0.495$), consistent with the paired t-test results.

In addition, we investigated whether the blink-derived biomechanical parameters were associated with baseline IOP. Spearman's rank correlation coefficients were computed between baseline IOP and the parameters τ and A. No significant correlation was found between τ and baseline IOP ($\rho = -0.25$, $P = 0.38$) or between A and baseline IOP ($\rho = -0.17$, $P = 0.54$). Although these associations were not statistically significant, both parameters exhibited a weak negative trend, also demonstrating a tendency toward faster corneal rebound (lower τ) at higher IOP levels.

4.5 DISCUSSION

The deformation of the cornea by the eyelid during a blink [33], [132], [133], [134] provides an opportunity to assess IOP-dependence of this phenomenon. However, the corneal deformation depends on its topography and biomechanics, leading to observable changes in corneal dynamics [135], [136], [137], [138]. As a result, various structural and pathological conditions may be potential modifiers of the observed corneal response. For instance, keratoconus leads to localized thinning and steepening of the cornea, altering its curvature and mechanical stiffness [139], which can modify the corneal response to ELP. Moreover, post-surgical eyes typically exhibit a lower corneal hysteresis, which reflects the viscoelastic damping response of the corneal tissue to the applied force and corneal resistance factor, which is related to the time-independent corneal response to the applied force [140]. These biomechanical changes can result in a slower rebound of the corneal profile and an altered displacement amplitude induced by ELP.

Lin et al.[108] further confirmed that ELP causes a flattening effect on the cornea, with biomechanical IOP correlating with eyelid pressure and corneal deformation during a blink. Our results demonstrate that the velocity of the corneal rebound is sensitive to IOP changes: the observed decrease of τ under elevated IOP conditions suggests that the cornea rebounds more rapidly after eyelid-induced deformation. We hypothesize that this is due to the increased internal pressure exerting a greater restoring force, leading to faster recovery of the corneal profile. On the other hand, A did not significantly differ between conditions, indicating that the extent of corneal deformation is consistent across the two conditions. The absence of a statistically significant difference in the amplitude suggests that the faster rebound of the corneal profile under Valsalva conditions cannot be attributed to an increase in the magnitude of eye movement. Indeed, elevated IOP predominantly influences the corneal rebound velocity without affecting the displacement amplitude.

The current prototype does not provide absolute IOP values. Instead, it extracts two biomechanical parameters, τ and A, that are sensitive to IOP variations. These parameters reflect the viscoelastic behavior of the cornea under physiological eyelid pressure and should be interpreted as IOP-dependent biomechanical indicators rather than direct tonometric measurements. This interpretation is supported by the analysis of the relationship between these parameters and the absolute IOP values: when assessing the correlation between baseline IOP and τ or A across participants, no statistically significant relationship was found for either parameter.

Compared to conventional tonometry or recent innovations (e.g. contact lenses, implantable sensors), which require contact with the eye or surgical implants and can only be performed during office visits with professional assistance, our technology, once miniaturized into a wearable device, can potentially provide continuous non-contact monitoring of IOP-dependent indicators without requiring significant patient expertise. A more accessible, user-friendly and frequent monitoring solution like this can lead to a better understanding of IOP patterns and their relationship to glaucoma progression. For instance, a study of IOP monitoring conducted outside of regular office hours found that peak 24-

hour IOP was greater than the peak IOP observed during prior office visits in 62% of the patients. Notably, the results of 24-hour IOP monitoring led to an immediate treatment change in 36% of patients[141]. Therefore, this technology could facilitate the early detection of abnormal IOP fluctuations, enable more precise patient-based treatment strategies, and mitigate the impact of untreated glaucoma.

Several types of glaucoma exist, the most common being primary open-angle glaucoma which is characterized by elevated IOP values beyond the normal range and progressive optic nerve damage [142]. However, not all forms of glaucoma are associated with increased IOP [143]. In normal-tension glaucoma, IOP values remain within the clinically normal range, yet progressive optic nerve damage can still occur [144]. In such cases, analyzing IOP fluctuations throughout the day could be beneficial for the early detection of the disease [145], as patients with normal-tension glaucoma often exhibit greater diurnal IOP variability [146], [147], even if additional IOP-independent factors have gained increasing relevance in detecting this ocular disease [148]. The proposed method can potentially assess these variations through frequent, non-invasive, home-based measurements. Conversely, ocular hypertension is characterized by IOP levels above the normal threshold despite the absence of optic nerve damage [149]. For these patients, the absolute IOP value remains the primary diagnostic metric.

To extend the proposed approach from indirectly detecting IOP variations to providing quantitative IOP values, a calibration phase would be required. This phase would involve acquiring data from a cohort of patients showing controlled IOP changes and correlating the variations in biomechanical parameters with the corresponding changes in IOP measured by standard tonometry. Once this relationship is established, a single reference tonometric measurement combined with subsequent blink-based biomechanical measurements would allow estimating absolute IOP values over time.

Our approach has limitations. First, the variability of IOP elevation induced by the Valsalva maneuver presents challenges in achieving consistent IOP increments across trials. Additionally, IOP measurements during the Valsalva maneuver are taken before the acquisition of natural blinks, as it is not feasible to measure IOP using a portable tonometer and simultaneously record natural blinks during the application of the maneuver. This sequential process may introduce variability in the exact elevated IOP level during blink acquisition.

Furthermore, while our analysis focused on longitudinal corneal displacement, it is known that the eye can retract during blinking [150], [151], [152], [153] due to ELP and subsequently move forward upon eyelid release, contributing to the observed dynamics. Iskander et al.[154] have proposed three different models depicted in Fig. **63.** Three models for the longitudinal corneal profile displacement during a blink. (a) Eye movement: the whole eye globe (black) moves forward to a new position (red dashed line), as indicated by the vertical arrow; (b) Cornea deformation: the red dashed profile represents the cornea deformed by eyelid pressure, with blue horizontal arrows indicating lateral compression and the blue vertical arrow showing the flattening direction; (c) Combined effect of eye movement (black arrow) and corneal deformation (blue arrows).

Their results have shown that the longitudinal movement of the corneal profile during a blink is the superposition of eye movement and corneal deformation. Indeed, the inability to separate these effects in our current framework is another limitation. However, our results suggest that the Valsalva maneuver does not necessarily lead to greater globe movement. If it were true that this maneuver causes greater forward movement of the eye during the opening phase of a blink, one would expect A to consistently be higher than in the baseline IOP condition, with a statistically significant difference. The fact that a statistically significant difference is observed only for τ suggests that the Valsalva maneuver primarily results in a different response speed of the corneal rebound, which could be related to the IOP.

In addition to eye retraction, several studies have demonstrated that the globe undergoes small rotational movements during the blinking process, primarily during the lid closure phase, which contributes to the stabilization of visual perception [155]. Specifically, blinks are accompanied by downward and nasal rotations that precede lid closure, followed by an intorsional, upward return during reopening [151], [156]. Kirchner et al.[157] further confirmed that these rotations typically range between 1–4° during natural blinks and represent a much smaller, subject-dependent component superimposed on the main translational motion of the globe. Therefore, since the analysis in the present study focused on the eye-opening phase, any residual rotation occurring during eyelid reopening is expected to be minimal and unlikely to significantly affect the longitudinal corneal dynamics quantified in our measurements.

Finally, another concern is the potential influence of physiological changes unrelated to IOP during the Valsalva maneuver. While it is well-documented that the maneuver induces an increase in IOP, the exact mechanisms behind this increase remain unclear [158]. Therefore, the observed differences between the baseline IOP condition and the Valsalva condition may not be attributed only to an IOP increase but could also be influenced by other phenomena induced by the Valsalva maneuver, such as changes in ocular blood flow [39], venous pressure [159], or biomechanical properties of the anterior segment [160].

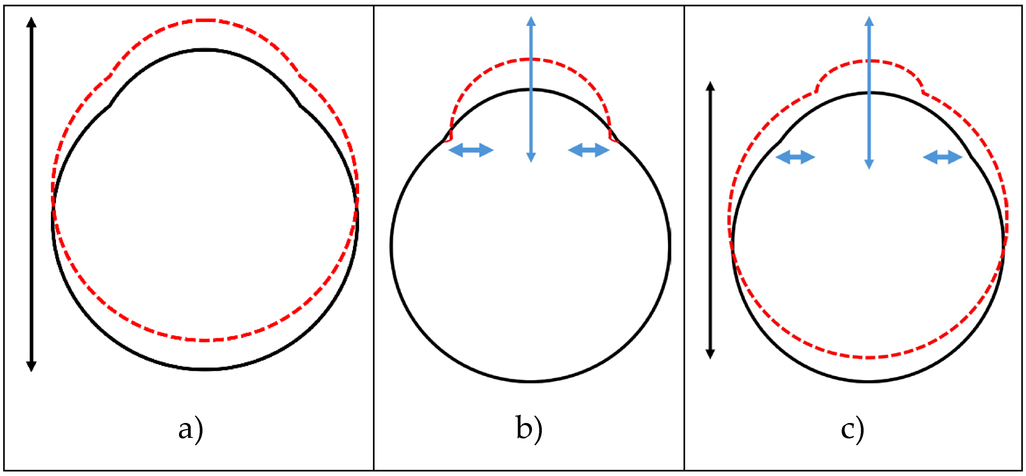

Fig. 63. Three models for the longitudinal corneal profile displacement during a blink. (a) Eye movement: the whole eye globe (black) moves forward to a new position (red dashed line), as indicated by the vertical arrow; (b) Cornea deformation: the red dashed profile represents the cornea deformed by eyelid pressure, with blue horizontal arrows indicating lateral compression and the blue vertical arrow showing the flattening direction; (c) Combined effect of eye movement (black arrow) and corneal deformation (blue arrows).

4.6 CONCLUSION

In this chapter, we presented a novel imaging system that provides information on the corneal dynamics during a natural, complete blink and its correlation with IOP changes. Thus, the corneal dynamics were analyzed under two conditions: baseline IOP and elevated IOP, obtained during the Valsalva maneuver. The proposed approach demonstrates the potential to extract blink-induced corneal rebound metrics that are sensitive to IOP changes, offering a promising foundation for future non-invasive and continuous IOP monitoring solutions. Future research should address key limitations. Specifically, separating the effects of corneal deformation and globe movement during blinking would provide a clearer understanding of the corneal dynamics. Moreover, a clinical study involving patients with glaucoma, both before and after administration of IOP-lowering medication, could validate the proposed method against applanation tonometry. This approach will overcome the limitations of the Valsalva maneuver and provide deeper insight into the relationship between corneal dynamics and IOP. Furthermore, this clinical trial would integrate complementary ophthalmic measurements obtained from devices such as the Corvis ST and the Ocular Response Analyzer to provide a more complete characterization of the biomechanical properties of the cornea and to assess whether these parameters influence the IOP-dependent metrics derived from the blink-related corneal dynamics. Additionally, system illumination should be optimized to properly work under ambient lighting conditions typically found in a real-world scenario.

In conclusion, we have presented a novel, non-contact imaging system capable of tracking the corneal profile during a natural, complete blink and analyzing its dynamics as an indicator of IOP variations. The proposed method does not directly measure IOP in mmHg but demonstrates the feasibility of blink-related corneal dynamics parameters as indirect markers of IOP changes. After appropriate miniaturization and calibration correlating these parameters with reference tonometric values, this approach may enable continuous, home-based assessment of IOP-dependent corneal dynamics, offering a realistic and accessible complementary tool for glaucoma management and early detection.

CHAPTER 5

AUTOMATIC ECG WAVE SEGMENTATION[6]

INTRODUCTION

CVDs affect a large portion of the population, particularly in developing countries, and represent a major cause of morbidity and mortality worldwide. CVD encompasses a wide range of conditions involving the heart and blood vessels. Among them, atherosclerosis can lead to severe complications such as myocardial infarction and stroke, as well as arrhythmias and impaired valve function [162]. Early detection of CVD is therefore crucial.

ECG is one of the most effective tools for predicting and diagnosing CVDs. It is the primary method for recording the heart's electrical activity and is widely used to detect cardiac pathologies by analyzing key segments of the cardiac cycle. This technique is non-invasive, cost-effective, safe, and accessible. The growing availability of wearable [163], [164], and wireless devices [165], which can be applied in telemedicine [166], [167] and home-based patient monitoring, has further enhanced its potential. These systems enable continuous measurement of vital signs and related parameters such as heart rate (HR) [168], [169], oxygen saturation (SpO_2), and respiratory rate (RR), among others.

---

[6] This chapter is based on the paper [161].

CHAPTER 5

Beyond its clinical relevance in cardiology, the ECG signal is increasingly studied in relation to ocular physiology and IOP. Several studies have demonstrated that systemic blood pressure and cardiac activity influence IOP fluctuations and ocular perfusion [170], [171], [172]. Moreover, autonomic nervous system regulation, reflected in HRV derived from ECG, has been associated with altered autonomic balance in patients with NTG compared to those with HTG, indicating a stronger sympathetic response to stress stimuli [173].

This cardio-ocular interaction suggests that cardiac electrical activity may provide additional insight into the systemic mechanisms underlying corneal dynamics and IOP variations. In the previous chapters, the blink-induced corneal deformation was analyzed and modeled to extract biomechanical parameters—such as deformation amplitude and recovery time constant—whose variation was shown to depend on IOP. Therefore, integrating ECG analysis into this framework enables multi-parametric interpretation, in which cardiovascular signals complement ocular measurements to better understand how systemic circulatory and autonomic factors may contribute to the blink-induced mechanical response of the cornea and to IOP fluctuations.

An ECG records the heart's electrical activity over time, generated by the action potentials propagating through the cardiac conduction system during each heartbeat. Electrodes placed on the skin detect these impulses thanks to the conductive properties of the body's interstitial fluids, allowing the potential difference to be measured. The resulting signal, expressed in millivolts as a function of time, displays characteristic peaks—P, Q, R, S, and T—representing the depolarization and repolarization phases of the atria and ventricles (**Fig. 64**).

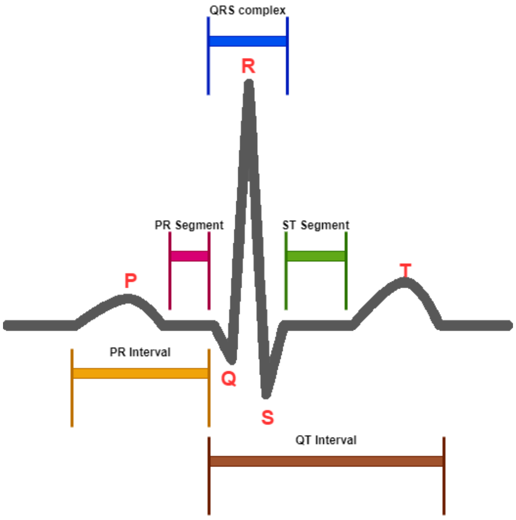

Fig. 64. ECG signal morphology of a cardiac cycle.

The QRS complex corresponds to ventricular depolarization, while the P wave reflects atrial depolarization. The PR segment marks the conduction of the impulse to the ventricles and the onset of atrial diastole. The T wave corresponds to ventricular diastole [174], [175]. Clinical diagnosis relies on analyzing both the morphology and duration of these components. Accurate ECG segmentation is thus essential for assisting clinicians in diagnosing and monitoring cardiac conditions.

Recent literature has proposed various approaches to improve ECG wave segmentation. Automatic segmentation remains challenging due to the considerable variability in QRS morphology between individuals, the lower amplitude of the P wave, and the diverse shapes of the T wave depending on myocardial condition. Furthermore, there is no universal agreement on the precise location of the characteristic points.

The most effective techniques include the Pan–Tompkins algorithm [176], STFT [177], WT [178], [179], EMD with Hilbert spectral analysis for nonstationary signals [180], [181], [182], [183], and other approaches described in [184]. Many methods involve transforming or filtering the ECG signal to emphasize significant features and locate points of interest. Alternative strategies rely on machine learning and deep learning models such as CNNs, SVMs, and other AI-based frameworks [185], [186], [187], [188], [189].

While many algorithms can accurately segment the QRS complex, the detection of P and T waves remains less reliable. Most existing solutions identify peaks but fail to determine the exact onset and offset of each wave, information that is highly valuable for diagnostic purposes.

In this chapter, we present a new ECG segmentation method that does not rely on artificial intelligence. The approach combines WT with a custom-designed algorithm capable of detecting not only the QRS complex but also the complete P and T waves, including their start and end points. The method is implemented in a system composed of a DAQ device managed by a LabVIEW Virtual Instrument and a SparkFun single-lead heart rate monitor based on the Analog Devices AD8232 amplifier. The DAQ acquires the ECG signal and performs pre-processing, while wave segmentation and result analysis are carried out in MATLAB R2022b.

5.1 ACQUISITION SYSTEM

The raw ECG signal, before amplification, exhibits a relatively low amplitude, on the order of millivolts, and is often affected by artifacts and noise. Common sources of interference include the 50 Hz mains frequency, baseline drift, and the electrical activity of other muscles (electromyographic noise), all of which can compromise signal quality. To obtain a diagnostically useful signal, amplification and filtering stages are typically required.

In this study, ECG acquisition was performed using the AD8232 single-lead heart rate monitor, a compact and integrated signal conditioning module designed for ECG and other biopotential measurements. This device requires only three electrodes and produces an output in which the characteristic P, QRS, and T waves of a single cardiac cycle can be clearly distinguished. The AD8232 combines amplification, filtering, and noise suppression in a single module, enabling reliable extraction of small biopotential signals even in the presence of motion artifacts or when electrodes are not optimally positioned.

The AD8232 board, shown in **Fig. 65**, features nine pins for integration with an analog acquisition system: SDN, LO+, LO-, OUTPUT, 3.3 V, and GND. In addition, three dedicated pins—RA (right arm), LA (left arm), and RL (right leg)—connect to the electrodes. The raw ECG signal is obtained by subtracting the potential recorded at RA from that at LA, with RL serving as the reference electrode. While this raw signal can be accessed directly from the RA, LA, and RL pins, it is weak in amplitude and contains significant noise, making it difficult to interpret without further conditioning.

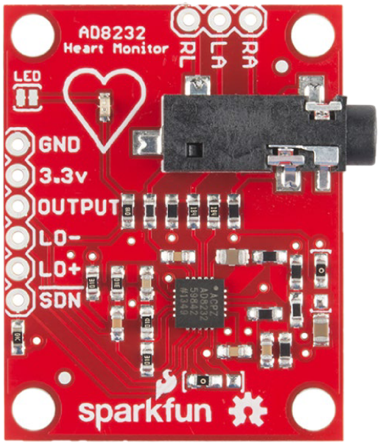

Fig. 65. AD8232 single lead heart rate monitor in a break-out board developed by Sparkfun.

To minimize noise in the HR monitor output, correct electrode placement is essential. In this work, electrodes were positioned according to the Einthoven triangle configuration, as illustrated in **Fig. 66**, where the black pad corresponds to the right arm (RA), the blue pad to the left arm (LA), and the red pad to the right leg (RL).

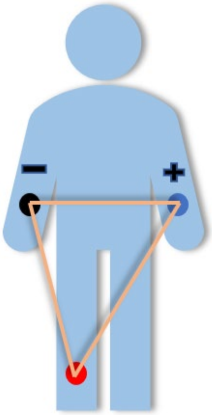

Fig. 66. Positioning of electrodes based on Einthoven triangle (black pad corresponds to the right arm, blue pad corresponds to the left arm and the red one to the right leg).

For data acquisition, the AD8232 output was connected to a National Instruments USB-6212 DAQ board, a 16-bit device capable of sampling at up to 400 kHz. Power to the AD8232 was supplied by a bench power supply. Signal acquisition and real-time visualization were managed via a LabVIEW Virtual Instrument, while subsequent processing and analysis were conducted in MATLAB. The complete experimental setup is shown in **Fig. 67**.

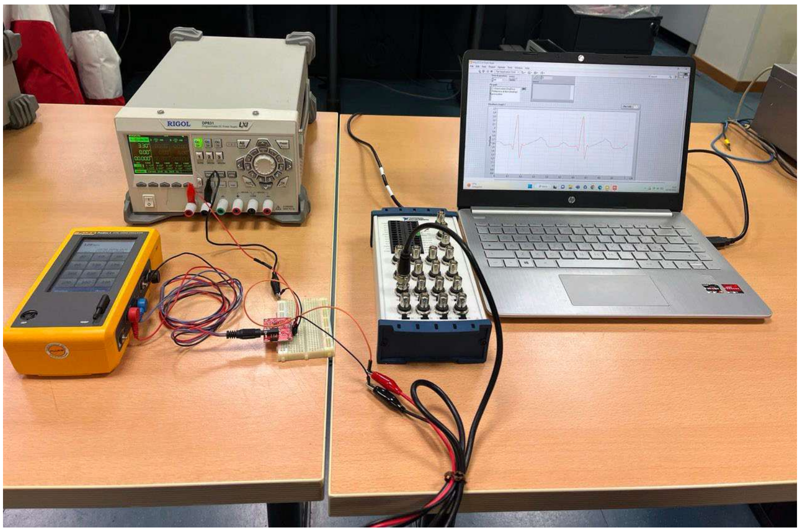

Fig. 67. Experimental setup for ECG acquisition.

5.2 ECG SEGMENTATION

ECG is a fast, non-invasive, and widely adopted diagnostic technique that provides a graphical representation of the heart's electrical activity. It is a fundamental tool for detecting cardiac dysfunctions, where accurate segmentation and feature extraction are critical steps for establishing a diagnosis. This section introduces a novel method for the segmentation of QRS complexes, T waves, and P waves in ECG waveforms, aimed at supporting the early detection of cardiovascular diseases.

Although numerous algorithms have been developed and successfully applied for QRS complex segmentation, reliable detection of P and T waves remains a challenging task. The proposed approach addresses this gap by first detecting R-peaks using a threshold derived from the Otsu method. Subsequently, it segments all remaining ECG waves through the combined use of wavelet filtering and a local maxima detection algorithm. For each waveform, both the onset and offset are precisely determined, enabling a complete temporal characterization of the cardiac cycle.

5.2.1 RAW SIGNAL ACQUISITION

The ECG signal was acquired using the DAQ device, with acquisition parameters configured via the front panel to fully exploit the ADC range. The sampling rate was set to 200 Hz, with the input voltage range spanning from −5 V to +5 V. Before performing parameter extraction and analysis, a pre-processing stage was implemented to remove baseline drift and attenuate the 50 Hz power line interference. For this purpose, LabVIEW was used to apply WT filtering, with parameters defined according to [190]. A threshold frequency of 0.35 and a db06 mother wavelet with symmetric extension were employed for the detrending process. Wavelet denoising was then carried out using an undecimated WT with the db06 wavelet and eight decomposition levels. The thresholding process used a single-level rescaling method, the universal threshold rule, and a soft thresholding approach.

Fig. 68 and **Fig. 69** show the ECG signal before and after filtering, respectively.

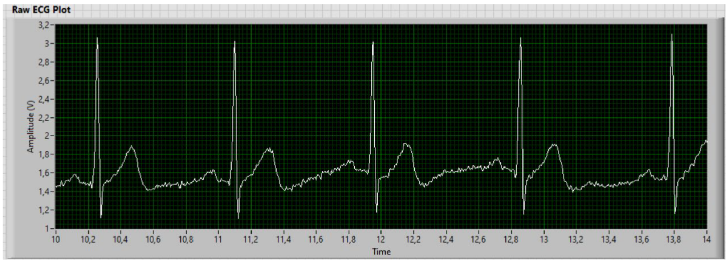

Fig. 68. Raw ECG signal.

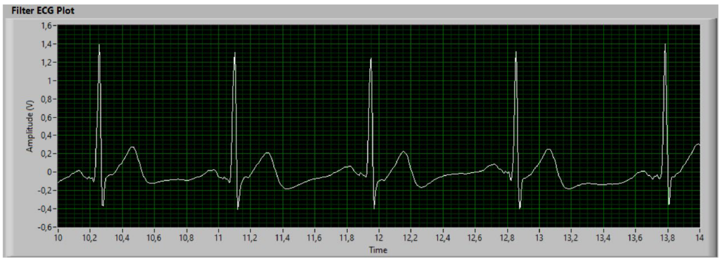

Fig. 69. Filtered ECG signal.

In addition to real ECG recordings, simulated ECG signals at different heart rates were also generated and analyzed using the Fluke ProSim 4 simulator.

5.2.2 R-PEAK DETECTION

The proposed algorithm is designed to identify both the position and amplitude of the R-peak in the unprocessed ECG signal, as well as to determine the onset and offset of the QRS complex. **Fig. 70** illustrates the initial step, in which the R-peak position and amplitude are detected directly from the raw ECG trace.

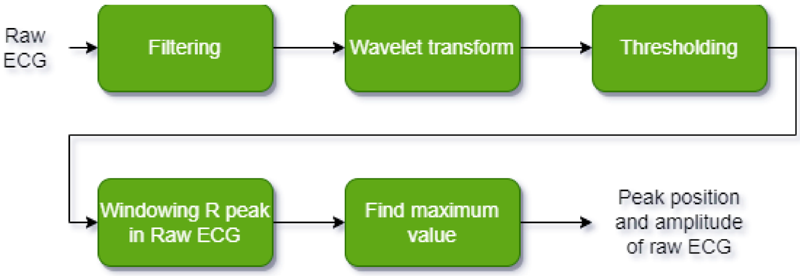

Fig. 70. R-peak detection algorithm.

Following the pre-processing stage, an undecimated WT is applied using the db02 mother wavelet, a multiple-level rescaling method with 10 decomposition levels, and a universal thresholding rule with soft thresholding. This operation attenuates the P and T waves within each cardiac cycle, isolating the QRS complex. The resulting signal after WT filtering is shown in **Fig. 71**.

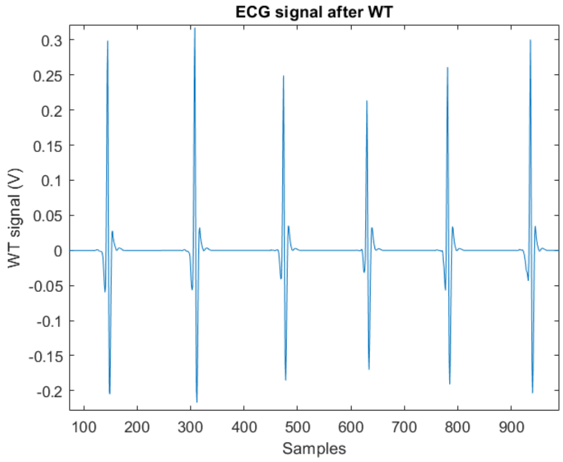

Fig. 71. ECG signal after WT filtering process.

Secondly, an image processing technique [191] has been employed to detect R-peaks using a threshold value derived from Otsu's method [192], a non-parametric and unsupervised approach to automatic threshold selection based on histogram analysis. Applying this threshold to the WT-filtered signal allows the identification of each R-peak within a defined temporal window, represented as a square signal in **Fig. 72**.

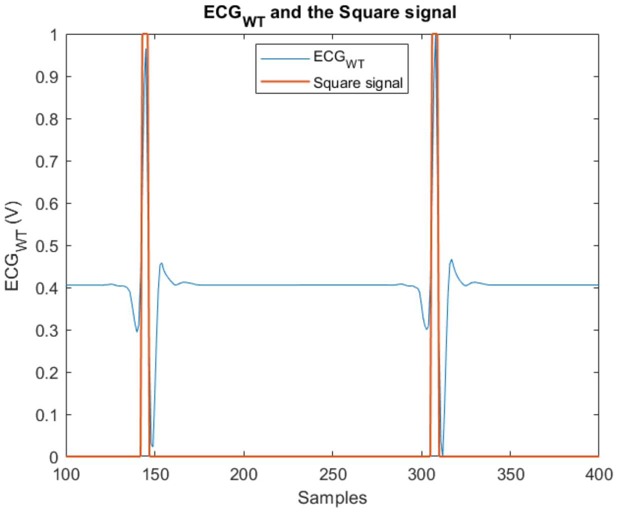

Fig. 72. ECG signal after WT transform (blue) and square signal (red), which defines the temporal window of the R-peak.

Once the candidate regions are identified, the algorithm searches the raw ECG signal within each window to locate the maximum amplitude, which corresponds to the R-peak as illustrated in **Fig. 73**.

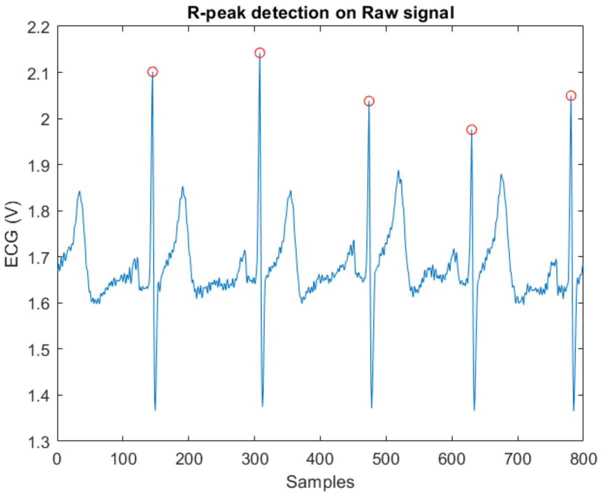

Fig. 73. R-peak detection on Raw ECG signal.

After the R-peaks are identified, the mean heart rate (HR) is computed by measuring the mean duration of R–R intervals, according to:

$$HR = \frac{mean(R-R)}{60}$$

5.2.3 QRS ONSET AND OFFSET DETECTION

To determine the onset and offset of the QRS complex, the STD of the wavelet-filtered signal is computed over a sliding window consisting of five samples, including the central sample. The window is defined by 5 samples preceding (ka) and 5 samples following (kb) the central point, plus the central sample itself. The length of this window is empirically chosen based on the sampling frequency of the acquired ECG signal. For a sampling frequency of 100 Hz, the optimal configuration is ka=1 and kb=1. The resulting STD signal is shown in **Fig. 74**.

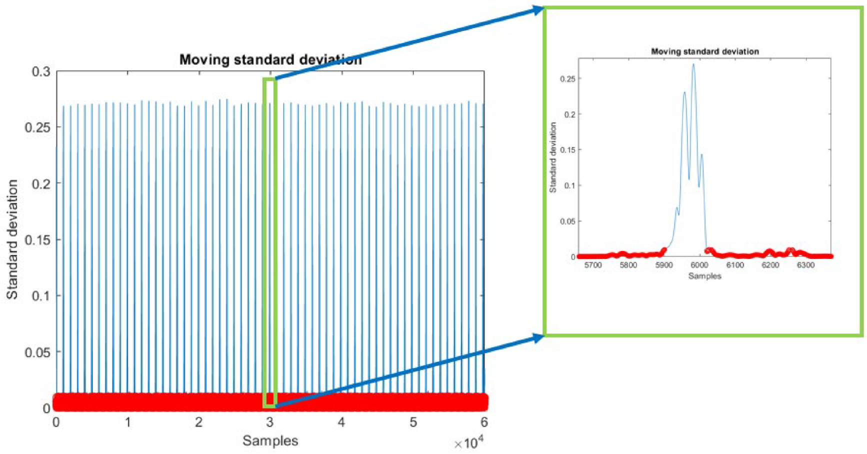

Fig. 74. STD of sliding window (blue) and zeros detected from zero-crossing algorithm.

A zero-crossing detection algorithm is then applied to the STD signal to identify the onset and offset of each QRS complex. The onset is defined as the last zero value in the STD signal occurring before the $i-th$ R-peak, while the offset corresponds to the first zero value after the $i-th$ R-peak.

Within the identified QRS segment, the Q wave is determined as the minimum amplitude between the onset and the R-peak, along with the time interval between these two points. Similarly, the S wave is identified as the minimum amplitude between the R-peak and the offset of the QRS complex.

An example of QRS segmentation using the proposed method is illustrated in **Fig. 75**.

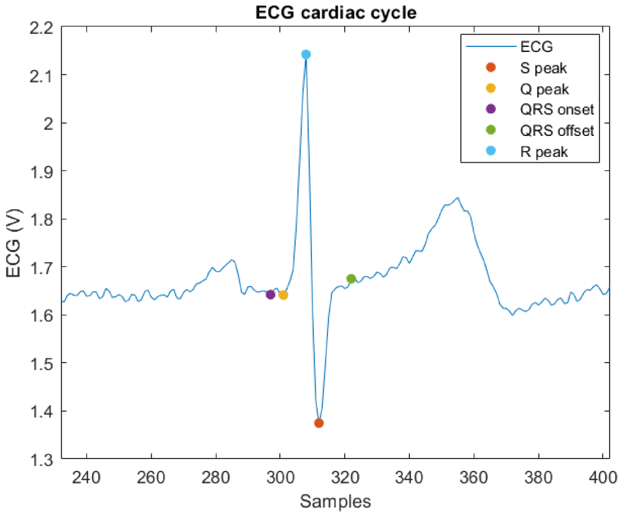

Fig. 75. QRS complex segmentation.

5.2.4 P WAVE SEGMENTATION

Detection of the P wave is particularly challenging due to its relatively small amplitude compared to the R-peak and the frequent presence of noise that can obscure its onset and offset. To address these challenges, the algorithm depicted in **Fig. 76** is proposed.

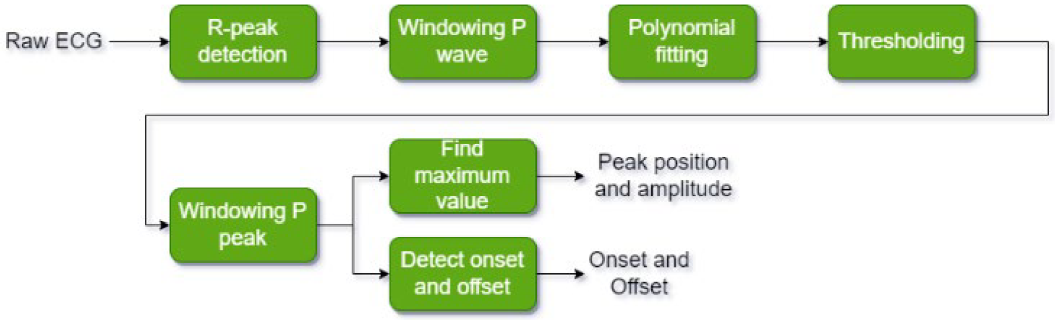

Fig. 76. P wave and T wave detection algorithm.

After R-peak detection, a windowing approach is applied to the ECG signal for each detected R-peak, excluding the first and last peaks to avoid incomplete cardiac cycles. For each cycle, the analysis window begins at the onset of the cardiac cycle and ends at the onset of the subsequent QRS complex, ensuring that the P wave is fully contained within this interval.

Within the selected segment, a fourth-degree polynomial fitting is applied to smooth the waveform. Otsu's method is then used to compute an adaptive threshold for isolating the P wave. The peak value within this window is identified as the P-peak, while the initial and final points of the window correspond to the onset and offset of the P wave, respectively, as shown in **Fig. 77**.

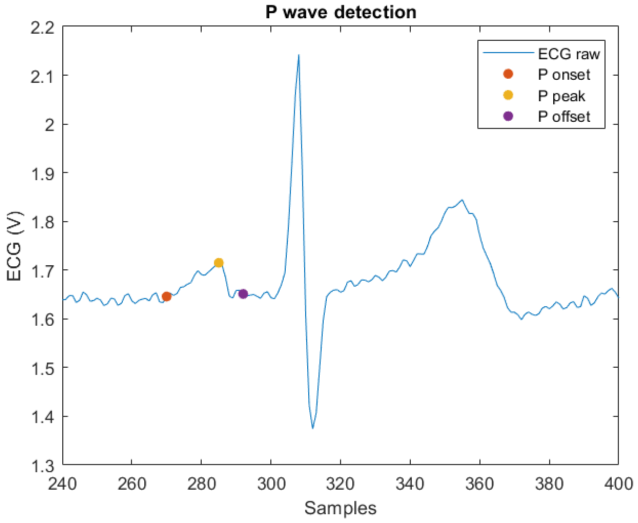

Fig. 77. P wave segmentation.

5.2.5 T WAVE SEGMENTATION

The detection of the T wave presents a significant challenge due to its smaller size in comparison to the R-peak, coupled with the presence of noise that obscures the boundaries. Furthermore, the lack of universal detection rules presents a challenge in the detection of both the T wave and the P wave. Consequently, researchers have concentrated their efforts on defining automatic detection algorithms.

More in depth, the same approach previously utilized for P-wave detection is employed for T-wave detection.

Indeed, a windowing technique has been applied to the ECG signal from the corresponding QRS offset to the end of the cardiac cycle for each R-peak. Subsequently, a fourth-degree polynomial fitting and Otsu's thresholding have been employed. The T-peak has been defined as the maximum value within this window, and the boundaries have been defined as the two edges. An example of T wave segmentation from a cardiac cycle can be depicted in **Fig. 78**.

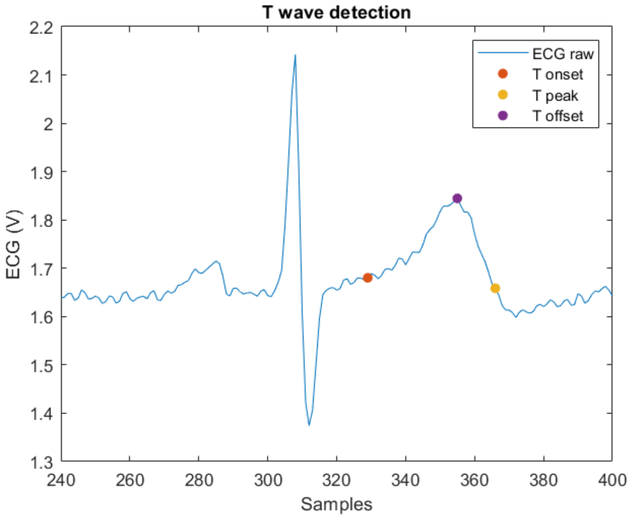

Fig. 78. T wave segmentation.

5.3 RESULTS

The proposed algorithm was evaluated on 100 cardiac cycles from three different patients, with ECG signals acquired using the single-lead heart rate monitoring system developed in this work. **Fig. 79** summarizes the percentage of correctly detected points of interest for the P wave, T wave, and QRS complex across all recorded data. As shown, the QRS complex was consistently detected, along with the P and T peaks. However, the accuracy in detecting the onset and offset of the P and T waves was comparatively lower.

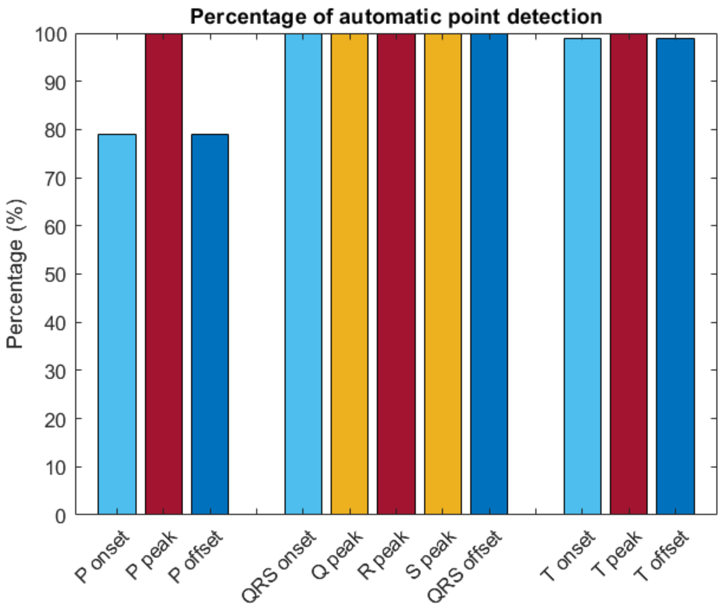

Fig. 79. Percentage of detection.

Table 12 reports the mean temporal error and STD for each annotated point within the ECG waveform. These values were computed as the time differences between the positions identified by the proposed algorithm and the corresponding handcrafted annotations.

	Mean (s)	**STD (s)**
P onset	-0.045	0.052
P peak	0.000	0.053
P offset	0.000	0.012
QRS onset	-0.010	0.012
Q peak	0.000	0.002
R peak	0.000	0.001
S peak	0.000	0.000
QRS offset	0.015	0.011
T onset	-0.002	0.014
T peak	0.005	0.001
T offset	-0.010	0.011

Table 12. Mean time error and standard deviation for each ECG wave, onsets, and offsets.

Furthermore, **Fig. 80** illustrates the IoU for the P wave, QRS complex, and T wave. The results indicate that the highest IoU was obtained for the T wave, while the lowest was observed for the P wave.

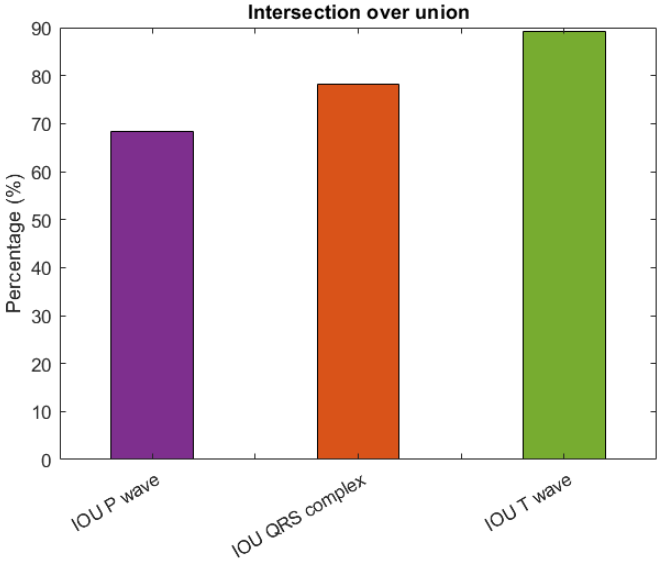

Fig. 80. IoU for all the ECG waves.

5.4 CONCLUSION

In this chapter, we presented a novel ECG segmentation approach that combines WT with Otsu's method, designed for application to ECG signals acquired from a single-lead heart rate monitor. The proposed algorithm demonstrated robust performance in detecting R-peaks, achieving a 100% detection rate and enabling accurate heart rate estimation. Furthermore, the QRS complex was consistently segmented across all recordings, including those affected by noise, with minimal temporal errors. Importantly, the method also addressed the more challenging task of detecting P and T waves, an area where segmentation accuracy remains a limitation in the existing literature, thus providing a comprehensive solution for complete P–QRS–T detection.

The proposed method for accurate segmentation of cardiac electrical activity not only advances ECG signal processing for telemedicine applications but also facilitates the investigation of how systemic circulatory and autonomic factors may contribute to the blink-induced mechanical response of the cornea and to IOP fluctuations.

CONCLUSION

In this thesis, novel measurement methods for intraocular pressure (IOP) assessment and blink detection have been developed, leveraging image processing, machine learning, and deep learning techniques. The work was carried out in the framework of a collaboration between the Electrical and Electronic Measurement Research Group of Politecnico di Bari, the Optics Biotech Lab of the University of Maryland, and the University of Maryland School of Medicine.

The first objective was to evaluate the performance of five unsupervised image processing algorithms for detecting eye blinks in high-speed video sequences. This investigation, presented in **By** integrating ECG analysis with the ocular-based metrics developed in previous chapters, this final part of the thesis expands the proposed framework toward multi-parametric health monitoring, where cardiovascular and ocular signals can be jointly interpreted to provide a more comprehensive understanding of IOP dynamics and ocular biomechanics in relation to systemic physiological states.

Chapter 1, provided a detailed comparison of iris area detection, optical flow, image correlation, local binary pattern, and Gabor decomposition techniques, quantifying their precision, sensitivity, and F1-score. The analysis offered insight into the strengths and weaknesses of each approach, establishing a benchmark for subsequent robustness evaluations.

Building upon this work,

Chapter 2 focused on the noise robustness of the same five algorithms by introducing Gaussian noise into the images and applying Monte Carlo simulations. The results highlighted that image correlation outperformed other methods at low noise levels, while local binary pattern was more robust at higher noise levels. This chapter also emphasized the importance of channel selection, showing that the red channel consistently delivered better performance across noise conditions.

The third contribution of this thesis, discussed in

Chapter 3, introduced a high-speed, non-contact imaging system for tracking corneal profile dynamics during natural blinking. A deep learning–based segmentation pipeline was designed to extract the corneal contour, enabling the definition of new biomechanical metrics (time constant and displacement amplitude) to characterize corneal rebound after eyelid-induced deformation. This chapter validated the intra-subject repeatability of these metrics and demonstrated their potential clinical relevance.

Chapter 4 extended this methodology to investigate the relationship between blink-related corneal dynamics and IOP. Healthy participants were tested under baseline conditions and during the Valsalva maneuver, which naturally increases IOP. The results revealed a statistically significant reduction in the time constant under elevated IOP, suggesting that higher internal pressure accelerates corneal rebound, while the displacement amplitude remained unchanged. These findings indicate that blink-induced corneal dynamics could serve as a non-contact proxy for relative IOP changes.

Finally,

Chapter 5 addressed a different biomedical signal processing challenge: the complete segmentation of ECG waveforms (P wave, QRS complex, and T wave) acquired using a single-lead heart rate monitor. The proposed algorithm, based on wavelet transform and Otsu's thresholding method, achieved accurate detection of R-peaks, QRS segmentation, and identification of P and T waves, thus providing a reliable non-AI solution for ECG morphological analysis. Additionally, accurate ECG segmentation can clarify how systemic circulatory and autonomic factors influence the blink-induced mechanical response of the cornea and IOP fluctuations, paving the way toward integrated ocular–cardiovascular monitoring systems that can be extremely useful for remote glaucoma management.

Overall, the thesis provides a coherent framework for non-contact ocular measurement and biomedical signal segmentation, offering both methodological innovations and practical applications. Future work will focus on validating blink-induced corneal metrics in glaucoma patients, optimizing the acquisition system for real-world environments, and integrating the developed techniques into portable telemedicine devices to enable continuous home-based monitoring.

REFERENCES

[1] V. I. D'Alessandro, F. Attivissimo, A. Di Nisio, A. M. L. Lanzolla, A. Isaiah, and G. Scarcelli, "Association between Blink-related Corneal Dynamics and Intraocular Pressure," *Invest. Ophthalmol. Vis. Sci.*.

[2] V. I. D'Alessandro, A. Di Nisio, A. M. L. Lanzolla, A. Isaiah, G. Scarcelli, and F. Attivissimo, "Analysis of Corneal Dynamics During Blinking for Assessing Eye Diseases," *Measurement*.

[3] H. A. Quigley, "The number of people with glaucoma worldwide in 2010 and 2020," *Br. J. Ophthalmol.*, vol. 90, no. 3, pp. 262–267, Mar. 2006, doi: 10.1136/bjo.2005.081224.

[4] R. N. Weinreb, T. Aung, and F. A. Medeiros, "The Pathophysiology and Treatment of Glaucoma: A Review," *JAMA*, vol. 311, no. 18, p. 1901, May 2014, doi: 10.1001/jama.2014.3192.

[5] Y.-C. Tham, X. Li, T. Y. Wong, H. A. Quigley, T. Aung, and C.-Y. Cheng, "Global Prevalence of Glaucoma and Projections of Glaucoma Burden through 2040," *Ophthalmology*, vol. 121, no. 11, pp. 2081–2090, Nov. 2014, doi: 10.1016/j.ophtha.2014.05.013.

[6] V. V. Kapetanakis, M. P. Y. Chan, P. J. Foster, D. G. Cook, C. G. Owen, and A. R. Rudnicka, "Global variations and time trends in the prevalence of primary open angle glaucoma (POAG): a systematic review and meta-analysis," *Br. J. Ophthalmol.*, vol. 100, no. 1, pp. 86–93, Jan. 2016, doi: 10.1136/bjophthalmol-2015-307223.

[7] M. C. Leske, "Open-Angle Glaucoma—An Epidemiologic Overview," *Ophthalmic Epidemiol.*, vol. 14, no. 4, pp. 166–172, Jan. 2007, doi: 10.1080/09286580701501931.

[8] A. L. Coleman and S. Miglior, "Risk Factors for Glaucoma Onset and Progression," *Surv. Ophthalmol.*, vol. 53, no. 6, pp. S3–S10, Nov. 2008, doi: 10.1016/j.survophthal.2008.08.006.

[9] D. Anderson, "Normal-tension glaucoma (Low-tension glaucoma)," *Indian J. Ophthalmol.*, vol. 59, no. 7, p. 97, 2011, doi: 10.4103/0301-4738.73695.

[10] M. O. Gordon, "The Ocular Hypertension Treatment Study: Baseline Factors That Predict the Onset of Primary Open-Angle Glaucoma," *Arch. Ophthalmol.*, vol. 120, no. 6, p. 714, June 2002, doi: 10.1001/archopht.120.6.714.

[11] M. M. Whitacre and R. Stein, "Sources of error with use of Goldmann-type tonometers," *Surv. Ophthalmol.*, vol. 38, no. 1, pp. 1–30, July 1993, doi: 10.1016/0039-6257(93)90053-A.

[12] H. Goldmann and Th. Schmidt, "Über Applanationstonometrie," *Ophthalmologica*, vol. 134, no. 4, pp. 221–242, 1957, doi: 10.1159/000303213.

[13] S. J. McCafferty, K. Tetrault, A. McColgin, W. Chue, J. Levine, and M. Muller, "Modified Goldmann prism intraocular pressure measurement accuracy and correlation to corneal biomechanical metrics: multicentre randomised clinical trial," *Br. J. Ophthalmol.*, p. bjophthalmol-2018-313470, Feb. 2019, doi: 10.1136/bjophthalmol-2018-313470.

[14] J. H. Liu *et al.*, “Twenty-four-hour pattern of intraocular pressure in the aging population,” *Invest. Ophthalmol. Vis. Sci.*, vol. 40, no. 12, pp. 2912–2917, Nov. 1999.

[15] K. Mansouri and R. Weinreb, “Continuous 24-hour intraocular pressure monitoring for glaucoma - time for a paradigm change,” *Swiss Med. Wkly.*, Mar. 2012, doi: 10.4414/smw.2012.13545.

[16] A. I. Kontiola, “A new induction-based impact method for measuring intraocular pressure,” *Acta Ophthalmol. Scand.*, vol. 78, no. 2, pp. 142–145, Apr. 2000, doi: 10.1034/j.1600-0420.2000.078002142.x.

[17] A. M. Bhorade, M. O. Gordon, B. Wilson, R. N. Weinrab, and M. A. Kass, “Variability of Intraocular Pressure Measurements in Observation Participants in the Ocular Hypertension Treatment Study,” *Ophthalmology*, vol. 116, no. 4, pp. 717–724, Apr. 2009, doi: 10.1016/j.ophtha.2008.12.036.

[18] I. Yilmaz *et al.*, “Comparison of three methods of tonometry in normal subjects: Goldmann applanation tonometer, non-contact airpuff tonometer, and Tono-Pen XL,” *Clin. Ophthalmol. Auckl. NZ*, vol. 8, pp. 1069–1074, 2014, doi: 10.2147/opth.s6391.

[19] E. Y. Chow, A. L. Chlebowski, and P. P. Irazoqui, “A Miniature-Implantable RF-Wireless Active Glaucoma Intraocular Pressure Monitor,” *IEEE Trans. Biomed. Circuits Syst.*, vol. 4, no. 6, pp. 340–349, Dec. 2010, doi: 10.1109/TBCAS.2010.2081364.

[20] G. Chen *et al.*, “A cubic-millimeter energy-autonomous wireless intraocular pressure monitor,” in *2011 IEEE International Solid-State Circuits Conference*, San Francisco, CA, USA: IEEE, Feb. 2011, pp. 310–312. doi: 10.1109/ISSCC.2011.5746332.

[21] M. H. Ouda, M. Arsalan, L. Marnat, A. Shamim, and K. N. Salama, “5.2-GHz RF Power Harvester in 0.18-/spl mu/m CMOS for Implantable Intraocular Pressure Monitoring,” *IEEE Trans. Microw. Theory Tech.*, vol. 61, no. 5, pp. 2177–2184, May 2013, doi: 10.1109/TMTT.2013.2255621.

[22] P. Zolfaghari, A. D. Yalcinkaya, and O. Ferhanoglu, “MEMS Sensor-Glasses Pair for Real-Time Monitoring of Intraocular Pressure,” *IEEE Photonics Technol. Lett.*, vol. 35, no. 16, pp. 887–890, Aug. 2023, doi: 10.1109/LPT.2023.3276078.

[23] M. Leonardi, P. Leuenberger, D. Bertrand, A. Bertsch, and P. Renaud, “A soft contact lens with a MEMS strain gage embedded for intraocular pressure monitoring,” in *TRANSDUCERS ’03. 12th International Conference on Solid-State Sensors, Actuators and Microsystems. Digest of Technical Papers (Cat. No.03TH8664)*, Boston, MA, USA: IEEE, 2003, pp. 1043–1046. doi: 10.1109/SENSOR.2003.1216947.

[24] G.-Z. Chen, I.-S. Chan, L. K. K. Leung, and D. C. C. Lam, “Soft wearable contact lens sensor for continuous intraocular pressure monitoring,” *Med. Eng. Phys.*, vol. 36, no. 9, pp. 1134–1139, Sept. 2014, doi: 10.1016/j.medengphy.2014.06.005.

[25] T. Y. Kim, S. Shin, H. Choi, S. H. Jeong, D. Myung, and S. K. Hahn, “Smart Contact Lenses with a Transparent Silver Nanowire Strain Sensor for Continuous Intraocular Pressure Monitoring,” *ACS Appl. Bio Mater.*, vol. 4, no. 5, pp. 4532–4541, May 2021, doi: 10.1021/acsabm.1c00267.

[26] S. Zhang *et al.*, “On-skin ultrathin and stretchable multifunctional sensor for smart healthcare wearables,” *Npj Flex. Electron.*, vol. 6, no. 1, p. 11, Feb. 2022, doi: 10.1038/s41528-022-00140-4.

[27] T. Y. Kim *et al.*, “Wireless theranostic smart contact lens for monitoring and control of intraocular pressure in glaucoma,” *Nat. Commun.*, vol. 13, no. 1, p. 6801, Nov. 2022, doi: 10.1038/s41467-022-34597-8.

REFERENCES

[28] C. G. De Moraes, J. V. Jasien, S. Simon-Zoula, J. M. Liebmann, and R. Ritch, “Visual Field Change and 24-Hour IOP-Related Profile with a Contact Lens Sensor in Treated Glaucoma Patients,” *Ophthalmology*, vol. 123, no. 4, pp. 744–753, Apr. 2016, doi: 10.1016/j.ophtha.2015.11.020.

[29] J. Xu *et al.*, “Highly Transparent and Sensitive Graphene Sensors for Continuous and Non-invasive Intraocular Pressure Monitoring,” *ACS Appl. Mater. Interfaces*, vol. 12, no. 16, pp. 18375–18384, Apr. 2020, doi: 10.1021/acsami.0c02991.

[30] K. H. Kim, J. O. Lee, J. Du, D. Sretavan, and H. Choo, “Real-Time *In Vivo* Intraocular Pressure Monitoring Using an Optomechanical Implant and an Artificial Neural Network,” *IEEE Sens. J.*, vol. 17, no. 22, pp. 7394–7404, Nov. 2017, doi: 10.1109/JSEN.2017.2760140.

[31] C. Yang *et al.*, “Wearable and Implantable Intraocular Pressure Biosensors: Recent Progress and Future Prospects,” *Adv. Sci.*, vol. 8, no. 6, p. 2002971, Mar. 2021, doi: 10.1002/advs.202002971.

[32] R. Raveendran *et al.*, “Current Innovations in Intraocular Pressure Monitoring Biosensors for Diagnosis and Treatment of Glaucoma—Novel Strategies and Future Perspectives,” *Biosensors*, vol. 13, no. 6, p. 663, June 2023, doi: 10.3390/bios13060663.

[33] A. J. Shaw, M. J. Collins, B. A. Davis, and L. G. Carney, “Eyelid Pressure and Contact with the Ocular Surface,” *Investig. Opthalmology Vis. Sci.*, vol. 51, no. 4, p. 1911, Apr. 2010, doi: 10.1167/iovs.09-4090.

[34] E. Yoshioka, M. Yamaguchi, A. Shiraishi, T. Kono, K. Ohta, and Y. Ohashi, “Influence of Eyelid Pressure on Fluorescein Staining of Ocular Surface in Dry Eyes,” *Am. J. Ophthalmol.*, vol. 160, no. 4, pp. 685–692, Oct. 2015, doi: 10.1016/j.ajo.2015.06.028.

[35] M. Yamaguchi and A. Shiraishi, “Relationship Between Eyelid Pressure and Ocular Surface Disorders in Patients With Healthy and Dry Eyes,” *Investig. Opthalmology Vis. Sci.*, vol. 59, no. 14, p. DES56, Nov. 2018, doi: 10.1167/iovs.17-23586.

[36] S. Brody, C. Erb, R. Veit, and H. Rau, “Intraocular pressure changes: the influence of psychological stress and the Valsalva maneuver,” *Biol. Psychol.*, vol. 51, no. 1, pp. 43–57, Oct. 1999, doi: 10.1016/S0301-0511(99)00012-5.

[37] U. Aykan, M. Erdurmus, B. Yilmaz, and A. H. Bilge, “Intraocular pressure and ocular pulse amplitude variations during the Valsalva maneuver,” *Graefes Arch. Clin. Exp. Ophthalmol.*, vol. 248, no. 8, pp. 1183–1186, Aug. 2010, doi: 10.1007/s00417-010-1359-0.

[38] W.-C. Liu, S.-M. Lee, A. D. Graham, and M. C. Lin, “Effects of Eye Rubbing and Breath Holding on Corneal Biomechanical Properties and Intraocular Pressure,” *Cornea*, vol. 30, no. 8, pp. 855–860, Aug. 2011, doi: 10.1097/ICO.0b013e3182032b21.

[39] L. Sun *et al.*, “Dual effect of the Valsalva maneuver on autonomic nervous system activity, intraocular pressure, Schlemm’s canal, and iridocorneal angle morphology,” *BMC Ophthalmol.*, vol. 20, no. 1, p. 5, Dec. 2020, doi: 10.1186/s12886-019-1275-y.

[40] F. Attivissimo, V. I. D’Alessandro, A. Di Nisio, G. Scarcelli, J. Schumacher, and A. M. L. Lanzolla, “Performance evaluation of image processing algorithms for eye blinking detection,” *Measurement*, vol. 223, p. 113767, Dec. 2023, doi: 10.1016/j.measurement.2023.113767.

[41] W. P. Blount, “STUDIES OF THE MOVEMENTS OF THE EYELIDS OF ANIMALS:

BLINKING,” *Q. J. Exp. Physiol.*, vol. 18, no. 2, pp. 111–125, July 1927, doi: 10.1113/expphysiol.1927.sp000426.

[42] J. A. Stern, L. C. Walrath, and R. Goldstein, “The endogenous eyeblink,” *Psychophysiology*, vol. 21, no. 1, pp. 22–33, 1984, doi: 10.1111/j.1469-8986.1984.tb02312.x.

[43] S. Gwon, C. Cho, H. Lee, W. Lee, and K. Park, “Gaze Tracking System for User Wearing Glasses,” *Sensors*, vol. 14, no. 2, pp. 2110–2134, Jan. 2014, doi: 10.3390/s140202110.

[44] L. K. McIntire, R. A. McKinley, C. Goodyear, and J. P. McIntire, “Detection of vigilance performance using eye blinks,” *Appl. Ergon.*, vol. 45, no. 2, pp. 354–362, Mar. 2014, doi: 10.1016/j.apergo.2013.04.020.

[45] A. Z. Attiah and E. F. Khairullah, “Eye-Blink Detection System for Virtual Keyboard,” in *2021 National Computing Colleges Conference (NCCC)*, Taif, Saudi Arabia: IEEE, Mar. 2021, pp. 1–6. doi: 10.1109/NCCC49330.2021.9428797.

[46] M. Kotani *et al.*, “The dopamine D1 receptor agonist SKF-82958 effectively increases eye blinking count in common marmosets,” *Behav. Brain Res.*, vol. 300, pp. 25–30, Mar. 2016, doi: 10.1016/j.bbr.2015.11.028.

[47] N. Fan, P. Wang, L. Tang, and X. Liu, “Ocular Blood Flow and Normal Tension Glaucoma,” *BioMed Res. Int.*, vol. 2015, pp. 1–7, 2015, doi: 10.1155/2015/308505.

[48] X. Wu *et al.*, “Role of ocular blood flow in normal tension glaucoma,” *Adv. Ophthalmol. Pract. Res.*, vol. 2, no. 1, p. 100036, May 2022, doi: 10.1016/j.aopr.2022.100036.

[49] A. Goshvarpour and A. Goshvarpour, “Eye-blinking analysis as a marker of emotional states,” *Multimed. Tools Appl.*, vol. 80, no. 25, pp. 33727–33746, Oct. 2021, doi: 10.1007/s11042-021-11304-1.

[50] S. Shekari Soleimanloo *et al.*, “Eye-Blink Parameters Detect On-Road Track-Driving Impairment Following Severe Sleep Deprivation,” *J. Clin. Sleep Med.*, vol. 15, no. 09, pp. 1271–1284, Sept. 2019, doi: 10.5664/jcsm.7918.

[51] A. Bulling, J. A. Ward, H. Gellersen, and G. Tröster, “Eye Movement Analysis for Activity Recognition Using Electrooculography,” *IEEE Trans. Pattern Anal. Mach. Intell.*, vol. 33, no. 4, pp. 741–753, Apr. 2011, doi: 10.1109/TPAMI.2010.86.

[52] L. Chittaro and R. Sioni, “Exploring Eye-Blink Startle Response as a Physiological Measure for Affective Computing,” in *2013 Humaine Association Conference on Affective Computing and Intelligent Interaction*, Geneva, Switzerland: IEEE, Sept. 2013, pp. 227–232. doi: 10.1109/ACII.2013.44.

[53] A. Królak and P. Strumiłło, “Eye-blink detection system for human–computer interaction,” *Univers. Access Inf. Soc.*, vol. 11, no. 4, pp. 409–419, Nov. 2012, doi: 10.1007/s10209-011-0256-6.

[54] K. Malik and B. Smolka, “Eye blink detection using Local Binary Patterns,” in *2014 International Conference on Multimedia Computing and Systems (ICMCS)*, Marrakech, Morocco: IEEE, Apr. 2014, pp. 385–390. doi: 10.1109/ICMCS.2014.6911268.

[55] A. Kuwahara, R. Hirakawa, H. Kawano, K. Nakashi, and Y. Nakatoh, “Eye Fatigue Prediction System Using Blink Detection Based on Eye Image,” in *2021 IEEE International Conference on Consumer Electronics (ICCE)*, Las Vegas, NV, USA: IEEE, Jan. 2021, pp. 1–3. doi: 10.1109/ICCE50685.2021.9427681.

[56] Assit. Prof. and MSc. Student, “Efficient Eye Blink Detection Method for disabled-

helping domain," *Int. J. Adv. Comput. Sci. Appl.*, vol. 5, no. 5, 2014, doi: 10.14569/IJACSA.2014.050530.

[57] P. Kowalczyk and D. Sawicki, "Blink and wink detection as a control tool in multimodal interaction," *Multimed. Tools Appl.*, vol. 78, no. 10, pp. 13749–13765, May 2019, doi: 10.1007/s11042-018-6554-8.

[58] W. Tansakul and P. Tangamchit, "Fatigue Driver Detection System Using a Combination of Blinking Rate and Driving Inactivity," *J. Autom. Control Eng.*, vol. 3, no. 6, pp. 33–39, 2015, doi: 10.12720/joace.4.1.33-39.

[59] S. Al-gawwam and M. Benaissa, "Robust Eye Blink Detection Based on Eye Landmarks and Savitzky–Golay Filtering," *Information*, vol. 9, no. 4, p. 93, Apr. 2018, doi: 10.3390/info9040093.

[60] J. D. Rodriguez, K. J. Lane, G. W. Ousler, E. Angjeli, L. M. Smith, and M. B. Abelson, "Blink: Characteristics, Controls, and Relation to Dry Eyes," *Curr. Eye Res.*, vol. 43, no. 1, pp. 52–66, Jan. 2018, doi: 10.1080/02713683.2017.1381270.

[61] M. Bruynooghe, "New hybrid opto-electronic method for fast and unsupervised object detection," *Opt. Eng.*, vol. 42, no. 11, p. 3352, Nov. 2003, doi: 10.1117/1.1612511.

[62] C. Jin *et al.*, "Object recognition in medical images via anatomy-guided deep learning," *Med. Image Anal.*, vol. 81, p. 102527, Oct. 2022, doi: 10.1016/j.media.2022.102527.

[63] Rein-Lien Hsu, M. Abdel-Mottaleb, and A. K. Jain, "Face detection in color images," *IEEE Trans. Pattern Anal. Mach. Intell.*, vol. 24, no. 5, pp. 696–706, May 2002, doi: 10.1109/34.1000242.

[64] N. Otsu, "A Threshold Selection Method from Gray-Level Histograms," *IEEE Trans. Syst. Man Cybern.*, vol. 9, no. 1, pp. 62–66, Jan. 1979, doi: 10.1109/TSMC.1979.4310076.

[65] Xuan Dong *et al.*, "Fast efficient algorithm for enhancement of low lighting video," in *2011 IEEE International Conference on Multimedia and Expo*, Barcelona, Spain: IEEE, July 2011, pp. 1–6. doi: 10.1109/ICME.2011.6012107.

[66] G. Farnebäck, "Two-Frame Motion Estimation Based on Polynomial Expansion," in *Image Analysis*, vol. 2749, J. Bigun and T. Gustavsson, Eds., in Lecture Notes in Computer Science, vol. 2749. , Berlin, Heidelberg: Springer Berlin Heidelberg, 2003, pp. 363–370. doi: 10.1007/3-540-45103-X_50.

[67] A. Fogelton and W. Benesova, "Eye blink detection based on motion vectors analysis," *Comput. Vis. Image Underst.*, vol. 148, pp. 23–33, July 2016, doi: 10.1016/j.cviu.2016.03.011.

[68] Z. Wang and X. Yang, "Moving Target Detection and Tracking Based on Pyramid Lucas-Kanade Optical Flow," in *2018 IEEE 3rd International Conference on Image, Vision and Computing (ICIVC)*, Chongqing: IEEE, June 2018, pp. 66–69. doi: 10.1109/ICIVC.2018.8492786.

[69] M. Awais, N. Badruddin, and M. Drieberg, "Automated eye blink detection and tracking using template matching," in *2013 IEEE Student Conference on Research and Developement*, Putrajaya, Malaysia: IEEE, Dec. 2013, pp. 79–83. doi: 10.1109/SCOReD.2013.7002546.

[70] N. Golyandina and A. Zhigljavsky, *Singular Spectrum Analysis for Time Series*. in SpringerBriefs in Statistics. Berlin, Heidelberg: Springer Berlin Heidelberg, 2013. doi: 10.1007/978-3-642-34913-3.

[71] T. Ojala, M. Pietikainen, and T. Maenpaa, "Multiresolution gray-scale and rotation

invariant texture classification with local binary patterns," *IEEE Trans. Pattern Anal. Mach. Intell.*, vol. 24, no. 7, pp. 971–987, July 2002, doi: 10.1109/TPAMI.2002.1017623.

[72] Jiang-Wei Li, "Eye blink detection based on multiple Gabor response waves," in *2008 International Conference on Machine Learning and Cybernetics*, Kunming, China: IEEE, July 2008, pp. 2852–2856. doi: 10.1109/ICMLC.2008.4620894.

[73] A. Kulkarni, D. Chong, and F. A. Batarseh, "Foundations of data imbalance and solutions for a data democracy," in *Data Democracy*, Elsevier, 2020, pp. 83–106. doi: 10.1016/B978-0-12-818366-3.00005-8.

[74] A. Fernández, S. García, M. Galar, R. C. Prati, B. Krawczyk, and F. Herrera, *Learning from Imbalanced Data Sets*. Cham: Springer International Publishing, 2018. doi: 10.1007/978-3-319-98074-4.

[75] A. Di Nisio, V. I. D'Alessandro, G. Scarcelli, A. M. L. Lanzolla, and F. Attivissimo, "Noise robustness evaluation of image processing algorithms for eye blinking detection," *Measurement*, vol. 239, p. 115508, Jan. 2025, doi: 10.1016/j.measurement.2024.115508.

[76] O. Korsun and V. Yurko, "Convolutional neural networks emotion recognition and blink characteristics analysis for operator state estimation," *Procedia Comput. Sci.*, vol. 186, pp. 293–298, 2021, doi: 10.1016/j.procs.2021.04.148.

[77] J. Acharjee and S. Deb, "Identification of Significant Eye Blink for Tangible Human Computer Interaction," in *2021 International Conference on Advance Computing and Innovative Technologies in Engineering (ICACITE)*, Greater Noida, India: IEEE, Mar. 2021, pp. 179–183. doi: 10.1109/ICACITE51222.2021.9404595.

[78] W. Luo, J. Cao, K. Ishikawa, and D. Ju, "A Human-Computer Control System Based on Intelligent Recognition of Eye Movements and Its Application in Wheelchair Driving," *Multimodal Technol. Interact.*, vol. 5, no. 9, p. 50, Aug. 2021, doi: 10.3390/mti5090050.

[79] R. A. Al Mudhafar and N. K. El Abbadi, "Noise in Digital Image Processing: A Review Study," in *2022 3rd Information Technology To Enhance e-learning and Other Application (IT-ELA)*, Baghdad, Iraq: IEEE, Dec. 2022, pp. 79–84. doi: 10.1109/IT-ELA57378.2022.10107965.

[80] W. Liu and W. Lin, "Additive White Gaussian Noise Level Estimation in SVD Domain for Images," *IEEE Trans. Image Process.*, vol. 22, no. 3, pp. 872–883, Mar. 2013, doi: 10.1109/TIP.2012.2219544.

[81] A. K. Boyat and B. K. Joshi, "A Review Paper : Noise Models in Digital Image Processing," *Signal Image Process. Int. J.*, vol. 6, no. 2, pp. 63–75, Apr. 2015, doi: 10.5121/sipij.2015.6206.

[82] M. Mafi, H. Martin, M. Cabrerizo, J. Andrian, A. Barreto, and M. Adjouadi, "A comprehensive survey on impulse and Gaussian denoising filters for digital images," *Signal Process.*, vol. 157, pp. 236–260, Apr. 2019, doi: 10.1016/j.sigpro.2018.12.006.

[83] J. Z. Lim, J. Mountstephens, and J. Teo, "Emotion Recognition Using Eye-Tracking: Taxonomy, Review and Current Challenges," *Sensors*, vol. 20, no. 8, p. 2384, Apr. 2020, doi: 10.3390/s20082384.

[84] A. Goshvarpour and A. Goshvarpour, "Human Emotion Recognition using Polar-Based Lagged Poincare Plot Indices of Eye-Blinking Data," *Int. J. Comput. Intell. Appl.*, vol. 20, no. 04, p. 2150023, Dec. 2021, doi: 10.1142/S1469026821500231.

REFERENCES

[85] R. L. Harrison, C. Granja, and C. Leroy, "Introduction to Monte Carlo Simulation," presented at the NUCLEAR PHYSICS METHODS AND ACCELERATORS IN BIOLOGY AND MEDICINE: Fifth International Summer School on Nuclear Physics Methods and Accelerators in Biology and Medicine, Bratislava (Slovakia), 2010, pp. 17–21. doi: 10.1063/1.3295638.

[86] A. Alsaiari, R. Rustagi, A. Alhakamy, M. M. Thomas, and A. G. Forbes, "Image Denoising Using A Generative Adversarial Network," in *2019 IEEE 2nd International Conference on Information and Computer Technologies (ICICT)*, Kahului, HI, USA: IEEE, Mar. 2019, pp. 126–132. doi: 10.1109/INFOCT.2019.8710893.

[87] Y. Huo and S. Yoon, "A survey on deep learning-based Monte Carlo denoising," *Comput. Vis. Media*, vol. 7, no. 2, pp. 169–185, June 2021, doi: 10.1007/s41095-021-0209-9.

[88] M. Lalonde, D. Byrns, L. Gagnon, N. Teasdale, and D. Laurendeau, "Real-time eye blink detection with GPU-based SIFT tracking," in *Fourth Canadian Conference on Computer and Robot Vision (CRV '07)*, Montreal, QC, Canada: IEEE, May 2007, pp. 481–487. doi: 10.1109/CRV.2007.54.

[89] W. O. Lee, E. C. Lee, and K. R. Park, "Blink detection robust to various facial poses," *J. Neurosci. Methods*, vol. 193, no. 2, pp. 356–372, Nov. 2010, doi: 10.1016/j.jneumeth.2010.08.034.

[90] A. Panning, A. Al-Hamadi, and B. Michaelis, "A color based approach for eye blink detection in image sequences," in *2011 IEEE International Conference on Signal and Image Processing Applications (ICSIPA)*, Kuala Lumpur, Malaysia: IEEE, Nov. 2011, pp. 40–45. doi: 10.1109/ICSIPA.2011.6144085.

[91] I. Choi, S. Han, and D. Kim, "Eye Detection and Eye Blink Detection Using AdaBoost Learning and Grouping," in *2011 Proceedings of 20th International Conference on Computer Communications and Networks (ICCCN)*, Lahaina, HI, USA: IEEE, July 2011, pp. 1–4. doi: 10.1109/ICCCN.2011.6005896.

[92] K. Malik and B. Smolka, "Eye blink detection using Local Binary Patterns," in *2014 International Conference on Multimedia Computing and Systems (ICMCS)*, Marrakech, Morocco: IEEE, Apr. 2014, pp. 385–390. doi: 10.1109/ICMCS.2014.6911268.

[93] C. Ryan *et al.*, "Real-time face & eye tracking and blink detection using event cameras," *Neural Netw.*, vol. 141, pp. 87–97, Sept. 2021, doi: 10.1016/j.neunet.2021.03.019.

[94] A. Kotecha, "What Biomechanical Properties of the Cornea Are Relevant for the Clinician?," *Surv. Ophthalmol.*, vol. 52, no. 6, pp. S109–S114, Nov. 2007, doi: 10.1016/j.survophthal.2007.08.004.

[95] S. Stevens, C. Gilbert, and N. Astbury, "How to measure intraocular pressure: applanation tonometry," *Community Eye Health*, vol. 20, no. 64, pp. 74–75, Dec. 2007.

[96] W. Lau and D. Pye, "A Clinical Description of Ocular Response Analyzer Measurements," *Investig. Opthalmology Vis. Sci.*, vol. 52, no. 6, p. 2911, May 2011, doi: 10.1167/iovs.10-6763.

[97] S. Bamdad and Y. Vatan, "Goldmann Applanation Tonometry: Using a Red-Free Filter for Mass Screening," *Med. Hypothesis Discov. Innov. Ophthalmol. J.*, vol. 6, no. 1, pp. 22–23, 2017.

[98] W. Wang, M. He, H. He, C. Zhang, H. Jin, and X. Zhong, "Corneal biomechanical metrics of healthy Chinese adults using Corvis ST," *Contact Lens Anterior Eye*, vol.

40, no. 2, pp. 97–103, Apr. 2017, doi: 10.1016/j.clae.2016.12.003.

[99] M.-R. Sedaghat *et al.*, "Corneal Biomechanical Properties in Varying Severities of Myopia," *Front. Bioeng. Biotechnol.*, vol. 8, p. 595330, Jan. 2021, doi: 10.3389/fbioe.2020.595330.

[100] P. Zhang *et al.*, "Evaluation of changes in corneal biomechanics after orthokeratology using Corvis ST," *Contact Lens Anterior Eye*, vol. 47, no. 1, p. 102100, Feb. 2024, doi: 10.1016/j.clae.2023.102100.

[101] C. Ye, M. Yu, G. Lai, and V. Jhanji, "Variability of Corneal Deformation Response in Normal and Keratoconic Eyes," *Optom. Vis. Sci.*, vol. 92, no. 7, pp. e149–e153, July 2015, doi: 10.1097/OPX.0000000000000628.

[102] J. Steinberg, T. Katz, K. Lücke, A. Frings, V. Druchkiv, and S. J. Linke, "Screening for Keratoconus With New Dynamic Biomechanical In Vivo Scheimpflug Analyses," *Cornea*, vol. 34, no. 11, pp. 1404–1412, Nov. 2015, doi: 10.1097/ICO.0000000000000598.

[103] J. Wang, Y. Li, Y. Jin, X. Yang, C. Zhao, and Q. Long, "Corneal Biomechanical Properties in Myopic Eyes Measured by a Dynamic Scheimpflug Analyzer," *J. Ophthalmol.*, vol. 2015, pp. 1–8, 2015, doi: 10.1155/2015/161869.

[104] A.-Y. Yu *et al.*, "Corneal biomechanical properties in myopic eyes evaluated via Scheimpflug imaging," *BMC Ophthalmol.*, vol. 20, no. 1, p. 279, Dec. 2020, doi: 10.1186/s12886-020-01530-w.

[105] Q. Long, J. Wang, X. Yang, Y. Jin, F. Ai, and Y. Li, "Assessment of Corneal Biomechanical Properties by CorVis ST in Patients with Dry Eye and in Healthy Subjects," *J. Ophthalmol.*, vol. 2015, pp. 1–7, 2015, doi: 10.1155/2015/380624.

[106] V. Satitpitakul, P. Taweekitikul, V. Puangsricharern, N. Kasetsuwan, U. Reinprayoon, and T. Kittipibul, "Alteration of corneal biomechanical properties in patients with dry eye disease," *PLOS ONE*, vol. 16, no. 7, p. e0254442, July 2021, doi: 10.1371/journal.pone.0254442.

[107] W. Wang, S. Du, and X. Zhang, "Corneal Deformation Response in Patients With Primary Open-Angle Glaucoma and in Healthy Subjects Analyzed by Corvis ST," *Investig. Opthalmology Vis. Sci.*, vol. 56, no. 9, p. 5557, Aug. 2015, doi: 10.1167/iovs.15-16926.

[108] M. Lin *et al.*, "Effects of eyelid pressure on corneal tomography and biomechanics: Quantitative analysis using a novel blepharo-tensiometer," *Contact Lens Anterior Eye J. Br. Contact Lens Assoc.*, vol. 47, no. 6, p. 102313, Dec. 2024, doi: 10.1016/j.clae.2024.102313.

[109] O. Ronneberger, P. Fischer, and T. Brox, "U-Net: Convolutional Networks for Biomedical Image Segmentation," in *Medical Image Computing and Computer-Assisted Intervention – MICCAI 2015*, vol. 9351, N. Navab, J. Hornegger, W. M. Wells, and A. F. Frangi, Eds., in Lecture Notes in Computer Science, vol. 9351. , Cham: Springer International Publishing, 2015, pp. 234–241. doi: 10.1007/978-3-319-24574-4_28.

[110] H. M and S. M.N, "A Review on Evaluation Metrics for Data Classification Evaluations," *Int. J. Data Min. Knowl. Manag. Process*, vol. 5, no. 2, pp. 01–11, Mar. 2015, doi: 10.5121/ijdkp.2015.5201.

[111] G. Nousias, E.-K. Panagiotopoulou, K. Delibasis, A.-M. Chaliasou, A.-M. Tzounakou, and G. Labiris, "Video-Based Eye Blink Identification and Classification," *IEEE J. Biomed. Health Inform.*, vol. 26, no. 7, pp. 3284–3293, July 2022, doi: 10.1109/jbhi.2022.3153407.

[112] C. Garbin, X. Zhu, and O. Marques, "Dropout vs. batch normalization: an empirical study of their impact to deep learning," *Multimed. Tools Appl.*, vol. 79, no. 19–20, pp. 12777–12815, May 2020, doi: 10.1007/s11042-019-08453-9.

[113] D. P. Kingma and J. Ba, "Adam: A Method for Stochastic Optimization," 2014, *arXiv*. doi: 10.48550/ARXIV.1412.6980.

[114] V. Badrinarayanan, A. Kendall, and R. Cipolla, "SegNet: A Deep Convolutional Encoder-Decoder Architecture for Image Segmentation," *IEEE Trans. Pattern Anal. Mach. Intell.*, vol. 39, no. 12, pp. 2481–2495, Dec. 2017, doi: 10.1109/TPAMI.2016.2644615.

[115] C. H. Sudre, W. Li, T. Vercauteren, S. Ourselin, and M. Jorge Cardoso, "Generalised Dice Overlap as a Deep Learning Loss Function for Highly Unbalanced Segmentations," in *Deep Learning in Medical Image Analysis and Multimodal Learning for Clinical Decision Support*, vol. 10553, M. J. Cardoso, T. Arbel, G. Carneiro, T. Syeda-Mahmood, J. M. R. S. Tavares, M. Moradi, A. Bradley, H. Greenspan, J. P. Papa, A. Madabhushi, J. C. Nascimento, J. S. Cardoso, V. Belagiannis, and Z. Lu, Eds., in Lecture Notes in Computer Science, vol. 10553. , Cham: Springer International Publishing, 2017, pp. 240–248. doi: 10.1007/978-3-319-67558-9_28.

[116] S. A. Taghanaki *et al.*, "Combo loss: Handling input and output imbalance in multi-organ segmentation," *Comput. Med. Imaging Graph.*, vol. 75, pp. 24–33, July 2019, doi: 10.1016/j.compmedimag.2019.04.005.

[117] J. Ma *et al.*, "Loss odyssey in medical image segmentation," *Med. Image Anal.*, vol. 71, p. 102035, July 2021, doi: 10.1016/j.media.2021.102035.

[118] G. Peyré and L. D. Cohen, "Geodesic Methods for Shape and Surface Processing," in *Advances in Computational Vision and Medical Image Processing*, vol. 13, J. M. R. S. Tavares and R. M. N. Jorge, Eds., Dordrecht: Springer Netherlands, 2009, pp. 29–56. doi: 10.1007/978-1-4020-9086-8_2.

[119] I. Goldberg and C. I. Clement, "The Water Drinking Test," *Am. J. Ophthalmol.*, vol. 150, no. 4, pp. 447–449, Oct. 2010, doi: 10.1016/j.ajo.2010.06.035.

[120] S. A. Read and M. J. Collins, "Water drinking influences eye length and IOP in young healthy subjects," *Exp. Eye Res.*, vol. 91, no. 2, pp. 180–185, Aug. 2010, doi: 10.1016/j.exer.2010.04.015.

[121] W. Chen *et al.*, "Influence of the Water-Drinking Test on Intraocular Pressure, Schlemm's Canal, and Autonomic Nervous System Activity," *Investig. Opthalmology Vis. Sci.*, vol. 59, no. 8, p. 3232, July 2018, doi: 10.1167/iovs.18-23909.

[122] B. Thylefors and A. D. Négrel, "The global impact of glaucoma," *Bull. World Health Organ.*, vol. 72, no. 3, pp. 323–326, 1994.

[123] J. M. Kang and A. P. Tanna, "Glaucoma," *Med. Clin. North Am.*, vol. 105, no. 3, pp. 493–510, May 2021, doi: 10.1016/j.mcna.2021.01.004.

[124] A. A. V. Cruz, D. M. Garcia, C. T. Pinto, and S. P. Cechetti, "Spontaneous Eyeblink Activity," *Ocul. Surf.*, vol. 9, no. 1, pp. 29–41, Jan. 2011, doi: 10.1016/S1542-0124(11)70007-6.

[125] C. W. McMonnies, "The clinical and experimental significance of blinking behavior," *J. Optom.*, vol. 13, no. 2, pp. 74–80, Apr. 2020, doi: 10.1016/j.optom.2019.09.002.

[126] A. Kotecha, E. White, P. G. Schlottmann, and D. F. Garway-Heath, "Intraocular Pressure Measurement Precision with the Goldmann Applanation, Dynamic

Contour, and Ocular Response Analyzer Tonometers," *Ophthalmology*, vol. 117, no. 4, pp. 730–737, Apr. 2010, doi: 10.1016/j.ophtha.2009.09.020.

[127] X. Feng, J. Li, Z. Hua, and F. Zhang, "Low-light image enhancement based on multi-illumination estimation," *Appl. Intell.*, vol. 51, no. 7, pp. 5111–5131, July 2021, doi: 10.1007/s10489-020-02119-y.

[128] "Icare IC200 Instruction Manual." Icare Finland Oy, 2023. [Online]. Available: https://materialbank.icare-world.com/wp-content/uploads/2023/06/iCare_IC200_instruction_manual_TA031-046-EN-5.0.pdf?mtime=1687243513;2023

[129] S. Nakakura *et al.*, "Evaluation of rebound tonometer iCare IC200 as compared with IcarePRO and Goldmann applanation tonometer in patients with glaucoma," *Eye Vis.*, vol. 8, no. 1, p. 25, Dec. 2021, doi: 10.1186/s40662-021-00249-z.

[130] S. V. Badakere, R. Chary, N. S. Choudhari, H. L. Rao, C. Garudadri, and S. Senthil, "Agreement of Intraocular Pressure Measurement of Icare ic200 with Goldmann Applanation Tonometer in Adult Eyes with Normal Cornea," *Ophthalmol. Glaucoma*, vol. 4, no. 3, pp. 238–243, May 2021, doi: 10.1016/j.ogla.2021.04.002.

[131] U. Aykan, M. Erdurmus, B. Yilmaz, and A. H. Bilge, "Intraocular pressure and ocular pulse amplitude variations during the Valsalva maneuver," *Graefes Arch. Clin. Exp. Ophthalmol.*, vol. 248, no. 8, pp. 1183–1186, Aug. 2010, doi: 10.1007/s00417-010-1359-0.

[132] E. Sakai, A. Shiraishi, M. Yamaguchi, K. Ohta, and Y. Ohashi, "Blepharo-tensiometer: new eyelid pressure measurement system using tactile pressure sensor," *Eye Contact Lens*, vol. 38, no. 5, pp. 326–330, Sept. 2012, doi: 10.1097/ICL.0b013e318268610a.

[133] H. Pult, S. G. P. Tosatti, N. D. Spencer, J.-M. Asfour, M. Ebenhoch, and P. J. Murphy, "Spontaneous Blinking from a Tribological Viewpoint," *Ocul. Surf.*, vol. 13, no. 3, pp. 236–249, July 2015, doi: 10.1016/j.jtos.2014.12.004.

[134] J. Wang *et al.*, "Assessment of Eyelid Pressure Using a Novel Pressure Measurement Device in Patients With Moderate-to-Severe Dry Eye Disease," *Front. Med.*, vol. 9, p. 833576, 2022, doi: 10.3389/fmed.2022.833576.

[135] T. Buehren, M. J. Collins, and L. Carney, "Corneal aberrations and reading," *Optom. Vis. Sci. Off. Publ. Am. Acad. Optom.*, vol. 80, no. 2, pp. 159–166, Feb. 2003, doi: 10.1097/00006324-200302000-00012.

[136] M. J. Collins, T. Buehren, T. Trevor, M. Statham, J. Hansen, and D. A. Cavanagh, "Factors influencing lid pressure on the cornea," *Eye Contact Lens*, vol. 32, no. 4, pp. 168–173, July 2006, doi: 10.1097/01.icl.0000189193.28870.81.

[137] A. J. Shaw, M. J. Collins, B. A. Davis, and L. G. Carney, "Corneal refractive changes due to short-term eyelid pressure in downward gaze," *J. Cataract Refract. Surg.*, vol. 34, no. 9, pp. 1546–1553, Sept. 2008, doi: 10.1016/j.jcrs.2008.05.047.

[138] A. J. Shaw, M. J. Collins, B. A. Davis, and L. G. Carney, "Eyelid pressure: inferences from corneal topographic changes," *Cornea*, vol. 28, no. 2, pp. 181–188, Feb. 2009, doi: 10.1097/ICO.0b013e31818a7d61.

[139] A. Martínez-Abad and D. P. Piñero, "New perspectives on the detection and progression of keratoconus," *J. Cataract Refract. Surg.*, vol. 43, no. 9, pp. 1213–1227, Sept. 2017, doi: 10.1016/j.jcrs.2017.07.021.

[140] Z. Pniakowska, P. Jurowski, and J. Wierzbowska, "Clinical Evaluation of Corneal Biomechanics following Laser Refractive Surgery in Myopic Eyes: A Review of the Literature," *J. Clin. Med.*, vol. 12, no. 1, p. 243, Dec. 2022, doi: 10.3390/jcm12010243.

[141] Y. Barkana, "Clinical Utility of Intraocular Pressure Monitoring Outside of Normal Office Hours in Patients With Glaucoma," *Arch. Ophthalmol.*, vol. 124, no. 6, p. 793, June 2006, doi: 10.1001/archopht.124.6.793.

[142] N. C. Sharts-Hopko and C. Glynn-Milley, "PRIMARY OPEN-ANGLE GLAUCOMA," *AJN Am. J. Nurs.*, vol. 109, no. 2, pp. 40–47, Feb. 2009, doi: 10.1097/01.NAJ.0000345434.37734.ee.

[143] D. Y. L. Leung and C. C. Tham, "Normal-tension glaucoma: Current concepts and approaches-A review," *Clin. Experiment. Ophthalmol.*, vol. 50, no. 2, pp. 247–259, Mar. 2022, doi: 10.1111/ceo.14043.

[144] B. L. Lee, R. Bathija, and R. N. Weinreb, "The definition of normal-tension glaucoma," *J. Glaucoma*, vol. 7, no. 6, pp. 366–371, Dec. 1998.

[145] B. Song and J. Caprioli, "New directions in the treatment of normal tension glaucoma," *Indian J. Ophthalmol.*, vol. 62, no. 5, p. 529, 2014, doi: 10.4103/0301-4738.133481.

[146] E. Gramer and W. Leydhecker, "Glaukom ohne Hochdruck. Eine klinische Studie*," *Klin. Monatsblätter Für Augenheilkd.*, vol. 186, no. 04, pp. 262–267, Apr. 1985, doi: 10.1055/s-2008-1050918.

[147] J. Mallick, L. Devi, P. K. Malik, and J. Mallick, "Update on Normal Tension Glaucoma," *J. Ophthalmic Vis. Res.*, vol. 11, no. 2, pp. 204–208, 2016, doi: 10.4103/2008-322X.183914.

[148] M. B. Shields, "Normal-tension glaucoma: is it different from primary open-angle glaucoma?:," *Curr. Opin. Ophthalmol.*, vol. 19, no. 2, pp. 85–88, Mar. 2008, doi: 10.1097/ICU.0b013e3282f3919b.

[149] J. B. Jonas, N. Wang, Y. X. Wang, Q. S. You, D. Yang, and L. Xu, "Ocular hypertension: general characteristics and estimated cerebrospinal fluid pressure. The Beijing Eye Study 2011," *PloS One*, vol. 9, no. 7, p. e100533, 2014, doi: 10.1371/journal.pone.0100533.

[150] C. Evinger, M. D. Shaw, C. K. Peck, K. A. Manning, and R. Baker, "Blinking and associated eye movements in humans, guinea pigs, and rabbits," *J. Neurophysiol.*, vol. 52, no. 2, pp. 323–339, Aug. 1984, doi: 10.1152/jn.1984.52.2.323.

[151] L. J. Bour, M. Aramideh, and B. W. Ongerboer De Visser, "Neurophysiological Aspects of Eye and Eyelid Movements During Blinking in Humans," *J. Neurophysiol.*, vol. 83, no. 1, pp. 166–176, Jan. 2000, doi: 10.1152/jn.2000.83.1.166.

[152] D. Mas, B. Domenech, J. Espinosa, J. Pérez, C. Hernández, and C. Illueca, "Noninvasive measurement of eye retraction during blinking," *Opt. Lett.*, vol. 35, no. 11, pp. 1884–1886, June 2010, doi: 10.1364/OL.35.001884.

[153] J. Perez, J. Espinosa, B. Domenech, D. Mas, and C. Illueca, "Blinking kinematics description through non-invasive measurement," *J. Mod. Opt.*, vol. 58, no. 19–20, pp. 1857–1863, Nov. 2011, doi: 10.1080/09500340.2011.554898.

[154] D. Robert Iskander and H. T. Kasprzak, "Dynamics in longitudinal eye movements and corneal shape," *Ophthalmic Physiol. Opt. J. Br. Coll. Ophthalmic Opt. Optom.*, vol. 26, no. 6, pp. 572–579, Nov. 2006, doi: 10.1111/j.1475-1313.2006.00415.x.

[155] S. M. Willett, S. K. Maenner, and J. P. Mayo, "The perceptual consequences and

neurophysiology of eye blinks,” *Front. Syst. Neurosci.*, vol. 17, p. 1242654, Aug. 2023, doi: 10.3389/fnsys.2023.1242654.

[156] O. Bergamin, S. Bizzarri, and D. Straumann, “Ocular torsion during voluntary blinks in humans,” *Invest. Ophthalmol. Vis. Sci.*, vol. 43, no. 11, pp. 3438–3443, Nov. 2002.

[157] J. Kirchner, T. Watson, J. Bauer, and M. Lappe, “High-speed MRI recordings of eyeball lifting, retraction and compression during blinks,” May 12, 2022, *Neuroscience*. doi: 10.1101/2022.05.11.491482.

[158] S. V, S. Bhansali, R. Kosti, P. Balananda, and N. L, “Intraocular pressure changes during Valsalva maneuver,” *Natl. J. Physiol. Pharm. Pharmacol.*, vol. 13, pp. 1887–1892, 2023, doi: 10.5455/njppp.2023.13.07338202323072023.

[159] R. Stodtmeister, M. Heyde, S. Georgii, E. Matthè, E. Spoerl, and L. E. Pillunat, “Retinal venous pressure is higher than the airway pressure and the intraocular pressure during the Valsalva manoeuvre,” *Acta Ophthalmol. (Copenh.)*, vol. 96, no. 1, pp. e68–e73, Feb. 2018, doi: 10.1111/aos.13485.

[160] N. Kara and S. Kenan, “Effect of refractive status on Valsalva-induced anterior segment changes,” *Int. Ophthalmol.*, vol. 38, no. 3, pp. 1205–1210, June 2018, doi: 10.1007/s10792-017-0583-6.

[161] L. D. Palma, V. I. D’Alessandro, F. Attivissimo, A. D. Nisio, and A. M. L. Lanzolla, “ECG wave segmentation algorithm for complete P-QRS-T detection,” in *2023 IEEE International Symposium on Medical Measurements and Applications (MeMeA)*, Jeju, Korea, Republic of: IEEE, June 2023, pp. 1–6. doi: 10.1109/memea57477.2023.10171894.

[162] E. Olvera Lopez, B. D. Ballard, and A. Jan, “Cardiovascular Disease,” in *StatPearls*, Treasure Island (FL): StatPearls Publishing, 2025. Accessed: Aug. 14, 2025. [Online]. Available: http://www.ncbi.nlm.nih.gov/books/NBK535419/

[163] S. C. Mukhopadhyay, “Wearable Sensors for Human Activity Monitoring: A Review,” *IEEE Sens. J.*, vol. 15, no. 3, pp. 1321–1330, Mar. 2015, doi: 10.1109/JSEN.2014.2370945.

[164] L. D’Alvia *et al.*, “Accuracy evaluation of an ECG device for heart failure patients self-monitoring: a preliminary study,” in *2022 IEEE International Symposium on Medical Measurements and Applications (MeMeA)*, Messina, Italy: IEEE, June 2022, pp. 1–6. doi: 10.1109/MeMeA54994.2022.9856535.

[165] F. Goodarzy, E. S. Skafidas, and S. Gambini, “Feasibility of Energy-Autonomous Wireless Microsensors for Biomedical Applications: Powering and Communication,” *IEEE Rev. Biomed. Eng.*, vol. 8, pp. 17–29, 2015, doi: 10.1109/RBME.2014.2346487.

[166] K. Hung, Y. T. Zhang, and B. Tai, “Wearable medical devices for tele-home healthcare,” in *The 26th Annual International Conference of the IEEE Engineering in Medicine and Biology Society*, San Francisco, CA, USA: IEEE, 2004, pp. 5384–5387. doi: 10.1109/IEMBS.2004.1404503.

[167] N. Giaquinto, M. Scarpetta, M. A. Ragolia, and P. Pappalardi, “Real-time drip infusion monitoring through a computer vision system,” in *2020 IEEE International Symposium on Medical Measurements and Applications (MeMeA)*, Bari, Italy: IEEE, June 2020, pp. 1–5. doi: 10.1109/MeMeA49120.2020.9137359.

[168] L. Grajales and I. V. Nicolaescu, “Wearable Multisensor Heart Rate Monitor,” in

International Workshop on Wearable and Implantable Body Sensor Networks (BSN'06), Cambridge, MA, USA: IEEE, 2006, pp. 154–157. doi: 10.1109/BSN.2006.58.

[169] M. Scarpetta, M. Spadavecchia, G. Andria, M. A. Ragolia, and N. Giaquinto, "Simultaneous Measurement of Heartbeat Intervals and Respiratory Signal using a Smartphone," in *2021 IEEE International Symposium on Medical Measurements and Applications (MeMeA)*, Lausanne, Switzerland: IEEE, June 2021, pp. 1–5. doi: 10.1109/MeMeA52024.2021.9478711.

[170] E. F. Bakke, J. Hisdal, and S. O. Semb, "Intraocular Pressure Increases in Parallel with Systemic Blood Pressure during Isometric Exercise," *Investig. Opthalmology Vis. Sci.*, vol. 50, no. 2, p. 760, Feb. 2009, doi: 10.1167/iovs.08-2508.

[171] P. Valmaggia, J. Wolleb, F. Bieder, H. P. N. Scholl, P. C. Cattin, and P. M. Maloca, "Heart-retina time analysis using electrocardiogram-coupled time-resolved dynamic optical coherence tomography," *Sci. Rep.*, vol. 15, no. 1, p. 385, Jan. 2025, doi: 10.1038/s41598-024-84417-w.

[172] Y. Yoshida, H. Takei, M. Ukisu, K. Takagi, and M. Tanito, "Heart Rate Variability Time-Domain Analysis Across Glaucoma Subtypes," *Biomedicines*, vol. 13, no. 4, p. 893, Apr. 2025, doi: 10.3390/biomedicines13040893.

[173] N. I. Kurysheva, T. Y. Ryabova, and V. N. Shlapak, "Heart rate variability: the comparison between high tension and normal tension glaucoma," *EPMA J.*, vol. 9, no. 1, pp. 35–45, Mar. 2018, doi: 10.1007/s13167-017-0124-4.

[174] P. E. McSharry, G. D. Clifford, L. Tarassenko, and L. A. Smith, "A dynamical model for generating synthetic electrocardiogram signals," *IEEE Trans. Biomed. Eng.*, vol. 50, no. 3, pp. 289–294, Mar. 2003, doi: 10.1109/TBME.2003.808805.

[175] J. Aspuru *et al.*, "Segmentation of the ECG Signal by Means of a Linear Regression Algorithm," *Sensors*, vol. 19, no. 4, p. 775, Feb. 2019, doi: 10.3390/s19040775.

[176] J. Pan and W. J. Tompkins, "A Real-Time QRS Detection Algorithm," *IEEE Trans. Biomed. Eng.*, vol. BME-32, no. 3, pp. 230–236, Mar. 1985, doi: 10.1109/TBME.1985.325532.

[177] N. Uchaipichat and S. Inban, "Development of QRS Detection using Short-time Fourier Transform based Technique," *Int. J. Comput. Appl.*, vol. CASCT, no. 1, pp. 7–10, Aug. 2010, doi: 10.5120/998-32.

[178] J. P. V. Madeiro, P. C. Cortez, F. I. Oliveira, and R. S. Siqueira, "A new approach to QRS segmentation based on wavelet bases and adaptive threshold technique," *Med. Eng. Phys.*, vol. 29, no. 1, pp. 26–37, Jan. 2007, doi: 10.1016/j.medengphy.2006.01.008.

[179] N. Prashar, M. Sood, and S. Jain, "Semiautomatic detection of cardiac diseases employing dual tree complex wavelet transform," *Period. Eng. Nat. Sci. PEN*, vol. 6, no. 2, p. 129, Nov. 2018, doi: 10.21533/pen.v6i2.188.

[180] S. K. Mukhopadhyay, M. Mitra, and S. Mitra, "ECG feature extraction using differentiation, Hilbert transform, variable threshold and slope reversal approach," *J. Med. Eng. Technol.*, vol. 36, no. 7, pp. 372–386, Oct. 2012, doi: 10.3109/03091902.2012.713438.

[181] M. Rakshit and S. Das, "An efficient wavelet-based automated R -peaks detection method using Hilbert transform," *Biocybern. Biomed. Eng.*, vol. 37, no. 3, pp. 566–577, 2017, doi: 10.1016/j.bbe.2017.02.002.

[182] H. N. Abderahman, H. R. Dajani, and V. Z. Groza, "Adaptive R-Peak Detector in

Extreme Noise Using EMD Selective Analyzer," in *2022 IEEE International Symposium on Medical Measurements and Applications (MeMeA)*, Messina, Italy: IEEE, June 2022, pp. 1–6. doi: 10.1109/MeMeA54994.2022.9856531.

[183] B. K. Pradhan, B. C. Neelappu, J. Sivaraman, D. Kim, and K. Pal, "A Review on the Applications of Time-Frequency Methods in ECG Analysis," *J. Healthc. Eng.*, vol. 2023, no. 1, p. 3145483, Jan. 2023, doi: 10.1155/2023/3145483.

[184] I. Beraza and I. Romero, "Comparative study of algorithms for ECG segmentation," *Biomed. Signal Process. Control*, vol. 34, pp. 166–173, Apr. 2017, doi: 10.1016/j.bspc.2017.01.013.

[185] S. S. Mehta and N. S. Lingayat, "SVM-based algorithm for recognition of QRS complexes in electrocardiogram," *IRBM*, vol. 29, no. 5, pp. 310–317, Nov. 2008, doi: 10.1016/j.rbmret.2008.03.006.

[186] G. Goovaerts, S. Padhy, B. Vandenberk, C. Varon, R. Willems, and S. Van Huffel, "A Machine-Learning Approach for Detection and Quantification of QRS Fragmentation," *IEEE J. Biomed. Health Inform.*, vol. 23, no. 5, pp. 1980–1989, Sept. 2019, doi: 10.1109/JBHI.2018.2878492.

[187] P. Silva *et al.*, "Towards better heartbeat segmentation with deep learning classification," *Sci. Rep.*, vol. 10, no. 1, p. 20701, Nov. 2020, doi: 10.1038/s41598-020-77745-0.

[188] S. Vijayarangan, V. R., B. Murugesan, P. S.P., J. Joseph, and M. Sivaprakasam, "RPnet: A Deep Learning approach for robust R Peak detection in noisy ECG," in *2020 42nd Annual International Conference of the IEEE Engineering in Medicine & Biology Society (EMBC)*, Montreal, QC, Canada: IEEE, July 2020, pp. 345–348. doi: 10.1109/EMBC44109.2020.9176084.

[189] X. Liu, H. Wang, Z. Li, and L. Qin, "Deep learning in ECG diagnosis: A review," *Knowl.-Based Syst.*, vol. 227, p. 107187, Sept. 2021, doi: 10.1016/j.knosys.2021.107187.

[190] P. Choudhary and J. Ramavtar, "ECG Signal denoising using UWT and features extraction using LabVIEW," presented at the International Research Journal of Engineering and Technology, 2016.

[191] M. L. Ramirez *et al.*, "A Novel Methodology for Calculating Heart Rate using Images Processing," *IEEE Lat. Am. Trans.*, vol. 14, no. 8, pp. 3522–3527, Aug. 2016, doi: 10.1109/TLA.2016.7786329.

[192] N. Otsu, "A Threshold Selection Method from Gray-Level Histograms," *IEEE Trans. Syst. Man Cybern.*, vol. 9, no. 1, pp. 62–66, Jan. 1979, doi: 10.1109/TSMC.1979.4310076.